Chapter 5

(Crystalline) Materials Under High Pressure

5.1. Material properties

A material can be described using its macroscopic and microscopic properties. The phenomena manifested by materials at pressures prevalent at the depths of the Earth are not only first-rank problems of geosciences but stand at the forefront of modern condensed matter physics (Hemley and Ashcroft, 1998). The core states in an atom remain sharp delta-function-like states. These states are raised or lowered relative to their positions in isolated atoms. The shifts are mainly due to the screened Coulomb potential from the rest of the atoms in the crystal. The description of the former properties is obtained from its thermodynamic behaviour. Through the elucidation of Boyles theory (1660), the pressure (P), volume (V) and temperature (T) relationship was established.

For microscopic description, the basic Hamiltonian at the level of elementary nuclear and nuclearcharge is expressed as:

$$\hat{H} = \hat{H}_{\mathrm{nn}} + \hat{H}_{\mathrm{en}} + \hat{H}_{\mathrm{ee}}, \tag{5-1}$$

where $\hat{H}_{\mathrm{nn}}$ and $\hat{H}_{\mathrm{ee}}$ are the kinetic energy of the nuclei and electrons, respectively, and the third term represents the Coulombic attractions. When the system is enclosed in a volume, V, the stationary states of the fundamental Schrödinger equation can be represented by

$$\hat{H}\Psi(V) = E(V)\Psi(V) \tag{5-2}$$

The relation involves volume V, which is alterable by pressure. This quantum-mechanical expression embodies a complex many-body problem. (*Note*: An atomic unit of pressure is $e^2/2a_0^4$, which corresponds to 14,720 GPa.)

The microscopic description of the properties of minerals, like other crystalline solids, is seen to be governed by quantum mechanics, which governs the behaviour of electrons and nuclei in solids. Again, the atoms in a mineral manifest space-group symmetry. Hence, a knowledge of crystallography and solid-state physics becomes important in understanding the mineral behaviour, especially with respect to the phase transitions, equations of state (EOS), electrical and chemical transport, etc. However, in minerals, it should be noted that interactions between electrons in atoms can be seen as responsible for all such behaviour.

Conventional solid-state physics extends from electronic band theory, explaining metals, insulators and semiconductors, to the theory of superconductivity and the quantum

Hall effect. X-ray, neutron and light scattering have become powerful probes of structures from microscopic to near-macroscopic length scales.

Quantum theory shows that the time-independent ground state of a system is given by a complex anti-symmetric many-body wave function (whose square gives the probability density of finding a particle in each point in space):

$$\rho(r) = \int \mathrm{d}r_2\, \mathrm{d}r_3\, \mathrm{d}r_4 \cdots \Psi(r, r_2, r_3, r_4, r_5, \ldots)\, \Psi^*(r, r_2, r_3, r_4, r_5, \ldots) \tag{5-3}$$

In an atom or molecule, the eigenvalues are the well known energy levels of the electronic system, which are modified by other atoms in the crystal.

The core states of atoms are sharp delta function-like states, which are raised/lowered in energy with respect to their positions in isolated atoms. The valence and conduction states broaden into bands. Under pressure, the bands broaden and become different from those of atomic states (*see* Section 5.1.2).

Crystals must have a lower energy than the aggregate of the constituent atoms separated from each other. The binding force between atoms is dominantly electrostatic and the Pauli's exclusion principle keeps the electrons apart. In ionic crystals, the binding force is primarily due to the electrostatic attraction among ions (e.g., Na^+ and Cl^-) while in covalent crystals the binding occurs through hybridization of valence electrons causing a lowering of the energy of electrons (e.g., in diamond).

In metals, the binding force arises from embedding the atom cores in a sea of itinerant electrons. In silicates, the bonds are nearly half ionic and half covalent. In van der Waals bonding, the dipoles fluctuate on separated atoms or molecules and the forces occur through local many-body exchanges and correlation interactions among electrons.

Excited state properties involve the energetic exciting of electrons out of their ground-state configurations. These are depicted in optical spectra.

High pressure alters the nature of chemical bonds, electronic and crystal structures, and thermal and mechanical properties of solids. Simple molecular solids may transform into a polymeric phase before they become metals at high pressure (Maihiot et al., 1992). Large molecules are stiffened by high pressure. That is how a droplet of pressure-frozen oil (large molecule) becomes capable of denting a steel plate!!

Very soft materials manifest an increase in density by as much as 1,000% (i.e., 20 times) at pressures of several hundred GPa, while the incompressible ones may show up to $\sim$50% increase in density. With increasing density, electrons in all materials become increasingly unstable and, above a critical density, the electrons delocalize into conduction states, thus forming a metal. The metallization process occurs due to an electronic overlap of valence and conduction bands.

Pressure may induce order, but it also can bring about disorder. Pressed beyond its stability field, a crystalline matter may transform to an amorphous material. This amorphization persists when the temperature is too low for recrystallization to the equilibrium high-pressure crystalline phase. Such unusual metastable states manifest varying degrees of disorder.

Much information on the bulk properties at high temperatures and pressures and on single-crystal elasticity and strength anisotropy may be obtained by integrating the high-pressure techniques, the scope of which are presented below (Table 5.1).

Pressure-induced phase changes or bonding changes follow several rules:

Rule 1

Open-structure collapse. Open structures stabilized by weak ionic or van der Waals forces can easily collapse under pressure yielding to *denser structures*.

$$\text{E.g., KCl or NaCl (BI) structure} \xrightarrow[P]{2.5\ \text{GPa}} \text{CsCl (B) structure (denser)}$$

(discussed earlier in Section 3.1)

Rule 2

Valence number changes. A few valence bonds per atom are non-metallic, whereas those with higher valence number are metallic. Under pressure, lighter elements behave like heavier elements. Examples: Germanium (Ge) a semiconductor with open diamond structure collapses to a white tin structure and becomes a metallic electrical conductor (like aluminium). Silica (SiO_2) (with SiO_4 tetrahedra) at ~ 10 GPa and moderate T transforms to stishovite (a TiO_2–-rutile structure) with hexavalent silicon.

In general, under pressure, an insulator transforms to a semiconductor or metallic state (*Mott transition*). An exception to this rule is observed when high-valent cations transform to lesser valency under pressure. Ferric iron is seen to reduce reversibly to ferrous iron at $\sim 1-2$ GPa pressure (proved by ^{57}Fe Mössbauer spectroscopy).

Rule 3

Effects on *cooperative phenomena*. An increase or decrease in magnetism and superconductivity are seen under high pressure. For example, iron above 11 GPa (RT) loses its ferromagnetic behaviour.

Rule 4

Reaction-path blocking: Certain reaction paths may be blocked. For example, poorly crystalline graphite yields to ordinary cubic diamond but a hexagonal form of diamond

TABLE 5.1

The scope of different pressure techniques

Techniques	Determination	High-pressure range
XRD (hydrostatic)	Lattice parameters Bulk moduli	Multi-megabar
RDX	Shear modulus Single-crystal elasticity tensor	200 GPa
Ultrasonic	Velocities of V_P and V_S — their orientational dependence	<20 GPa
Shock-wave	Bulk elasticity	H_{PT} Hugoniot
Ab initio calculations	Elasticity	>300 GPa

can only be prepared by subjecting highly crystalline graphite to a pressure of 13 GPa and 1,500°C.

At high pressure, carbon takes the diamond structure (5 GPa), while silicon and germanium take the white tin structure (10 GPa). White tin changes to a body-centred tetragonal form with coordination number 8. Generally, the high-pressure forms of lighter elements or compounds are suggested by low-pressure forms of chemically *heavier* elements or compounds.

5.1.1. Thermodynamics, equilibrium and time interval

Thermodynamics provides a description of the equilibrium states of systems with many degrees of freedom. It focuses on a small number of macroscopic degrees of freedom, such as internal energy, temperature, density or magnetization, needed to characterize a homogenous equilibrium state. In systems with a broken continuous symmetry, thermodynamics can be extended to include slowly varying elastic degrees of freedom and to provide descriptions of spatially non-uniform states produced by boundary conditions or external fields. Since the wavelengths of elastic distortions are long compared with any microscopic length, the departure from ideal homogeneous equilibrium is small.

Thermodynamic equilibrium is produced and maintained by collisions between particles or elementary excitations that occur at a characteristic time interval, τ. In low-temperature solids or in quantum liquids, τ can be quite large, diverging as some inverse power of the temperature T.

The mean distance λ between collisions (mean free path) of particles or excitations is characteristic velocity V times τ. In solids, V is typically a sound velocity. Most disturbances in many-body systems have characteristic frequencies that are of the order τ^{-1}. If excited, they decay rapidly to equilibrium.

5.1.2. Many-body systems and broken symmetry

5.1.2.1. Crystalline symmetries: 5-fold symmetry, icosahedra and quasi-crystals

The system of crystals is classified based on 230 symmetries (*see also* Section 5.1.5). A periodic crystal is invariant with respect to a discrete set of translations only, rather than to the continuum of translations that leave the high-temperature state unchanged.

The concept of symmetry helps approach condensed matter phases, from high-temperature fluids to low-temperature quantum crystals. A description of their symmetry can be made in terms of order parameters, which can also be invoked to explain phase transitions, elasticity, hydrodynamics and topological defect structures.

The concepts of broken symmetry and order parameters have emerged as unifying theoretical concepts applicable not only to condensed matter physics but also to particle physics and even to cosmology. Condensed matter physics has built on atomic and

molecular physics and also on classical and quantum mechanics. It also relies on statistical mechanics and thermodynamics.

Along with these concepts, *many-body theory* can explain normal Fermi liquids, electrons phonon-s, magnetism and superconductivity. Nature offers an unlimited variety of many-body systems, from dilute gases to quantum solids to living cells and quark-gluon plasma. These cover the subject which can be referred to as "hard" condensed matter physics.

Mean field theories are set up. Mean field theory replaces the actual configurations of the local variables (e.g., spins) by their average value and it neglects the effects of fluctuations about the mean.

The densest packing of 12 spheres around a central sphere is icosahedral and this rule may continue hierarchically. Since the early 1960s, many icosahedral clusters have been found. The size of an icosahedron is limited by the increasing strain with increase in size. At a certain size, a transition from icosahedron to cuboctahedron will probably occur.

The hierarchical packing may be obtained by arranging Penrose tilings in two or three dimensions — a mathematical pattern that has the geometrical properties required of a quasi-crystal. In 3D, Penrose tiles are obtuse and in acute rhombohedra form with angles of 116.6 and 63.4° (*see* Mackay, 1998). However, hierarchy can also offer an alternative to lattice repetition in providing an assembly of atoms with an infinite number of almost identical or quasi-equivalent sites. Hierarchy has now appeared as a building principle in a class of inorganic materials, the quasi-crystals. These are solids with *5-fold symmetry* as indicated by their diffraction patterns — a symmetry impossible for a conventional pattern.

Quasi-crystals are a further step away from conventional crystals because they have many centres of local icosahedral symmetry. We now may expect many more varied structures beyond the austere domain of classical crystallography. Clusters of boron suboxide, B_6O, show icosahedral shapes, produced from hierarchial clusters with 5-fold symmetry (usually forbidden to solid crystals). Without dislocated grain boundaries, the glide planes in this boron suboxide are locked and so the particles are very hard, suggesting promising technical applications (*see* Hubert et al., *Nature*, **391**, 376–378, 1998).

5.1.2.2. Broken symmetry

The macroscopic properties are governed by *conservation laws* and *broken symmetries*. Associated with each broken symmetry are distortions, defects and dynamical modes that provide paths to restore the symmetry of the original high-temperature state. Magnetic systems have played a very important role in the development of our understanding of broken symmetry.

These can reveal how the breakdown of symmetry occurs and results in generalized elasticity. The phenomena we commonly observe involve an order of 10^{27} particles (e.g., as in a litre of water) and the motion of each of those particles can scarcely be observed. However, we can observe microscopic variables, such as particle density, momentum density or magnetization, and measure their fluctuations and response to external fields.

It is these observables that characterize and distinguish the many different thermodynamically stable phases of matter that account for why liquids flow, solids are rigid, some are coloured, some are transparent, some are insulators and others are metals or semiconductors, etc. Even the simplest atoms in aggregate can occur in different states. For example, helium can be seen as gas, liquid or solid and also as a non-viscous superfluid at low temperatures.

5.1.2.3. Electron excitations and band gaps

Presence of unpaired electrons builds up the magnetism. Hund's rule maximizes the net magnetic moment but decreases the total electrostatic energy. The formation of energy bands (hybrid crystalline electronic states) may lead to intermediate- or low-spin magnetic structures. In Fe^{3+} ($3d^5 : t_{2g}^3$ and e_g^2 electronic configuration) the net magnetic moment is $5\mu_B$ (μ_B = Bohr magneton) while that of Fe^{2+} ($3d^6 : t_{2g}^4$ and e_g^2) is $4\mu_B$. The high-spin and low-spin state of Fe^{2+} ($3d^6$) was shown in Fig. 4.5.

The origin of crystal-field splitting is not only due to the potential field of a point-charge lattice but also due to bonding hybridization. Furthermore, d-states are not pure atomic-like states but are dispersed across the Brillouin zone (energy varies with k). The splitting is due to d–d interactions between next-nearest neighbours and to p–d and s–d interactions between neighbouring (oxygen) ions. The d–d interactions lead to splitting that varies as $1/r^5$. The splitting can also be effected by hybridization, which also mediates the sign of the magnetic coupling J.

When the magnetic moments are unequally distributed over different sub-lattices, ferrimagnetism results. From incomplete cancellation of aligned spins, a net spontaneous magnetic moment arises. For ferromagnetic and anti-ferromagnetic phases, the magnetic fields are aligned (below the Curie and Nèel temperatures), which gives rise to magnetic splittings.

Excitations in a system can be induced by external (e.g., electronic or magnetic) or internal (e.g., temperature) fields. In the presence of an intense external electric field, the response can be a function of the magnitude of the field and the susceptibility is a function of the field. This gives rise to a non-linear optical response (e.g., multi-photon excitations). Electrons can be excited into extended or itinerant states (i.e., across the band gap) or the excitations may be local (i.e., forming a localized electron–hole pair or exciton). The electronic transitions involving the valence (bonding) band, the conduction (anti-bonding) band and d-electron levels can be investigated by using optical spectra.

The study of the electronic structure of highly correlated transition-metal compounds is important for a better understanding of a material and, in 1985, Zeanen, Sawatzky and Allen (ZSA) proposed a theoretical phase diagram for it.

In addition to the on-site d–d Coulombic interaction (U) employed in the Mott–Hubbard theory, the ligand-valence band-width (W), the ligand-to-metal charge transfer energy (Δ), and the ligand–metal hybridzation interaction are explicity included as parameters in the model Hamiltonian. The high-energy-scale charge can be varied moderately by external temperature and magnetic field but can be considerably affected by pressure.

When an additional electron is added to a d-orbital, an energy (U, Hubbard) increase occurs. For localization of the electron, the parameter that governs the tendency is U/W, where W is the band-width. Mott or charge-transfer insulators (at low pressures) become metallic under pressure because W increases with pressure and U decreases because of increased screening. Thus, at high pressure, band theory is likely to be more reliable. Again, Monte Carlo simulations (Gunnarson et al., 1996) predict metallic behaviour when $U/W < N$, where N is the orbital degeneracy (5 in the d-orbital case). This again shows that, at high pressure, band theory appears to be more appropriate.

5.1.2.4. Dielectric properties

The dielectric properties such as piezoelectricity, pyroelectricity and ferroelectricity are structure dependent.

Piezoelectricity is manifested by electrical polarization caused by applied stress. With the exception of point group 432, any crystal belonging to one of the 20 remaining non-centrosymmetric point groups (that also contain a unique polar axis) is piezoelectric. The motif common to many piezoelectric crystals is the tetrahedrally coordinated atom.

A common example of piezoelectric crystal is tourmaline, which is also *pyroelectric*. In this, the silicon atoms in the tetrahedra are positively charged; consequently, the extension along the polar axis would result in a negative polarity on the (0001) face. The quartz form of SiO_2 is a very important piezoelectric material used for transducers and frequency-controlled devices.To cater for these applications, large quartz crystals are grown by implanting seeds in large pressure vessels.

Pyroelectric materials are characterized by the presence of a spontaneous polarization, P_s, the magnitude of which is temperature dependent.

Ferroelectricity is manifested when the spontaneous polarization is capable of reversal or re-orientation of its polar direction on application of an electric field. Ferroelectric transition is either a displacive type or an order–disorder type. To understand ferroelectric phase transitions, numerous experimental and theoretical studies are undertaken. The origin of ferroelectric phase transitions in oxides is due to the anharmonic potential surfaces caused by softening of the short-range repulsions by covalent hybridization. These cause the atoms to move off-centre and towards each other.

Oxide ferroelectrics are studied for their (i) soft modes, using time-resolved spectroscopy, (ii) atomic positions, by nuclear and X-ray studies, (iii) ground-state potential surfaces, by electronic structure studies, (iv) electronic structure and (v) macroscopic polarization.

5.1.2.5. Electronic and magnetic behaviour

The electronic and magnetic properties directly influence large-scale global phenomena ranging from the initial differentiation of the planet, the formation and transmission of the Earth's magnetic field, the propagation of seismic waves and the upwelling and downwelling of mass through the mantle (Hemley et al., 1998).

The pressure range within the Earth can compress the rock-forming silicates and oxides by factors of 2–3 and the molecular species and rare gases by well over an order

of magnitude. Discrete magnetic and electronic transformations such as metallization and magnetic collapse may also occur (e.g., Cohen et al., 1997).

Under pressure, volatiles can be bound as "valence lattices" in dense, high-pressure phases, e.g., hydrogen in ice, mantle silicates and ferrous alloys. Pressure at depths may dissociate Fe^{2+}–Mg^{2+} combination from oxide or silicate phases and incompatible elements such as Fe and K may form alloys (Parker and Badding, 1996).

The valence and conduction states broaden into energy bands under higher pressure. When an ion possesses a shell filled with electrons, it attains greater stability. The interaction between ions through Madelung or strong electrostatic forces enhances the crystal stability.

Band structures. In an insulator, the bands are filled and, due to the Pauli exclusion principle, nothing can happen without exciting electrons to states above the gap. But this excitation requires a large energy and, hence, in a small field no current can flow. Metals have partially occupied states at the Fermi level and the current will flow.

In insulators, the highest occupied levels form the valence band, designated as E_v, and the empty energy levels form the bottom of the conduction band, E_c. The difference is the band gap, $E_g = E_c - E_v$. Crystals with band gaps between occupied and unoccupied states should be insulators and those with partially filled bands should be metals.

From the intermediate states (formed by chemical doping), the electrons can be excited into the conduction bands or holes in the valence bands and the crystal becomes a semiconductor. In a non-magnetic system, each band holds two electrons. Thus, a crystal with an odd number of electrons in the unit cell should be a metal since it will have at least one partially filled band. Magnetic crystals that are insulators by virtue of local magnetic moments are known as Mott insulators (Mott, 1990).

At energies intermediate between the valence and conduction bands, there can occur localized states, which affect the optical and transport properties There is a possible relationship between optical modes (high-frequency) and elastic properties (low-frequency) acoustic modes.

5.1.2.6. Ionicity in bonding: Madelung forces

In crystals, atoms donate or accept electrons, resulting in ionicity. The ionicity is driven by the increased stability attained through filling of the outer shell by electrons. For example, oxygen having a nuclear charge (z) should have $1s^2$, $2s^2$ and $2p^4$ electrons but a filled p-shell has six electrons. O^{2-} ion is unstable in the free state but is stabilized by the crystal field in an oxide. In an oxide or silicate crystal, the O grabs two more electrons to form an O^{2-} anion from another atom, usually a positively charged cation. This strong electrostatic (called Medelung) interaction between the ions increases the crystal stability.

The ionic solids are dominated by electrostatic or Madelung forces between charged ions. The alkali halides and alkaline earth oxides are proto-typical ionic solids. Employing all modifications and the self-consistent methods, the EOS, elasticity, the electronic and optical properties of these materials are obtained. In ionic crystals, the Madelung energy is to be added to the overlap energies.

In atomic computation, most studies use a "Watson sphere" (Watson, 1958), which is a charged sphere, usually of opposite charge to the ion.

5.1.3. Covalent bonding and hardness

Hard substances have a high number of strongly directed, covalent chemical bonds per unit volume. Soft substances generally have fewer bonds per unit volume or bonds that are weak or weakly directed, such as ionic or dipole attraction forces. Covalent (electron pair) bond strengths vary between $\sim 60-90$ kcal/mol for most elements present in hard materials. The heavier elements generally offer more bonds per atom. A plot of hardness measured by Knoop indenter vs. the bond energy per molar volume for various substances is essentially linear.

The hardest materials are generally made of light elements, with diamond at the top. Hard materials are brittle because the strongly directed bonds favour hardness but not plasticity, which involves the inter-site motion of atoms. At high pressures, many brittle materials become ductile.

5.1.3.1. Hardness and bulk moduli

Hardness (H) of ionic and covalent materials increases with bulk modulus (Cohen, 1993). Diamond has the highest known bulk modulus, $K = 444$ GPa, and it is also the hardest material known, with its single-crystal $H = 90$ GPa. It is followed by cubic boron nitride (cBN) with corresponding values of $K = 369$ GPa and single-crystal $H = 48$ GPa (Sung and Sung, 1996).

High-bulk moduli require high charges and small volumes; thus, tetravalent cation dioxides could be hard. Although silicon is the smallest tetravalent cation, the common forms of silicon dioxide are not hard because of their open structures, such as in quartz and cristobalite phases $(N_C = 4)$. But the denser phase stishovite has a much higher bulk modulus, 298 GPa (Hemley et al., 1994). This value is much higher even than that of the other common hard material, alumina, whose bulk modulus is 252 GPa. Indeed, among polycrystalline materials, the hardness of stishovite (33 GPa) rivals those of the hardest materials. The bulk moduli (K) and the Knoop micro-hardness values of synthesized compounds obtained by different workers were earlier presented in Table 3.5.

5.1.3.2. Phonon-s and band states

Most solids can be described by harmonic or by anharmonic approximations. In the former, non-interacting phonon-s couple strongly and form a broad continuum band. In the latter, strong interaction of phonon-s leads to the formation of states of bound quasi-particles, coupled only weakly in the crystal. For example, in two-phonon- vibrational spectroscopy, the quasi-particle is a biphonon- acting as a molecular oscillator. The biphonon- forms a sharp peak separated from the origin of the broad two-phonon-continuum band by the amount of its anharmonicity. The condition when the harmonic and anharmonic cases overlap has been a problem of great interest in condensed systems. It is postulated that if the relative magnitudes of the continuum bandwidth and the anharmonicity could be varied so that the former would exceed the latter, the band biphonon- would disappear into the continuum band.

In a crystal, the band states are characterized by a continuous quantum number κ, so that the eigenvalues are $\varepsilon(\kappa)$ and the eigenfunctions are represented by Bloch states (*see* equations (4-27a)–(4-27c)):

$$\phi(\kappa, r) = U(r)\exp^{-i\kappa r} \tag{5-4}$$

where $U(r)$ is a periodic function of position r. The eigenvalues (i.e., energy) as a function of κ are known as the band structure. By studying the band structure, densities of state (DOS) and the charge densities, one can understand the nature of bonding and its changes with chemistry, distortions and pressure.

Experimentally, bands can be studied by photoemission spectroscopy, which helps determine the relative energies of emitted electrons as functions of input photon energy and wavevector, or by employing X-ray spectroscopy.

In angle-resolved photoemission, the observed band structure is the energy spectrum for removing electrons from the surface of the crystal, which is sometimes a complex phenomenon — and may be broadened or shifted from the intrinsic energy levels in the interior of the crystal.

In a non-magnetic system, each band holds two electrons and thus a crystal with an odd number of electrons in the unit cell should be a metal because it will have at least one partially filled band (except in Mott insulators). Magnetic crystals that are insulators by virtue of local magnetic moments are known as Mott insulators (Mott, 1990). The real energy states in a crystal are not single-particle eigenstates at each value of κ; rather, there is an energy spectrum which has more or less strong peaks at the quasi-particle energies.

5.1.4. Elasticity

According to Hooke's law (Nye, 1985), the stress (σ) and strain (ε) for small deformation in a crystal are linearly related by

$$\sigma_{ij} = C_{ijkl}\varepsilon_{kl}, \qquad i,j,k,l = 1,2,3$$

where the fourth rank tensor C_{ijkl} is the elastic constant tensor.

Thus, the elastic constants can be determined directly from the computation of the stress generated by small strains (Wentzcovitch et al., 1995). The cubic crystal has three independent elastic constants, C_{11}, C_{12} and C_{44} (in the Voigt notation).

The strained lattice (lattice vectors $\mathbf{a}'$) used in determining the elastic constants is related to the unstrained lattice ($\mathbf{a}$) by the relation $\mathbf{a}' = (I + \varepsilon)\mathbf{a}$, where I is the identity matrix. The strain tensor is

$$\varepsilon = \begin{pmatrix} \varepsilon & \varepsilon/2 & 0 \\ \varepsilon/2 & 0 & 0 \\ 0 & 0 & 0 \end{pmatrix} \tag{5-5}$$

so that Hooke's law gives

$$\sigma_{xx} = C_{11}\varepsilon, \qquad \sigma_{yy} = \sigma_{zz} = C_{12}\varepsilon, \qquad \sigma_{yz} = C_{44}\varepsilon, \qquad \sigma_{zx} = \sigma_{xy} = 0.$$

For the lower symmetry of the strained lattice, the $4 \times 4 \times 4k$-point mesh yields 20 special k-points. The ion positions are still fixed by the symmetry so in the strained lattice only electrons should be relaxed.

The elastic constants completely specify the elastic properties and acoustic velocities of a single crystal. For the purpose of comparing with seismological data, it is interesting to compute the elastic properties of an isotropic polycrystalline aggregate. The bulk modulus of such an aggregate is well defined, whereas the shear modulus is inherently uncertain, depending on the arrangement and shape of the constituent crystals (Watt et al., 1976). The bulk modulus is related to the elastic constants by

$$K = 1/3(C_{11} + 2C_{12}) \tag{5-6}$$

The isotropic shear modulus in the Hashin–Shtrikman averaging scheme (Hashim and Shtrikman, 1962) is given by

$$G = 1/2(G_{\mathrm{U}} + G_{\mathrm{L}}) \tag{5-7}$$

where the upper (U) and lower (L) bounds are, respectively,

$$G_{\mathrm{U}} = C_{44} + 2\left[\frac{5}{C_s - C_{44}} + \frac{18(K + 2C_{44})}{5C_{44}(3K + 4C_{44})}\right] \tag{5-8}$$

and

$$G_{\mathrm{L}} = C_s + 3\left[\frac{5}{C_{44} - C_s} + \frac{12(K + 2C_s)}{5C_s(3K + 4C_s)}\right] \tag{5-9}$$

where $C_s = (C_{11} - C_{12})/2$.

5.1.4.1. Elastic anisotropy

Anisotropy of crustal and mantle materials arises from the preferred alignment (texturing) of the aggregate of intrinsically anisotropic minerals. For cubic crystals, the elasic anisotropy is conveniently expressed in terms of Zener ratio (A), which is the ratio of the shear moduli in the (100) and (110) planes in the [100] direction:

$$A = \frac{2C_{44}}{C_{11} - C_{12}} = \frac{2(S_{11} - S_{12})}{S_{44}} \tag{5-10}$$

For the elastically anisotropic case, $A = 1$.

Under Reuss approximation, A can be directly measured from radial diffraction experiments, without the use of any assumed bulk property (Singh et al., 1998; Merkel et al., 2002) but, with increasing pressure, A value decreases (Karki et al., 1999).

For cubic materials, single-crystal elastic anisotropy and seismic anisotropy can be related through the anistropy factor, A, defined as

$$A = \frac{2C_{44} - C_{12}}{C_{11}} - 1. \tag{5-11}$$

For isotropic material, $A = 0$.

The anisotropy of a single crystal is determined by its elastic constant tensor. For cubic phases, there are three independent elastic constants and, for hexagonal phases, there are five. The elastic constants are related to the elastic wave (seismic) velocities by the *Cristoffel equation* (Nye, 1985)

$$|c_{ijkl}\mathbf{n}_j\mathbf{n}_l - \rho V^2\delta_{ik}| = 0$$

where V is the velocity, ρ is the density, $\mathbf{n}$ is the propagation direction and C_{ijkl} is the elastic constant tensor and δ_{ik} is the Kraenecker delta function. The elastic anisotropy is determined by calculating the velocity of each of the elastic waves (one P and two S) for all propagating directions. The data on elastic anisotropy have important implications for the interpretation of seismological observations of the anisotropy in terms of flow in the upper mantle (Tanimoto and Anderson, 1984). To determine the elastic anisotropy of a polycrystalline aggregate, one must know the elastic constant tensor of the individual crystals and the texture as specified by the orientational distribution function.

The eigen values of the 3×3 matrix yield the three unique elastic-wave velocities for propagation direction n, whereas the eigenvectors yield the polarization directions (Musgrave, 1970).

5.1.5. Elastic constants: crystal systems

The elastic constants are directly related to the inter-atomic potentials. Consequently, the parameters of a potential are often determined from elastic constants.

In general, the number of independent elastic constants increases as the point-group symmetry of the solid decreases: the most isotropic solids have the smallest number of elastic constants. The highest symmetry that a three-dimensional (3D) crystalline solid has is cubic symmetry and three independent elastic constants. The solid hexagonal symmetry has only two independent elastic constants. In two- and 3D crystals of lower symmetry, there are more elastic constants. For example, a 2D crystal with 4-fold symmetry (rather than 6-fold symmetry, like a 3D crystal with cubic symmetry) has three elastic constants. The numbers of independent elastic constants for 3D crystals are listed in Table 5.2.

For crystals of simple systems (e.g., cubic and hexagonal), the values for room-temperature harmonic elastic constants and densities (ρ) are shown in Table 5.3.

TABLE 5.2

Number of elastic constants for crystal systems

Crystal system	No. of elastic constants
Triclinic	21
Monoclinic	13
Orthorhombic	9
Tetragonal	6 or 7
Rhombohedral	6 or 7
Hexagonal	5
Cubic	3

TABLE 5.3

The elastic constants of some phases crystallizing in cubic and hexagonal systems

Name Ref (composition)	ρ	C_{11}	C_{12}	C_{44}	Reference
Cubic crystals					
Fluorite (CaF_2)	3.180	1.64	0.53	0.337	
Chromite ($FeCr_2O_4$)	4.450	3.225	1.437	1.167	Hearmon (1956)
Diamond (C)	3.511	9.320	4.112	4.167	
Galena (PbS)	7.5640	1.020	0.380	0.250	Hearmon (1956)
	7.5640	1.270	0.298	0.248	
Gold (Au)	19.300	1.925	1.630	0.424	Neighbours et al. (1958)
Periclase (MgO)	3.583	2.963	0.951	1.559	Anderson et al. (1966)
Periclase (at 298 K)	5.390	2.230	1.200	0.790	
Pyrite (FeS_2)	5.016	3.818	0.310	1.094	Simmons et al. (1963)
Halite (NaCl)	2.162	0.487	0.131	0.127	Lewis et al. (1967)

Name (composition)	ρ	C_{11}	C_{12}	C_{13}	C_{33}	C_{55}	Reference
Hexagonal crystals							
Apatite	3.218	1.667	0.131	0.665	1.396	0.663	Hearmon (1956)
Beryl	2.68	2.800	0.990	0.670	2.480	0.658	Hearmon (1956)
Biotite	3.05	1.860	0.324	0.116	0.540	0.058	Alexandrov et al. (1961)
Cancrinite	2.460	0.520	0.086	0.124	0.826	0.238	Alexandrov et al. (1961)
Muscovite	2.790	1.780	0.424	0.145	0.549	0.122	Alexandrov et al. (1961)
Phlogopite	2.820	1.780	0.3020	0.152	0.510	0.065	Alexandrov et al. (1961)
β-quartz (873 K)	2.533	1.166	0.167	0.328	0.104	0.361	Hearmon (1956)
Sphalerite (ZnS)	4.089	1.312	0.663	0.509	1.408	0.286	Klerk (1967)

The temperature derivatives of elastic constants are determined by using the value at room temperature and the harmonic value of the elastic constants. Commonly, elastic constants decrease with temperature but, for MgO, NaCl and other halides, C_{12} values are seen to increase with temperature.

The experimental values of second-order elastic constants, G and K (in 1012 dyes/cm^2), of different minerals (polycrystals) at room temperature (298 K) were obtained by Cheng (1974).

Name composition	G	K
(α-Cr_2O_3)	1.298	2.321
Almandine	0.951	1.765
Almandine	0.943	1.770
Sp.Almandine	0.966	1.756
Sp.Almandine	0.961	1.777
Spess-alm-pyrope	0.049	1.750
Hematite (α-Fe_2O_3)	1.213	2.088
Fayalite (α-Fe_2SiO_4)	0.536	1.220
Fayalite (β-Fe_2SiO_4)	0.815	2.050
Spinel ($MgAl_2O_4$)	1.080	1.972
Fe–spinel ($FeAl_2O_4$)	0.853	2.103
Magnetite (Fe_3O_4)	0.773	1.769
Magnetite (Fe_2TiO_4)	0.263	1.210
Ferrosilite ($FeSiO_3$)	0.608	1.018
Forsterite (Mg_2SiO_4)	0.797	1.281
Enstatite ($MgSiO_3$)	0.788	1.066
Ortho-pyroxene ($Mg_{0.5}Fe_{0.5}$)SiO_3	0.686	1.041
($MnFe_2O_4$)	0.692	1.851
($NiFe_2O_4$)	0.713	1.823
α-quartz (SiO_2)	0.447	0.378
SiO_2–rutile (SiO_2)	1.696	2.93
Rutile (TiO_2)	1.124	2.155

In a cubic crystal, there are only three unique elastic constants, C_{11}, C_{12} and C_{44}. The shear velocity in the 100 direction is calculated from $(C_{44}/\rho)^{1/2}$ and the compressional velocity in the 100 direction from $(C_{11}/\rho)^{1/2}$, where ρ is the density. The shear velocity in the 110 direction is calculated from $\{(C_{11} - C_{12})/2\rho\}^{1/2}$ and the compressional velocity in the 110 direction from $\{(C_{11} + C_{12} + 2C_{44}/2\rho\}^{1/2}$.

Values of A (equation (5-11)) greater than 1 signify that C_{44} is greater than $1/2(C_{11}-C_{12})$, whereas the opposite holds when A is less than 1. For gold, the elastic anisotropy is large; $A = 2.9$ at ambient pressure. An extrapolation of ultrasonic data suggests that this should increase weakly with pressure (Duffy et al., 1999).

At the transition, the $C_{11-} - C_{12}$ instability gives rise to an anomalous decrease in the shear-wave velocity, which provides a seismic signature that could be diagnostic of the presence of a separate phase (e.g., free silica in the deep mantle and D$''$ zone).

The estimates of elastic constants of minerals are generally taken from zero-pressure experiments. However, the anisotropy can be strongly pressure dependent (e.g., in MgO; Karki et al., 1997).

5.1.5.1. Cauchy relation and its violations

The Cauchy relation, defined as $C_{12} - C_{44} = 2P$, is valid when all inter-atomic forces are central under static lattice conditions.

While studying MgO, Karki et al. (1997) observed that, as pressure increases, the calculated value of $C_{12} - C_{44} - 2P$ decreases (Cauchy violation). The decrease is relatively slow up to 100 GPa and then rapid between 100 and 150 GPa, as shown in Fig. 5.1. The relatively faster decrease above 100 GPa is due to the slow increase of C_{12} between 100 and 150 GPa. The initial pressure dependence of the deviation from the Cauchy condition agrees fairly well with low-pressure ultrasonic behaviour.

Since MgO remains a wide-gap insulator to pressures well beyond the deep-mantle pressure (when covalent bonding or metallic bonding is less significant), the Cauchy violations cannot be explained. The PIB model, with a zero-pressure value of −72 GPa for $C_{12} - C_{44} - 2P$, has also shown a very similar pressure dependence of the Cauchy violation (Isaak et al., 1990).

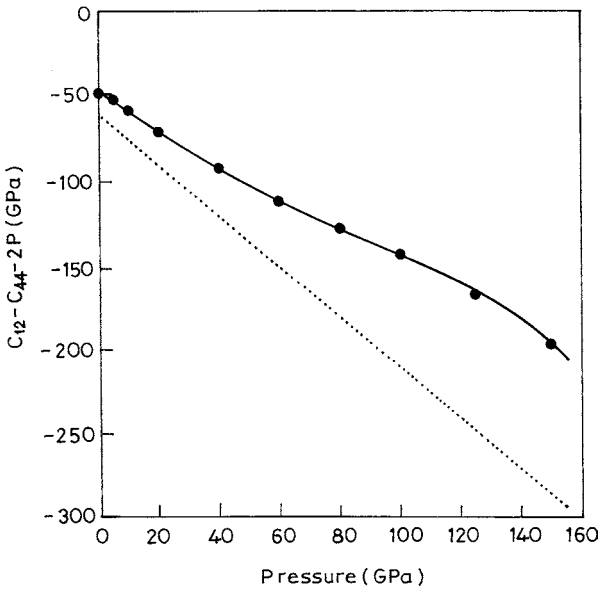

Figure 5.1. Pressure variation of the Cauchy violation in MgO. The circles represent the calculated values. The first-order extrapolation from ultrasonic data (Jackson and Niesler, 1982) is shown by the dashed line (Karki et al., 1997; © 1997 Mineralogical Society of America).

5.1.6. Born's stability criteria: B_1, B_2 and B_3

The mechanical stability of crystal lattices can be estimated from their elastic moduli by the so-called Born's stability condition based on the elastic lattice energy (Binggelli et al., 1994). For the stability of a trigonal lattice, the following three conditions need to be satisfied:

$$B_1 = C_{11} - |C_{12}| > 0,$$

$$B_2 = (C_{11} + C_{12})C_{33} - 2C_{13}^2 > 0$$

$$B_3 = (C_{11} + C_{12})C_{44} - C_{14}^2 > 0. \tag{5-12}$$

For the elastic stability of a phase, the determinant as well as sequential principal minor of the matrix of elastic stiffness coefficient (c_{ij}) must be greater than zero

The first condition, $B_1 > 0$, ensures stability with respect to the elastic waves in the basal plane perpendicular to the c-axis; $B_2 > 0$ implies positive compressibility and $B_3 > 0$ is associated with shear acoustic modes in the $y-z$-plane (Terhune et al., 1985). When one of these moduli vanishes, the initial crystalline structure becomes homogeneously unstable against the corresponding fluctuations.

Under a given P, T condition, the lattice is elastically stable when all the three conditions of elastic moduli are satisfied.

The values of the three parameters (B_1, B_2 and B_3) can be estimated from the calculated elastic moduli under compression.

For trigonal quartz-type phases at ambient pressure, six calculated values (in GPa) obtained by different workers are

C_{11}	C_{33}	C_{44}	C_{12}	C_{13}	C_{14}	Reference
55.1	123.0	26.2	18.1	22.2	−4.2	Tsuchiya et al. (2000)
64	118	37	22	32	2	Grimsditch et al. (1998)

Both B_1 and B_2 parameters increase regularly with pressure and are positive in all pressure ranges up to the transition. However, B_3, which indicates the shear stability of the lattice, decreases and becomes zero at ~7 GPa as a result of decrease in C_{44} with pressure (Fig. 5.2; Tsuchiya et al., 2000). The stability condition vanishes near the transition pressure. This indicates that lattice instability from the shear softening of the quartz-type lattice is induced by pressure (e.g., α-quartz study by Binggeli et al., 1994).

Tse and Klug (1991) reported a sudden decrease in the modulus B_2 as a function of time at the critical pressure. For a trigonal structure, B_2 can be related to the stability of volume compressibility which is given by

$$(C_{11} + C_{12} - 4C_{44} + 2C_{33})/B_2. \tag{5-13}$$

A discontinuous volume reduction is seen to occur at the first-order transformation because the decrease in B_2 to zero corresponds to the divergence in compressibility.

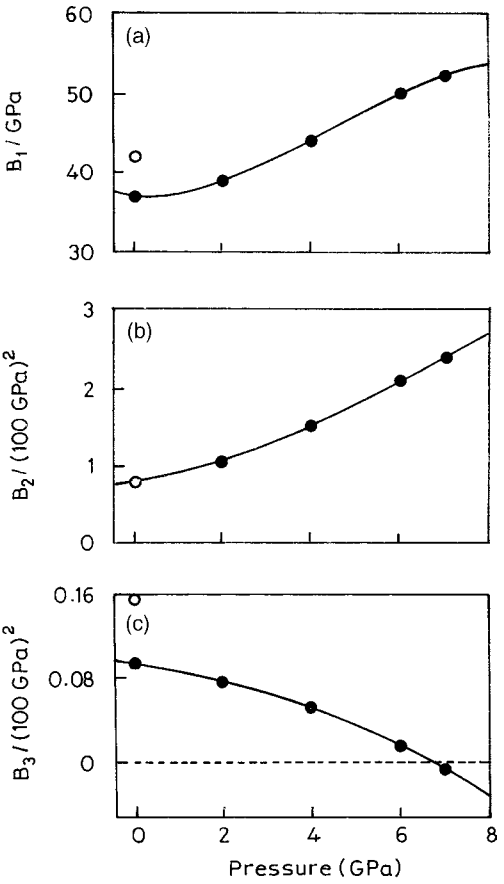

Figure 5.2. Calculated Born's parameters of quartz-type lattice with pressure. The B_1, B_2 and B_3 values are shown in (a), (b), and (c) by solid circles, respectively. Earth value estimated from experimental measurements is also plotted by an open circle. The lattice is elastically stable if these parameters are positive. The B_3 value decreases with pressure at 2 GPa and changes to negative near to amorphization pressure at 7 GPa. The result is related to the negative correlation of C_{44} with pressure (Tsuchiya et al., 2000, © Springer-Verlag).

Hence, the violation of the condition $B_2 > 0$ can be considered as caused by the transformation.

For quartz, B_2 softens at 22.3 GPa. For ice, B_1 and B_2 soften at the pressure of $\sim$0.9 GPa when becomes amorphous. This observation may suggest the question: Is an amorphous phase a consequence of mechanical melting? MD calculation showed that, at $\sim$22.3 GPa, α-quartz would show an abrupt softening of B_2. This softening is due to transition to a disordered phase. Employing first-principles pseudopotentials, it is seen that, at $\sim$30 GPa, B_3 softens but B_1 and B_2 stiffen with pressure (Bingelli and Chclikowsky, 1992).

The result of Born's stability criteria indicated that the volume collapse of the quatz-type lattice with pressure-induced transformation originates from pressure-induced shear elastic instability. The effect of the shear stress field decreases transition pressure and enhances lattice instability as well as the uniaxial stress field. The quartz-type structure transforms to the rutile-type structure on decompression when σ_{xy} is imposed (Tsuchiya et al., 2000).

5.1.7. Thermoelasticity

From the experimental $P-V-T$ data, the thermoelastic parameters can be derived using a high-temperature Murnaghan EOS. Based on the thermodynamic identity

$$K_{\mathrm{T}}(P,T) = -V\left(\frac{\delta P}{\delta V}\right)_{\mathrm{T}} \tag{5-14}$$

and with $K_{\mathrm{T}}(P,T)$ expressed as (isothermal $T = 300$ K):

$$K_{\mathrm{T}}(P,T) = K_{\mathrm{T}_0} + K'_{\mathrm{T}_0}P + \left(\frac{\delta K_{\mathrm{T}}}{\delta T}\right)_0 (T-300) + \left(\frac{\delta^2 K_{\mathrm{T}}}{\delta P\,\delta T}\right)P(T-300) \tag{5-15}$$

The $P-V-T$ relation can also be defined by equation

$$V(P,T) = V(O,T)\left(1+\frac{b}{a}P\right)^{-1/b}, \tag{5-16}$$

where

$$a = K_{\mathrm{T}_0} + \left(\frac{\delta K_{\mathrm{T}}}{\delta T}\right)_0 (T-300)$$

and

$$b = K'_{\mathrm{T}_0} + \left(\frac{\delta^2 K_{\mathrm{T}}}{\delta P\,\delta T}\right)_0 (T-300)$$

At high temperatures and pressures, a nearly uniform behaviour of a number of thermoelastic parameters of oxides and silicates has been noted in experimental and theoretical investigations. Above the Debye temperature, the product αK_{T} has been observed to be independent of temperature and pressure.

Important thermoelastic parameters such as the temperature derivative of bulk modulus, $\delta K/\delta T$, the pressure derivative of thermal expansion, $\delta\alpha/\delta P$, and Anderson–Grüneisen parameter, δ_{T}, need to be derived experimentally at simultaneous high pressures and temperatures. These thermoelastic parameters can be derived from measurements of volume change of the crystallographic unit cell at simultaneous high pressures and temperatures. Recent breakthroughs in high $P-T$ single crystal X-ray diffraction using a diamond-anvil cell (Zhao et al., 1995) provide most accurate

measurements of unit-cell dimensions at uniform temperature and sustained hydrostatic pressure.

5.2. Atomic vibrations in crystals: phonon-s

In crystals, atomic vibrations propagate as weakly interacting waves with wave vector $\mathbf{k}$ and frequencies $\omega_j(\mathbf{k})$. To each wave, one can assign an oscillator with frequency $\omega_j(\mathbf{k})$.

Phonon-s. Each wave can behave as a *particle* (de Broglie) with energy equal to $\hbar\omega_j(\mathbf{k})$ and momentum $\mathbf{p}$ equal to $\hbar\mathbf{k}$. This quasi-particle, called a *phonon-, is* an elementary component of sound energy with frequency ω, just as a photon is related to light (electromagnetic) energy. (Thus, wave → quantum oscillator → phonon-s.)

Phonon- gas. A solid may be conceived as a box containing phonon- gas and, like molecules in ordinary gas, phonon-s collide with one another. The energy of phonon- gas is the sum of the energies of individual phonon-s but the collision of phonon-s does not conserve momentum. However, a crystal lattice does not always participate in the collisions of phonon-s.

As the temperature falls, the number of high-momentum phonon-s becomes smaller and smaller. At $T \ll \Theta$ (Debye temperature), almost all phonon-s are close to the centre of the first Brillouin zone.

By combining the dependence of heat capacity and mean free path on temperature, one obtains

$$\Xi \sim T^3 \exp(\Theta/T).$$

Near absolute zero, the mean free path is enormously large. Even at extremely low temperature, the number of phonon-s in a crystal is enormous, e.g., at $(1/10)\Theta$ (tenth Debye) temperature. About 10^{20} phonon-s are present per cubic centimetre.

The phonon- gas is the main heat reservoir of a solid but the number of phonon-s in a solid is not constant. High temperatures create more phonon-s and the number of phonon-s is proportional to (the third power of) temperature. However, most of the phonon-s have energies close to $k_B T$.

There are acoustic and optical phonon-s. The velocity of phonon-s corresponds to the speed of sound. A study of resonance absorption of light in a crystal would reveal the properties of optical phonon-s.

Neutron scattering and phonon- study. Low-momentum phonon-s are ordinary sound waves. Hence, by studying sound propagation in crystals, the properties of individual phonon-s can be studied. The inelastic scattering of neutrons in crystals provides very important information on phonon-s. In its motion through a crystal, a neutron makes the atoms "swing" and creates sound waves and its own energy is lowered. The change in the neutron's energy is equal to the phonon-'s energy. This is what follows from the dispersion law of phonon-s. Employing high-energy neutron sources, the obtained phonon-'s energy spectra reveal the construction of solids.

5.2.1. Elastic waves in crystals

The longitudinal (V_P) and shear (V_S) wave velocities of isotropic aggregates are given by (*see* Section 2.6.2):

$$V_P = \sqrt{\frac{K + 4/3G}{\rho}}, \qquad V_S = \sqrt{\frac{G}{\rho}} \tag{5-17}$$

where ρ is the density and K and G are isotropic bulk and shear moduli, which are determined from the single-crystal elastic constants (C_{ij}) using the *Hashin–Strikman averaging scheme* shown by equation (5-7). The bulk sound velocity is given by (*see* Section 2.6.2)

$$V_B = \sqrt{\frac{K}{\rho}} = \sqrt{V_P^2 - \frac{4}{3}V_S^2} \tag{5-18}$$

Temperature is expected to lower the density and seismic wave velocities, while addition of Fe will increase the density and decrease the seismic-wave velocities.

The seismic-wave velocities of periclase in the lowermost part of the lower mantle are lower than those of Mg-silicate perovskite by 3–5%. Additional Fe has a strong effect. Magnesio-wustite with $X_{Fe} = 0.20$, a value appropriate for a pyrolite bulk composition, has a shear velocity that is 15% lower than that of $MgSiO_3$ perovskite.

It should be possible to detect a number of minor or secondary phases in the lower-mantle magnesiowüstite, $CaSiO_3$ perovskite and SiO_2 silica — all have distinctive wave velocities and should be seismically distinguishable.

5.2.1.1. Shock waves

Shock waves are intense compressional waves of short duration (typically $\sim 10^{-6}$ s) created by the high velocity of projectiles or by intense light pulses. Shock pressures can be high, exceeding 600 GPa. Shock pressure may accompany high temperatures ~2,000–15,000 K.

Shock-pressure measurements may involve $P–V–T$ EOS. The data are based on Rankie–Hugoniot equations that follow from conservation of momentum, mass and energy in response to the impact. The observable quantities are U_S and U_P, V_S is the shock-propagation speed and V_P the particle speed. The shock speed V_S is measured by timing the shock propagation over a known distance. The particle velocity V_P is inferred from collision properties of the impact or from the observation of free-surface velocity as the shock wave emerges from the shocked material.

Shock measurements can be made for electrical resistance, laser X-ray diffraction and spontaneous and coherent Raman scattering. Each shot in a shock experiment generates one point in the EOS.

Shock waves in crystals. To study true shock waves at the atomistic level, non-equilibrium molecular dynamics (NEMD) simulations with Newton's equations of

motion are solved on the computer for thousands of strongly interacting atoms (Straub et al., 1980). True shock waves exhibit steady profiles (density, velocity, stress and energy) which accompany dissipative, irreversible flow of atoms in the direction transverse to the planar-wave propagation. The NEMD profiles could also be explained by a continuum constitutive model, which uses Navier–Stokes equations of hydrodynamics.

Planar shock waves in a single crystal become steady waves through transverse displacements of atoms, not by viscous flow as in fluid shock waves (Hoover, 1979) but rather by plastic flow through the concerted slippage of atoms over each other.

In the Lennard–Jones (LJ) pair-potential solid, represented by fcc lattice, a shock wave travelling in the (100) direction would result in slippage along one of the four available [111] planes through emission at the shock front of a Shockely partial dislocation. The wave leaves behind a stacking fault (the usual ABCABC… stacking of a triangular-lattice, when the close-packed planes become ABABCA). For steady planar shock waves, depending on their strength, the Hugoniot relation offers a general statement of mass, momentum and energy conservation linking a given initial equilibrium state.

To obtain the sound velocities from acoustic-mode formation, the following relation can be used:

$$V = V_0 \left(\frac{w}{w_0} \right) \left(\frac{a}{a_0} \right) \tag{5-19}$$

where the subscript zero represents values at one atmosphere.

Velocities vs. pressure can be used to calculate the pressure dependence of the elastic moduli from the relation

$$K_S = \rho(V_P^2 - 4/3V_S^2), \qquad G = \rho V_S^2 \tag{5-20}$$

where K_S is the adiabatic bulk modulus, G the shear modulus and ρ the density.

5.2.1.2. Shock velocity and particle velocity

In shock-wave measurements, the paired variables are particle velocity (U_p) and shock velocity (U_s), from which, and with HugonistEOS, the pressure–density relations are calculated.

A new pair of variables has been chosen to improve the accuracy of primary calibration of anvil devices. They are the density (ρ) measured with XRD and the acoustic velocity (V_ϕ) measured with the ultrasonic method or Brillouin scattering on the same sample under the same compression (Mar and Hemley, 1998).

Pressure is derived from

$$P = \int V_\phi^2 \, \mathrm{d}\rho$$

The resultant $P-\rho$ relation is a primary pressure standard.

The metastable pressure–volume Hugoniot data may be converted to the corresponding shock-velocity–particle-velocity ($V_S - V_P$) data using the relation (Liu, 1975):

$$V_S = V_0[P^m/M(V_0^m - V^m)]^{1/2} \tag{5-21}$$

$$V_P = [P^m(V_0^m - V^m)/M]^{1/2} \tag{5-22}$$

where P^m and V^m are the metastable Hugoniot pressure and volume, respectively, V_0^m the initial volume of the high-pressure phase and M the molecular weight. It has been shown by Ruoff (1967) that the data in the $V_S - V_P$ plane can be represented by

$$V_S = C_0 + sV_P + s'V_P^2 \tag{5-23}$$

and, if an EOS is assumed to have the following form:

$$K^S = K_0^S + K_0^{S'}P + 1/2K_0^{S''}P^2 \tag{5-24}$$

then

$$K_0^S = \rho_0 C_0^2$$

and

$$K_0^{S'} = 4s - 1$$

where K_0^S is the isentropic bulk modulus at zero pressure, $K_0^{S'}$ is its first pressure derivative evaluated at zero pressure and ρ_0 is the initial density.

The method of converting the experimental Hugoniot to a new Hugoniot, centred at a different initial condition, was demostrated by McQueen et al. (1963). In doing so, they obtained

$$P^m = \frac{P^e\left[1 - \frac{\gamma}{2}\left(\frac{V^m}{V^e} - 1\right)\right] - \frac{\gamma}{V^\varepsilon}(E_0^e - E_0^m)}{1 - \frac{\gamma}{2}\left(\frac{V_0^m}{V^e} - 1\right)} \tag{5-25}$$

where P, V, E and γ are the pressure, volume, specific internal energy and the Grüneisen parameter, superscripts "e" and "m" denote the experimental and metastable Hugoniots and subscript zero represents the initial condition. Some quantities have to be evaluated before calculations from the foregoing equation can be performed. Firstly, determine the change of the specific internal energy between the starting material and the high-pressure phase at zero pressure:

$$\Delta E_{tr} = E_0^e - E_0^m = P[(V^m - V^e) + (V_0^m - V_0^e)]/2 \tag{5-26}$$

assuming that the temperature effect is negligible.

5.2.1.3. Shock-induced transitions

Shock-induced phase transitions are observed by noting: (i) the breaks or discontinuities in the shock velocity (V_S)−particle velocity (V_P) curves, (ii) the abrupt changes in sound velocity, (iii) the multi-wave structure in wave profiles of pressure or particle velocity and by analyzing the shock-recovered samples.

The shock-treated sample data are compared with those obtained from in situ experiments to know if the observed discontinuity in the Hugoniot $P-V$ curve indicates any new phase not observed by an in situ experiment. On the $P-V-T$ surface, the shock Hugoniot function chalks out a path different from an isotherm in static experiments. Lattice disorder is observed in diverse minerals induced by stresses ≤ 30 GPa (Horz and Quaide, 1973). Pronounced lattice disorders for quartz and plagioclase felspar are observed when shocked to < 22 GPa (Cygan et al., 1992). Conversion of graphite to diamond occurs in rocks shocked to < 30 GPa, at a pressure distinctly short of melting (e.g., Koebertl et al., 1995).

Most oxides and silicates (excepting MgO and Al_2O_3) undergo shock-induced phase transitions in pressures up to 200 GPa (Ahrens, 1980).

Shock-induced phase transition can be of reconstructive or non-reconstructive type, depending on whether the transition involves atomic diffusion or not. The latter type may be completed within a micro-second time scale of a shock experiment. Martensite or electronic transition belongs to this type. The martensitic nature of B1−B2 transition in NaCl shocked parallel to [111] occurs at pressure lower by 4 GPa than that shocked parallel to [100] (Fritz et al., 1971).

In shock compression of Fe_3O_4 and α-Fe_3O_3, the transition is due to a change in configuration from a high-spin state to a low-spin state. Mössbauer spectroscopic (and XRD) study in DAC showed a transition to a non-magmetic state at ~ 50 GPa (Mao et al., 1977). The volume change accompanying phase transition is predicted to be 13% based on the density-cation radius systematics of the corundum structure. Both the crystal-field splitting (Δ) and the spin-pairing energy (π) depend on the volume (Goto et al., 1982). Under pressure, the following relations with the inter-atomic distance (r) are assumed:

$$\Delta \propto r^{-3.0}$$

$$\pi \propto r^{1.3}$$

Shock-compression experiments have been performed on a single crystal of forsterite (Mg_2SiO_4) up to 170 GPa (by Syono et al., 1981). Extraordinary high values of HEL (up to 12 GPa) were found to be direction dependent. The onset of phase transition was at ~50 GPa, which is much higher than those known high-pressure transformations in static experiments, such as < 20 GPa for olivine to modified spinel or to spinel transition (Akimoto et al., 1976) and below 30 GPa for post-spinel dissociation to ilmenite or perovskite type $MgSiO_3$ plus MgO (Ito et al., 1982). The mixed phase region persists up to ~100 GPa, where the shocked state merged into the high-pressure regime (Syno, 1984).

Reconstructive-type phase transformations under shock compression preferentially occur along the shear zone where temperature is high enough to promote the transition, resulting in very heterogeneous textures in the shock-recovered materials.

A heterogeneous yielding model has been developed for brittle, low thermal conductivity materials, in which dynamic yielding occurs along the stress-concentrated sheared zone (Syono, 1984).

5.3. Inelastic and non-hydrostatic states

From the 1920s, pioneers such as P.W. Bridgman, D. Griggs, H. Heard, M. Paterson, W. Brace et al. worked on minerals and rocks under high-pressure–high-temperature conditions. These involved inelastic processes such as brittle fracture, frictional sliding, plastic deformation and dynamic metamorphism. The results have been applied to handle diverse problems related to the rheology of Earth's materials, such as the flexure of the lithosphere, metamorphic textures, post-glacial rebound, deformation under partial melting, forces driving plates, the physical nature of earthquake sources, seismic anisotropy and so on. It is, however, now more clearly known that non-hydrostatic stresses generated in high-pressure phase transitions are responsible for deep-focus earthquakes (Kirby et al., 1991).

5.3.1. Stress states

A solid sample placed between a pair of flat faces of perfectly rigid anvils will experience stress states which can be expressed along a set of three orthogonal axes (x_1, x_2 and x_3). The x_1 and x_2 axes are in a plane parallel to the anvil face, and x_3 is along the load axis. The centre of the anvil face is taken as the origin of the coordinates. For circular anvil face, the stress state is cylindrically symmetric about the x_3 axis. Thus, the stress component σ_{11} equals σ_{22}. For a finite shear strength of the sample, $\sigma_{33} \geq \sigma_{11}$. Since the anvil faces are flat and parallel, the stress gradient in the direction of applied load (x_3 axis) is absent.

The maximum shear stress for von Mises criterion of yielding leads to the relation

$$\sigma_{33} - \sigma_{11} = t = 2\tau_y = \sigma_y$$

where t, τ_y and σ_y are, respectively, the uniaxial stress component, shear strength and yield strength of the specimen. And the pressure $\sigma_\rho = (\sigma_{11} + \sigma_{22} + \sigma_{33})/3 = (\sigma_{11} + t/3)$ ($\because\ \sigma_{11} = \sigma_{22}$). The value of t can be determined from the diffraction data.

The stress at the origin of the coordinates is given by a tensor:

$$\sigma_{ij} = \begin{pmatrix} \sigma_{11} & 0 & 0 \\ 0 & \sigma_{11} & 0 \\ 0 & 0 & \sigma_{33} \end{pmatrix} = \begin{pmatrix} \sigma_\rho & 0 & 0 \\ 0 & \sigma_\rho & 0 \\ 0 & 0 & \sigma_\rho \end{pmatrix} + \begin{pmatrix} -t/3 & 0 & 0 \\ 0 & -t/3 & 0 \\ 0 & 0 & 2t/3 \end{pmatrix}$$

$$= \sigma_\rho + D_{ij} \tag{5-27}$$

The second term in equation (5-27) is the deviatoric stress component. The strain produced by σ_{ij} is a superposition of stress components. As the load on the anvil is

increased, σ_ρ increases and can reach a few hundred gigapascals. The magnitude of t is normally a few % of σ_ρ. The strain produced by D_{ij} is small and is adequately described by linear elasticity theory. The adequacy of the linear elasticity theory is linked to the precision of the lattice strain measurement, which is at best one part in 10,000 (Singh et al., 1998).

5.3.1.1. Non-hydrostatic stress

Under conditions of uniaxial non-hydrostatic stress, a phase transformation (or distortion) could be observed to occur at a lower pressure than it would under hydrostatic conditions. Experimentally, this has been shown by Zou et al. (1981).

The pressure-induced phase transition is reflected by changes in diffraction patterns. It is possible to detect small distortions in the unit cell caused by the deviators from the hydrostatic condition of the stress acting on the sample.

The measurement of unit-cell dimensions as a function of pressure gives the pressure–volume relation (i.e., EOS) of a solid sample.

Ostapenko (1971) has shown that, for two polymorphs in hydrostatic equilibrium, the denser modification will become more stable if a uniaxial stress of significant magnitude is applied. A similar result has been shown to be true for second-order transitions where the more rigid form (higher bulk and shear moduli) becomes the stable phase if a sufficiently large uniaxial stress is applied (Ostapenko, 1973).

Under conditions of non-hydrostatic stress, the concept of thermodynamic equilibrium is not valid. The local phase equilibria differ depending on the orientation of the phase interfaces to the stress and, therefore, transformations occurring under non-hydrostatic stress cannot strictly be located on an equilibrium-phase diagram.

Differential stress: examples. The rheological constraint at depth involves measurement of small differential stresses at high $P-T$. Stress measurements at depth along the San Andreas fault system suggest that plate-scale motion may result from shear stresses as small as 10–20 MPa (Hickman et al., 1988).

Microstructures of mantle xenoliths suggest that, with depth, as temperature and mean stress increase, the differential stresses decrease from ~15 to ~5 MPa. (*Note*: At 70 km, mean stress is 2.2 GPa.) This is attained by large-scale isostatic adjustments (Hager, 1990) and by the shape of the Earth's geoid (Jeffreys, 1963). Moreover, the flow strengths of crystalline solids weaken exponentially with temperature. (*Note*: At high pressure, quartz may get weakened hydrolytically.)

Deviatoric stress. Deviatoric stress is the total stress with 1/3 the trace (sum of the diagonal terms) subtracted from each of the diagonal terms. When the stress is deviatoric, the sum of the principal stresses is zero. This reflects the shape-altering stresses and is the driving force field for flow. A purely deviatoric stress can be represented in a coordinated system where all the diagonal terms are zero and the off-diagonal terms are non-zero.

Deviatoric stress can be measured in multi-anvil apparatus from the broadening of XRD lines. Uniaxial compression in DAC can ideally be used for quantitative study of deviatoric stress at ultra-high pressures (Singh et al., 1998).

The uniaxial component or deviatoric stress is a measure of $t = (\sigma_1 - \sigma_3)$. The yield and shear strengths of a material, designated as σ_y and τ, are related to the maximum t, which the material can support as $\sigma_y = 2\tau = t$. This equility (*Von Mises condition*) is satisfied only when the material is observed to deform under pressure. In high-pressure experiments, the assumption commonly used is that $t = \sigma_y$.

Shear stress (τ) is determined from the measurement of pressure gradients on the sample (in a DAC) by

$$\tau = (h/2)\mathrm{d}P(r)/\mathrm{d}r$$

where h is the sample thickness. This analysis depends critically on the shape of the diamond in the pressure cell and is only valid when the diamonds remain flat (no cupping) and the sample continues to flow under loading (Spitzig and Leslie, 1971).

The stress difference between materials (assuming that the stress is equivalent to the pressure) is obtained from the EOS of each material. This approach significantly overestimates the deviatoric stress because it neglects the effect of the shear modulus on the measured differential strains (Meng and Weidner, 1993).

Gold standard. The effect of deviatoric stress (i.e., departures from hydrostaticity) on the unit-cell volume measurement and further on the volume-based pressure calibration is directly proportional to K/G of the measured material (Meng et al., 1993). As gold has an unusually high value of K/G (6.2) compared with most samples (1–2), the measurement of the unit-cell volume of gold is very sensitive to the existence of even a small amount of deviatoric stress. At RT, the deviatoric stress in gold increases with increasing pressure above 15 GPa. By 30 GPa, the calculated deviatoric stress is above 0.6 GPa. The deviatoric stress decreases dramatically with increasing temperature and disappears by a temperature of about 650 K. The pressure dependence of the uniaxial stress t for gold is obtained as

$$t = 0.06 + 0.015P,$$

where P is the pressure in GPa in (Duffy et al., 1999).

The method for determining the deviatoric stress in a diamond-anvil cell, the deviatoric stress in gold as a function of pressure and temperature and also the deviatoric stress effect on the volume-based pressure calibration have been discussed by Meng et al. (1993). The elastic moduli of gold as a function of pressure is shown in Fig. 5.3b.

5.3.2. Crystallographic shear

Anion-deficient non-stoichiometry is accommodated in certain transition-metal oxides by eliminating point defects by the so-called *crystallographic shear*, cs, which provides a means of accommodating anion-deficient non-stoichiometry without introducing point defects and without change of cation coordination. Crystallographic shear phases can be regarded as translation modulations of the parent structure, the translation boundaries being cs planes.

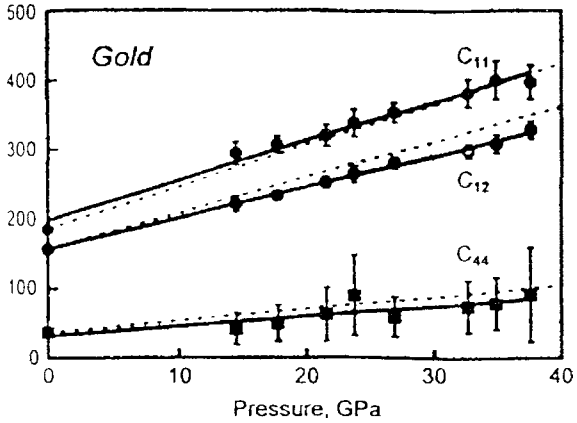

Figure 5.3. The elastic moduli of gold as a function of pressure. (a) second order elastic moduli of gold as a function of pressure. The doted lines show finite strain extrapolations of ultrasonic data (Hiki and Granato, 1966) while the simple lines are obtained from study up to 37 GPa. The vertical axis stands for Cij (GPa). The symbols show individual data points and solid lines are finite strain fits (Birch, 1978) to the present data combined with ambient pressure data (Hiki and Granato,1966). Uncertainties are one standard deviation.

In the ordering of shear planes, elastic strain appears to play a crucial role. Extensive relaxation around the shear planes seems essential for stabilizing some structures. Isolated cs planes offer solid–solid interfaces.

5.3.2.1. Shear and deformational twinning

The extensional axis (ε_1) is parallel to $[\bar{1}01]$ in the (101) plane of the tetragonal phase of cristobalite. This plane consists of distorted six-membered tetrahedral rings, and, in the high-temperature cubic phase, becomes a pseudo-close-packed (111) plane. This direction is equivalent to $[\bar{1}\bar{1}2]$, the slip direction for the smallest possible "shear" of the $\{111\}$ layers. The cristobalite I $\rightarrow$ cristobalite II phase transition can, therefore, be viewed as a shear of the crystal structure. This involves the sliding of adjacent close-packed sheets against each other, much like the martensitic-type transformation in close-packed metals.

Palmer and Downs (1991), in their single-crystal diffraction work on the high-pressure phase of cristobalite, observed splits in single-crystal diffraction peaks (measured in ω and $\omega/2\theta$ scans), indicative of deformation twinning. These deformation twins are distinct from the tetragonal to monoclinic transformation twins. However, a co-existence of both high- and low-pressure phases within the hysteresis region has been observed in single-crystal X-ray experiments (Downs and Palmer, 1994) and in Raman spectroscopic studies (Palmer et al., 1991).

5.3.3. Strain anisotropy in crystalline mass: e.g., hcp iron

Radial XRD (RXD) measurements (vide Section "Radial X-ray diffraction (RXD): deviatoric stress" of Chapter 4) provide single-crystal elasticity information (Singh et al., 1998a,b). In a laboratory experiment, the stress (non-hydrostatic) state of a sample is determined by compressing the sample between the two anvils and by employing the RXD technique.

The results from RXD (zero-frequency) and multi-anvil (ultrasonic frequency) measurements show good correspondence, bracketing a wide frequency range including seismic waves. The K/G ratios obtained for hcp iron by the two methods under different pressure experiments are (Mao et al., 1998):

Method	Pressure (GPa)	K/G
RXD	20–39	2.7 ± 0.7
Ultrasonic	16.5	2.68 ± 0.1

In the RXD measurements on hcp iron (Mao et al., 1998) the strong (hkl) dependence of lattice strain reflects a strong elasticity anisotropy or an (hkl) dependence of stress (Singh and Balasingh, 1994).

A strong *hkl* dependence of t, defined as $t = \sigma_3 - \sigma_1 = 1.5(\sigma_3 - \sigma_\rho)$ (σ_3 = axial stress; σ_1 = radial stress) in the polycrystalline specimen may partially or fully account for the observed lattice-strain anisotropy. Again, the development of the basal plane slip texture common in hcp metals could conceivably lower the t of grains with their c-axis at 45° orientation.

The integrated study by Mao et al. (1998) reveals that the Earth's inner core may represent the low shear modulus of hcp iron close to melting or the existence of additional components with low shear-wave velocities but with similar densities.

The seismic V_S of the inner core is lower. If this softening of V_S represents possible Born–Durand pre-melting effects (Tallon, 1979) or partial melting, the observed shear values would constrain the inner-core temperature to near-melting. The attenuation of seismic waves may be affected by near-melting softening or by the presence of additional low-velocity phases in the inner core.

Theories predict a small V_P anisotropy (4% faster in the c than in the a direction) of the inner core. This requires a perfect alignment of hcp iron crystals or the presence of a giant single crystal (Stixrude and Cohen, 1995). A partial alignment of hcp iron crystals may be sufficient for accounting the magnitude of the inner-core anisotropy (Mao et al., 1998).

5.4. Spontaneous strain

In phase transition, the spontaneous strain, ε, is defined in terms of the lattice parameters. For example, for a cubic to tetragonal phase transformation, if the cubic phase has lattice parameter a_0 while the tetragonal phase has parameters a and c, the spontaneous strain ε is measured as

$$\varepsilon = (a - a_0)/a_0$$

which is proportional to Q^2

If in the transition there is no change in the translational symmetry and the unit cell merely changes its shape, no extra reflection would appear in the diffraction pattern. In such a case, if no extra points appear in the reciprocal lattice, the transition does not involve a change in the boundaries of the Brillouin zone. This type of transition is called a zone-centre transition, where $\varepsilon \propto Q$ holds.

In cases where the translational symmetry changes with changes in the reciprocal lattice and the boundaries of the Brillouin zone, they are called *zone-boundary transitions.* Here, the relation $\varepsilon \propto Q^2$ commonly holds. When, in the transition (e.g., cubic $\Rightarrow$ tetragonal), a reduction in translational symmetry and the formation of a superlattice occur, the relation $\varepsilon \propto Q^2$ holds.

The symmetry of the low-temperature form must be a subgroup of the high-temperature symmetry. In other words, the low-temperature form is derived from the high-temperature form by a loss of some symmetry elements, i.e., the structures are topologically similar.

Excess free energy, expressed as G rather than ΔG, is defined as the excess over that which the high form would have if the phase did not occur. Usually, the excess quantities are stated as G, S, etc., rather than ΔG, ΔS, etc.

5.4.1. Spontaneous strain and order parameter

For a displacive phase transition involving a supergroup to subgroup relation, the order parameter, Q, may couple to the lattice strain. The resulting excess lattice distortion is characteristic of the phase transition and is usually expressed as the spontaneous strain, ε (Carpenter, 1992).

The spontaneous strains for a tetragonal $\rightarrow$ orthorhombic transition are given by

$$\varepsilon_1 = (a - a_o)/a_o$$
$$\varepsilon_2 = (b - a_o)/a_o$$

and

$$\varepsilon_3 = (c - c_o)/c_o$$

where a, b and c are lattice parameters of the orthorhombic phase, while a_o and c_o are linear parameters of the tetragonal phase extrapolated into the stability field of the orthorhombic phase for $P4_2/mnm \rightarrow Pnnm$ (Carpenter et al., 2000) transition, which is pseudo-ferroelastic in nature (Wadhawan, 1982).

The symmetry-breaking strain is

$$(\varepsilon_1 - \varepsilon_2) = \frac{a - b}{a_o},$$

which is proportional to the order parameter Q.

The volume strain is given by

$$V_s = (V - V_o)/V_o,$$

where V is the unit-cell volume of the orthorhombic phase and V_o is the volume of the tetragonal phase. For small strains, V_s, ε_1, ε_2 and ε_3 are related approximately as $V_s = \varepsilon_1 + \varepsilon_2 + \varepsilon_3$.

Of great current interest is the transformation in dense SiO_2 (stishovite) from the rutile to a $CaCl_2$-type structure ($P4_2/mnm \rightarrow Pnnm$), which is thought to be a classic displacive transition (Karki et al., 1997d). Single-crystal XRD measurements near

50 GPa pressure in quasi-hydrostatic media have proven the $P4_2/mnm \rightarrow Pnnm$ transition, which is largely displacive but exhibits hysteresis indicating weak first-order character. A Landau model has been developed that quantitatively relates all of the spectroscopic, elastic, structural and thermodynamic data for the Si–O system. The elastic instability at the transition gives rise to anomalies in the Raman spectrum, which are expected to be a general feature of such pressure-induced transition (Hemley et al., 2000).

Since Q can never be measured directly, measurements of macroscopic properties, such as the spontaneous strain, are essential for the thermodynamic description of the phase transitions. This is illustrated below with a case of tetragonal to monoclinic transition seen under pressure (Cristobalite I → II; Palmer and Finger, 1994).

For the phase transition 422 → 2, the active representation is of type E (Salje, 1990), comprising an orthogonal pair of basis functions (*see* Table 5.4). The $xz(\varepsilon_3)$ basis function describes a shear parallel to a, such that the angle β departs from 90°. The tetragonal condition $a = b$ is relaxed in the monoclinic system and so an addition of improper strain is allowed, involving extensions or contractions parallel to these two axes (i.e., non-zero ε_{11} and ε_{22}). The strain is subject to the constraint that there shall be no net volume change and, therefore, the condition to be satisfied is $\varepsilon_{11} = -\varepsilon_{22}$ (Palmer and Finger, 1994).

The alternative basis function $yz = -xz(\varepsilon_5 = -\varepsilon_4)$ is a shear parallel to [110], i.e., the $(1\bar{1}0)$ plane of the tetragonal cell, leaving a unique (diad) axis perpendicular to the $(1\bar{1}0)$ shear plane. There is no longer any constraint for $\gamma = 90°$ and so an additional improper strain, ε_{12}, is allowed. The resulting unit cell has $\alpha = \beta = \gamma \neq 90°$ (because of ε_{23} and ε_{13}). This is better described by a conventional monoclinic unit cell, with b perpendicular to the $(1\bar{1}0)$ shear plane of the tetragonal phase and with a and c lying within this plane. It can be clearly seen that the deformation can be described by the xz-basis function but not by the yz–xz basis function.

Palmer and Finger (1994) described the spontaneous strain that violates the symmetry of the super group 422. In addition to this symmetry-breaking strain (ε^{sb}), extra and non-symmetry-breaking strains (ε^{nsb}) are allowed, which couple to the A representation of 422. These strains do not affect the off-diagonal (shear) terms of the

TABLE 5.4

Spontaneous strain relations for the subgroup 422 (after Salje, 1990)

Active Repn.	Sub-group	Spontaneous strain		No. of elastic domains	Basis functions
		Proper	Improper		
A_2	4			1	Z
B_1	222	$\varepsilon_1 = -\varepsilon_2$		2	$(x^2 - y^2)$
B_2	222	ε_6		2	xy
E	2	ε_5	$\varepsilon_1 = -\varepsilon_2$	4	
E	2	$\varepsilon_5 = -\varepsilon_4$	ε_6	4	x, y, xz, yz
E	1	$\varepsilon_4, \varepsilon_5$	$\varepsilon_6, \varepsilon_1 = -\varepsilon_2$	8	

Note: The monoclinic subgroups correspond to an orientation with the unique axis parallel to [010].

strain tensor but may modify the on-diagonal terms and, hence, the unit-cell volume. One can expect symmetry-breaking strains parallel to a and b, but not c. Therefore, the axial strains may be expressed as

$$\varepsilon_{11} = \varepsilon_{11}^{\mathrm{nsb}} + \varepsilon_{11}^{sb}$$

$$\varepsilon_{22} = \varepsilon_{22}^{\mathrm{nsb}} + \varepsilon_{22}^{sb} \tag{5-28}$$

$$\varepsilon_{33} = \varepsilon_{33}^{\mathrm{nsb}}$$

The non-symmetry-breaking strains must conform to the high-symmetry point group 422 and, therefore, the condition becomes

$$\varepsilon_{11}^{\mathrm{nsb}} = \varepsilon_{22}^{\mathrm{nsb}} \neq \varepsilon_{33}^{\mathrm{nsb}}.$$

The relation between two symmetry-breaking strain components (i.e., for no volume change) is

$$\varepsilon_{11}^{\mathrm{sb}} = -\varepsilon_{11}^{\mathrm{sb}}.$$

From these relations one arrives at the following:

$$\varepsilon_{11}^{\mathrm{nsb}} = \frac{1}{2}(\varepsilon_{11} + \varepsilon_{22}) \tag{5-29}$$

$$\varepsilon_{11}^{\mathrm{sb}} = \frac{1}{2}(\varepsilon_{11} - \varepsilon_{22}).$$

The phase relation involves a shear plus a volume change. The measured strain tensor, S, can, therefore, be separated into a symmetry-breaking tensor:

$$S = \begin{pmatrix} \varepsilon_{11} & 0 & \varepsilon_{13} \\ \varepsilon_{11} & \varepsilon_{22} & 0 \\ \varepsilon_{11} & \varepsilon_{22} & \varepsilon_{33} \end{pmatrix} = \begin{pmatrix} \varepsilon_{11}^{\mathrm{nsb}} & 0 & 0 \\ \varepsilon_{11}^{\mathrm{nsb}} & \varepsilon_{11}^{\mathrm{nsb}} & 0 \\ \varepsilon_{11}^{\mathrm{nsb}} & \varepsilon_{11}^{\mathrm{nsb}} & \varepsilon_{33} \end{pmatrix} + \begin{pmatrix} \varepsilon_{11}^{\mathrm{sb}} & 0 & \varepsilon_{13} \\ \varepsilon_{11}^{\mathrm{sb}} & -\varepsilon_{11}^{\mathrm{sb}} & 0 \\ \varepsilon_{11}^{\mathrm{sb}} & -\varepsilon_{11}^{\mathrm{sb}} & 0 \end{pmatrix} \tag{5-30}$$

The symmetry-breaking strain tensor may be diagonalized to reveal the orientation (i.e., the shear plane) and magnitude of the corresponding strain ellipsoid.

5.5. Strain tensor

Under a hydrostatic pressure, the change in the unit-cell parameters makes up the strain and this phenomenon is represented by a second-rank tensor (Nye, 1957). From each increment of pressure, the strain can be calculated (with certain uncertainties).

The three principal coefficients of the strain, ε_1, ε_2 and ε_3 (conventionally, $|\varepsilon_1| > |\varepsilon_2| > |\varepsilon_3|$) obtained by diagonalization of the strain tensor represent the fractional change in length along the principal axes of the strain tensor. The isothermal linear

coefficient of volume compressibility, β, is given by

$$\beta = V_o - V_p/V_o = -(\varepsilon_1 + \varepsilon_2 + \varepsilon_3) \quad (5\text{-}31)$$

since for compression the principal strains are all negative.

For second-rank tensors, the visualized strain surface is an ellipsoid with principal axes of length $(1 + \varepsilon_1)$, $(1 + \varepsilon_2)$ and $(1 + \varepsilon_3)$.

In monoclinic felspars, the three principal strains are unequal and one of the principal axes is along the diad *b*-axes. Hence, the other two principal axes must lie in the (010) plane. It is seen that in alkali felspars about 60–70% of the volume compression is brought about by a linear compression along the (100) plane normal. However, the same degree of anisotropy is observed in plagioclases.

5.6. Bulk modulus of ionic compounds

Under ambient conditions, the bulk modulus of ionic compounds is given by a general relationship:

$$K \propto Z_a Z_c / V$$

where Z_a and Z_c, are the formal anion and cation charges, respectively, and V is the specific volume per ion pair (Anderson and Nafe, 1965).

Under pressure, packing efficiency increases at phase transition, when the cation coordination number (N_c) increases. As the structure becomes more compact, compression becomes increasingly difficult and the bulk modulus rises. High-pressure phases may thus be hard materials. The archetypal example is the transformation of graphite to diamond or of quartz to stishovite.

5.6.1. Molar volume

The inverse relationship between bulk modulus and molar volume V was first formulated by Bridgman (1923). This relationship was used for predicting bulk moduli of mantle minerals where the data were not available (e.g., Hazen and Finger, 1979). The basic expression is $KV =$ constant. However, anomalous compression behaviours known through recent studies in $(Mg,Fe)_2SiO_4$ spinels and $Ca(Mg,Fe)Si_2O_6$ clinopyroxenes do not conform to the above relationship (Hazen 1993; Zhang et al., 1997). They found that Mg-rich members with smaller molar volume were more compressible at high pressures than their Fe-rich counterparts of larger molar volume.

To explain this discrepancy, a comprehensive study comprising the determination of the crystal structure type, valence state of cations, electronic configuration, polyhedral coordination number as well as the cation substitution becomes a necessity.

5.6.2. Shear modulus: mantle perovskite

Compared with the determination of bulk modulus and the EOS at high pressure, the shear modulus, G, is more difficult to determine. In geophysics, shear modulus is

an important quantity as it is related to the longitudinal (P) and shear (S) velocities as (*see also* equation (5-20)):

$$V_p = [(K_s + 4/3G)/\rho]^{1/2}, \qquad V_s = (G/\rho)^{1/2} \tag{5-32}$$

Using a PIB model (Cohen, 1987), a value of 190 GPa for the G of $MgSiO_3$ perovskite was determined under ambient conditions. Brillouin scattering measurements (Yeganeh-Haeri et al., 1989) showed this value as 184.2($\pm$4.0) GPa (both Voigt–Reuss–Hill bounds).

The single-crystal elastic moduli (in GPa) for $MgSiO_3$ perovskite at zero pressure using the theoretical PIB model and the experimental Brillouin scattering spectroscopy indicate that the value of G under room T, P equals that of the lower mantle at 1,000-km depth (Dziewonski and Anderson, 1981). If the lower mantle is perovskite-rich, the pressure and temperature effects offset each other at that depth (40 GPa and 1,900–2,300 K). At 1,071-km depth, pressure G equals 255 GPa (at 300 K). These indicate that $dG/dT \approx 0.04$ GPa/K is consistent with geophysical data when a perovskite-rich lower mantle is assumed. The measured values of $\delta G/\delta T$ for 15 silicates fall in the range of -0.08 to -0.014 GPa/K (Sumino and Anderson, 1989).

5.7. Magnetic features

5.7.1. Ferromagnetism

In ferromagnets, interactions between the dipoles favour a state in which the dipoles align along the same direction and long-range magnetic ordering occurs at T_c. The spontaneous magnetization is zero above T_c, where thermal motion overwhelms any magnetic alignment.

In other words, ferromagnetism arises from a spontaneous alignment of the atomic magnetic dipoles (spins), driven by magnetic interactions between the atoms. But magnets of certain crystal structure show an inability to attain magnetic order, solely by virtue of the geometrical arrangement of the magnetic atoms. These are geometrically frustrated. The high-temperature supercounductivity is believed by some to be due to a kind of frustrated magnetic state (Anderson, 1986).

Ferromagnetism is generally considered to be geometrically unfrustrated. For discussion on ferromagnetism phase transition, *see* Section "Ferromagnetic phase transition" of this chapter.

5.7.1.1. Curie temperature

The pressure dependence of T_c is a strong function of the doping level and is reminescent of the effects observed in high-temperature superconductors (Neumeier and Zimmermann, 1994), where the total charge-carrier concentration n increases with pressure. Under pressure, the value of $n(P)$ could be non-zero and enhance the ferromagnetic double-exchange coupling.

TABLE 5.5
dT_C/dP and dT_N/dP some ferromagnetic materials

Compound	dT_C/dP (K/GPa)	Source
Sr Ru O_3 perovskite	≈ -5.7	Neumeier et al. (1994)
Ni	$+32$	White and Geballe (1979)
Fe	$=0$	White and Geballe (1979)
Co	$=0$	White and Geballe (1979)
S_{C3}ln	$+1.7$	Grew et al. (1989)
YFe_5O_{12}	$+12.5$	Kafalas et al. (1971)
	dT_N/dP (K/GPa)	
Ca_{1-x} Sr_xMnO_3	$\sim+4$	Neumeier et al. (1994)

The dT_c/dP values of some ferromagnetic materials are shown in Table 5.5. Large values of dT_c/dP suggest that strong magneto-volume effects will be observed in these materials. The largest dT_N/dP and dT_c/dP values occur for the highest electrical resistivity.

The ferromagnetic double-exchange interaction is presumably more strongly pressure dependent than direct or super-exchange (assumed to be responsible for the anti-ferromagnetism) in similar compounds.

5.7.2. Ferrimagnetism

In a ferrimagnet (e.g., magnetite), there are two non-compensating sub-lattices of local dipoles called M_A and M_B, with $M_A \neq M_B$. The interactions between M_A and M_B favour their anti-parallel orientation. Again, a long-range ordering occurs at T_c, with the dipoles M_A aligned in one direction and the dipoles M_B oriented in the opposite direction.

At any temperature below T_c, the spontaneous magnetization is the algebraic sum of the contributions arising from each of the two sub-lattices. In most cases, at any particular temperature, the contribution of one of the sub-lattices is larger in value so that the resulting spontaneous magnetization increases steadily as T is lowered.

In a few cases, the two contributions cancel out at a temperature called the compensation temperature, T_{comp}. Between T_c and T_{comp}, the contribution of one of the sub-lattices dominates. Below T_{comp}, the contribution of the other sub-lattices dominates. The spontaneous magnetization is first positive, then zero and finally negative as the sample cools down. This behaviour, predicted by Louis Neel in 1948, is observed in metal oxides and also in some molecule-based magnets containing organic molecules (Mathonière et al., 1996).

5.7.3. Spin states of iron

In accordance with Hund's rule, the ground-state electronic configuration is the one with maximum spin multiplicity, i.e., $S = 2$. The state with maximum S is stabilized through exchange energy. This state with maximum spin will have the most parallel electrons and, hence, the greatest exchange stabilization energy.

In the case of Fe^{2+}-bearing compounds, such as FeO, FeS_2 and FeS, the electronic configuration is [Ar] $3d^6$ and the levels consist of two sets of orbitals t_{2g} and e_g, which are split according to the octahedral ligand field 10 Dq (or Δ_0).

In the HS state, the electrons occupy the orbitals according to Hund's rule and electrons in $3d^6$ are spread over as $t^3_{2g\uparrow}e^2_{g\uparrow}t^1_{2g\uparrow}$. In the LS state, the electronic configuration becomes $t^3_{2g\uparrow}t^3_{2g\downarrow}$ and the total 3d magnetic moment is zero (in XES, the K'_β satellite emission line vanishes).

In the case of an Fe^{3+}-bearing compound, such as Fe_2O_3, the electronic configuration is [Ar] $3d^5$ and the configuration of the 3d orbitals is $t^3_{2g\uparrow}e^2_{g\uparrow}$ in the HS and $t^3_{2g\uparrow}\ t^2_{2g\downarrow}$ in the LS state to a first approximation.

The exact electronic configuration and magnitude of the magnetic moment would depend on the nature of the ligand field, crystal structure and 3d band structure. However, a finite moment is expected in the case of lower-spin Fe_2O_3 (in XES emission spectrum, a weak $K_\beta{}'$ satellite shows up).

Because the high-spin phase should be the high-entropy phase, the increasing temperature should promote the high-spin magnetic phase rather than the low-spin non-magnetic phase. Increasing temperature leads to disordering of the local moments.

5.7.3.1. Electronic/magnetic ordering: examples

Pressure-induced electronic and magnetic order–disorder effects are known in condensed matter research (Kelso and Banerjee, 1995). To site a few examples: Verwey transition in Fe_3O_4, spinels (Kaakol et al., 1992), electron delocalization (insulator-to-metal transition in VO_2; Pintchovski et al., 1978) and spin unpairing as in Co_3O_4 and $CaFeO_3$ (Mocala et al., 1992). At high pressure when ΔV becomes positive, metallization and spin pairing may occur.

5.7.3.2. Magnetic collapse: oxides and perovskites

As pressure and temperature are varied, a number of transitions are expected. These may occur together in several groups, such as Mott transition, transitions between band states and localized states, high-spin–low-spin transitions, structural-phase transitions and magnetic-ordering transitions.

Magnetic collapse can occur if the crystal-field splitting becomes larger than the exchange splitting. In such a case, the occupancy of state changes and the magnetic moments collapse. The magnetic collapse occurs by band broadening with pressure, with very little change in the crystal field. Indeed, the crystal-field $t_{2g}-e_g$ splitting is seen to remain the same at all pressures. A uniform decrease in effective DOS with pressure rather than a change in CF splitting (which is low) gives rise to magnetic collapse.

The magnetic properties at very high pressure of FeO, MnO, CoO, NiO and $FeSiO_3^{(pvs)}$ have been investigated by Cohen et al. (1997) using the first-principles linear muffin-tin orbital (LMTO) and linearized augmented plane wave (LAPW) electronic structure methods within the GGA. They computed the anti-ferromagnetic moments for cubic rock salt (B1)-structured FeO, MnO, CoO and NiO and found that all four compounds exhibit magnetic collapse. For FeO, magnetic collapse occurs at relatively

high pressures, whereas for CaO the transition pressure is relatively low (*see also* Section 12.2.1).

$(Mg,Fe)SiO_3$ perovskite containing up to 15% Fe is considered to be the most common mineral in the Earth. In this phase, Fe is in a high-spin state in the A-site and a low-spin state in the B-site at geophysically relevant pressures (135 GPa). In the A-site, magnetic collapse does not occur until 1 TPa whereas, in the B-site, the magnetic moment decreases smoothly from high spin at low pressures to low spin at high pressures. Again, the B-site is much smaller than the A-site. The B-site band-width becomes much larger when Fe is in the B-site; this leads to different magnetic behaviour. When the magnetic collapse occurs, it is governed by the band-width rather than by the crystal field.

Transition-metal sulphides, having a greater overlap of larger sulphur anions, will show larger band-widths and, consequently, lower pressure transitions. For example, in the FeS_2–MnS_2 system, Fe^{2+} is in a low-spin state, whereas dilute Fe^{2+} in MnS_2 iron is in a high-spin state because of the larger molar volume of MnS_2 (compared with FeS_2). Under moderate compression (12 GPa), the Fe^{2+} ions undergo magnetic collapse to the low-spin state. Substitution in a smaller site will also cause a compression effect on Fe^{2+} to induce magnetic collapse at lower pressures. This occurs in Mg(Fe)O, magnesiowüstite, in which iron undergoes magnetic collapse at lower pressures than for FeO. This is because Mg^{2+} ion is smaller in size than Fe^{2+} ion. Also, Fe^{2+} ion in Mg-wüstite will collapse at lower pressures than Fe^{2+} ion dissolved in Fe liquid. The magnetic collapse of Fe^{2+} iron in Mg-wüstite may be responsible for the anomalies observed in the D″ zone above the core.

Magnetic collapse in Co^{2+} would make it more siderophile. This explains the relative depletions of Ni and Co in the silicate mantle. Thus, ultra-high-pressure experiments help one to a better understanding of the partitioning of elements in the lower mantle.

5.7.3.3. Magnetism in phase stability

Magnetism can affect phase stability, lattice distortions, elasticity, EOS, and vibration frequencies.

Magnetism arises from electron spin, which is a vector quantity, behaving like quantum angular momentum. The orbital angular momentum of electron leads to orbital magnetic moments. The orbital moments become important in f-orbital electrons, such as present in rare Earths and lanthanides. When the localized f-electrons interact with delocalized band-like states interesting phase transitions occur with pressure, such as with Ce. d-State electrons get more delocalized than f-state electrons, which are more localized. But localization is also important.

The antisymmetric property of the wave function leads to the Pauli exclusion principle, without which the electrons would fall into the nucleus and no atom will exist! The opposite spin property allows a maximum of two electrons to exist in an orbital. Since electron is indistinguishable one can consider the quantum states to be paired rather than the electrons themselves. In order to lower the total potential energy the electrons are

required to have the same spin. The lowering of potential energy by lining up the spins is to raise the system's kinetic energy. The electronic potential energy favours magnetic while the electronic kinetic energy favours non-magnetic electronic structure.

Under pressure electrons are pushed close together, the bands become wider and the material becomes non-magnetic. The total energy change between magnetic and non-magnetic system is known as exchange energy.

From low temperature as the temperature is raised the magnetic moment directions on each atom will fluctuate and at critical temperature, T_c, in ferromagnetic the moments will disorder.

In antiferromagnets the magnetic moments lie in opposite directions in alternate sites. Under pressure the kinetic energy is lowered. Some ferromagnets under pressure become antiferromagnet, e.g., fcc iron.

5.7.3.4. Magnetic frustration

At the lowest free energy state some have non-collinear spins, and it becomes impossible to transform lattice with perfect antiferromagnetic pattern, (i.e., neighbours with opposite pointing spin), e.g., fcc and hcp structures. Such properties are responsible for anti-Invar effect (high thermal expansivity) as in fcc iron.

5.8. Polyhedral changes

It is known that a closed 3D figure made of rigid triangles can be squeezed or stretched into a new shape without distorting the faces. The concept of flexible polyhedra retaining their volume constant has destroyed the belief that a given set of edge lengths should yield a finite number of shapes.

The formula of Heron, the Greek mathematician (of Alexandria) says that area, x, of a triangle with side lengths (a, b, c) must solve the polynomial:

$$16x^2 + a^4 + b^4 + c^4 - 2a^2b^2 - 2a^2c^2 - 2b^2c^2 = 0.$$

The volume of a tetrahedron has to a satisfy similar but more complicated polynomial. For an octahedron, the polynomial involves 16th powers of the volume. The volume of any polyhedron might also solve some version of Heron's polynomial.

The volume of a polyhedron with fixed side lengths could only change by jumping from one solution of the polynomial to another but if the polyhedron change is gradual, the volume cannot change suddenly; it has to remain constant. A flexible four-sided figure, for example, can change its area without changing the side lengths.

The compression of the individual octahedral configuration is strongly dependent upon both the geometry of the polyhedron itself and the types of, and the connectivity to, the neighbouring polyhedra. The dominant mechanism of compression is usually one of polyhedral rotation and the change in interpolyhedra bond angles. Conversion of corner-shared MO_6 octahedra to various structural patterns is shown in Fig. 5.4.

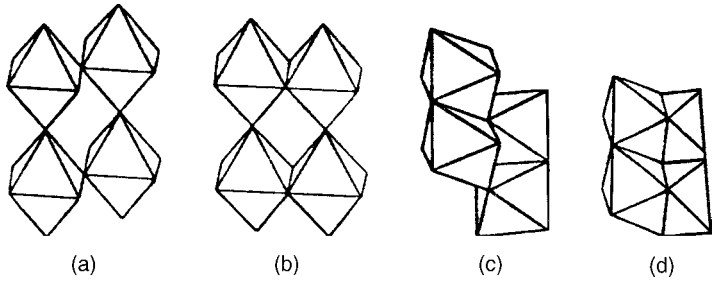

Figure 5.4. Transformation of corner-shared (MO_6) octahedra (a) to edge-shared octahedra (b) to corner and edge-shared octahedra (c) to face-shared octahedra (d). The structure consists of an infinite array of corner-shared octahedra (a), and infinite strings of edge-shared octahedra (c).

The bonding geometry controls the pressure-induced changes of the material's physical characters. Generally, with pressure, the bond-length distortion decreases as the anions tend to approximate close packing.

The degree of polyhedral distortion at high pressure can be characterized with distortion parameters defined (Renner and Lemann, 1986) as

Bond-length distortions (BLD):

$$\mathrm{BLD}(\%) = \frac{100}{n}\sum_{i=1}^{n}\frac{|d_i - \bar{d}|}{\bar{d}} \tag{5-33}$$

Edge length distortion (ELD):

$$\mathrm{ELD}(\%) = \frac{100}{n}\sum_{i=1}^{n}\frac{(x_i - \bar{x})}{\bar{x}} \tag{5-34}$$

Angular distortions (AD):

$$\mathrm{AD}(\%) = \frac{100}{N}\sum_{j}^{N}|a_j| \tag{5-35}$$

$$a_j = \sum_{i=1}^{m}\frac{\alpha_i - \alpha_{\mathrm{ideal}}}{\alpha_{\mathrm{ideal}}} \tag{5-36}$$

where d_i and x_i are the bond length and edge length, respectively, $\bar{d}$ and $\bar{x}$ are the average bond length and edge length in a polyhedron, α is the polyhedral angle and α_{ideal} is the polyhedral angle of a regular polyhedron.

The bulk modulus of a mineral, K, represents the pressure dependence of its molar volume, V, as

$$K = -V(\mathrm{d}P/\mathrm{d}V) = 1/\beta,$$

where β is the volume compressibility of the crystal. At elevated pressure, K generally increases.

Usually, under increasing pressure, SiO_4 tetrahedra become more regular, as do the MgO_8 polyhedra whereas AlO_6 octahedra become more distorted. MO_6 and SiO_4 polyhedra dictate the compressibility of the structure hosting these. A high-valence state of cations in octahedra would lead to a more incompressible structure. The compressibility of Si–O bonding is of great interest because of the transition between 4- and 6-fold coordinated silicon in the Earth's transition zone and lower mantle. The constituent polyhedra of mineral phases in the upper and lower mantle are shown in Fig. 5.5 (*see* caption). The high incompressibility of Si–O bonding makes it difficult to determine the bulk modulus of SiO_4 tetrahedra occurring in the mantle minerals. However, experiments at extended pressures by different workers have demonstrated the Si–O bonding to show a significant compressibility (although over a broad range) (Kudoh and Takeuchi, 1985, Hazen and Finger, 1989; Hugh-Jones and Angel, 1994; Zhang et al., 1997, Zhang et al., 1998).

The crystal volume for an experiment above 20 GPa is more than five times smaller than for an experiment at pressures lower than 10 GPa.

The macroscopic bulk modulus is due to polyhedral compression and tilting of polyhedra about shared-corner linkages. The bulk modulus is related to pressures as

$$K_p \langle d \rangle^3 / S^2 z_c z_a.$$

where K_p is the bulk modulus of the polyhedron, $\langle d \rangle$ is the mean distance between the cation and anion, z_c and z_a are the charges on the cation and anion, respectively, and S is a scaling factor equal to 0.50 for oxides and silicates.

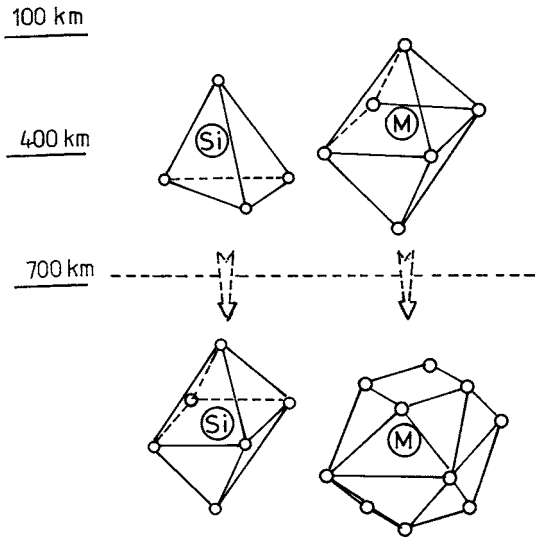

Figure 5.5. Major constituent polyhedra of the mantle mineral phases. In the upper mantle, silicon is coordinated to four oxygens and metal (M) atoms (Mg, Fe, Ca,…) to six oxygens. In the lower mantle, the oxygen coordination of silicon ranges from 4 to 6, and that of metal atoms from 6 to 12 (after Madon, 1992).

Change in the volume of coordination polyhedra is related to the bond parameters, such as the M–O distance (d), coordination number (n), cation radius (r), cation and anion charges (Z_c and Z_a) and ionization (S^2). The volume changes in the direction of α, β and γ in anistropic crystals can be represented as

$$\alpha_v = 1/v\left(\frac{\delta V}{\delta T}\right) \approx 120\left(\frac{n}{s^2 z_c z_z}\right) \times 10^{-6}\,^{\circ}\mathrm{C}^{-1} \tag{5-37}$$

$$\beta_v = -1/v\left(\frac{\delta V}{\delta P}\right) \approx 0.133\left(\frac{\mathrm{d}^3}{s^2 z_c z_a}\right) \times 10^{-6}\,\mathrm{bar}^{-1} \tag{5-38}$$

$$\gamma_v = 1/v\left(\frac{\delta V}{\delta X}\right) \approx \frac{3(r_2 - r_1)}{\mathrm{d}} \tag{5-39}$$

where $X =$ atomic fraction of large cation.

The compressibility in isothermal conditions is defined as

$$\beta_T = -\frac{1}{V}\left(\frac{\mathrm{d}V}{\mathrm{d}P}\right)_T.$$

An increase in the coordination number (by transition, etc.) will increase the polyhedral compressibility. Compression of cation polyhedra in oxides is a fundamental property of the type of polyhedron, essentially independent of the structure type.

The oxides and silicate minerals suffer structural changes. The changes are controlled by the following the observed rules:

(A) With pressure, the lattice volume change is negative because crystal compresses mostly along the axes.

(B) The metal–oxygen bond distance, d, shows an average compressibility, β. In the case of a crystalline phase:

$$\beta = (-1/d)\delta d/\delta P \approx 0.044(d^3/S^2 Z_c Z_a) \times 10^6\,\mathrm{bar}^{-1} (\textit{see}\ \text{Fig. 5.6(a)}).$$

(C) The polyhedral compressibilities (and change in O–cation–O angles) correspond to the total volume compression. The relationship between the bulk modulus and volume for a variety of marerials is shown in Fig. 5.6(a) (Hazen and Finger, 1979).

5.8.1. Elasticity of MgO_6 and SiO_6 octahedra: $MgSiO_3$ ilmenite

The calculated Si–O, Mg–O and O–O bond lengths and the polyhedral volume decrease continuously with increasing pressure.

The polyhedral bulk moduli obtained from fits to third-order Birch–Murnaghan EOS are

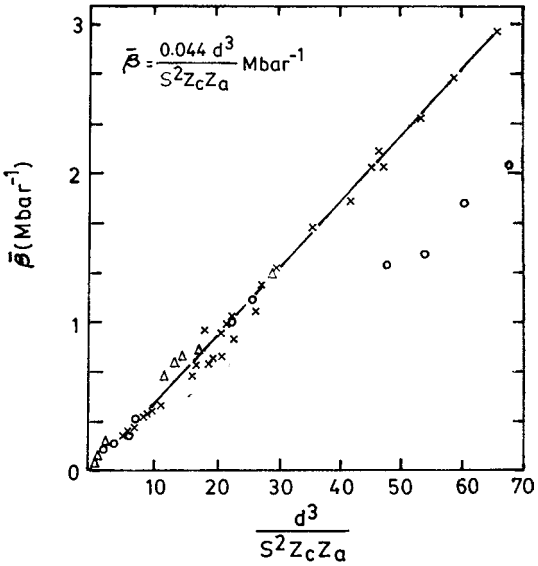

Figure 5.6(a). The bulk modulus-volume relationship for polyhedra a variety of materials (Hazen and Finger, 1979, © 1998 Mineralogical Society of America).

for SiO_6 octahedron:

$K = 338\,\text{GPA}$ (when $K'_{T0} = 5.05$)

and, for MgO_6 octahedron:

$K = 172\,\text{GPA}$ (when $K'_{T0} = 3.96$).

Thus, MgO_6 octahedra are ~ 2 times more compressible than SiO_6 octahedra.

The degree of distortion (QE and σ^2) in both MgO_6 and SiO_6 octahedra decreases under compression, but the distortion of the former decreases more rapidly with pressure (Fig. 5.6(b)).

The ilmenite structure consists of alternating MgO_6 and SiO_6 octahedral layers normal to the *c*-axis. The high elastic anisotropy of ilmenite is connected to the large contrast in the compressibility of the two types of octahedra, namely MgO_6 and SiO_6. Compression along the *c*-axis is jointly determined by the more compressible MgO_6 and less compressible SiO_6 octahedra, whereas compression along the *a*-axis is only controlled by the less compressible SiO_6 octahedra (Karki et al., 2000).

5.8.2. Anisotropic deformation: decompression

Cubic crystals deform isotropically while the deformation of anisotropic crystal is determined by the anisotropy of bond strength and shearing. Negative linear thermal expansion is common in monoclinic and triclinic crystals.

Highly ansiotropic deformation in oblique-angle crystals, such as felspars, amphiboles, pyroxenes and micas, cause decompression of rocks, increase in fluid permeability and ore deposition through metamorphism. The anisotropy of felspars and

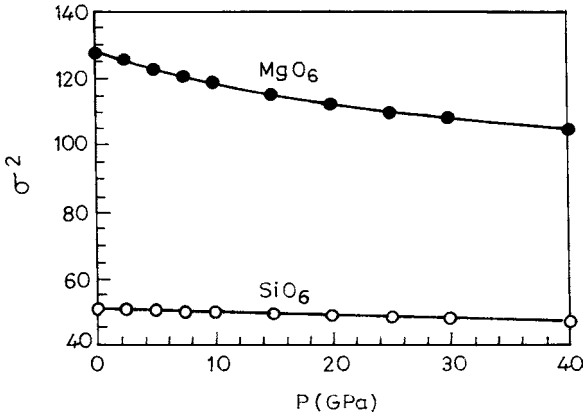

Figure 5.6(b). Pressure variation of distortion parameters (a) quadratic elongation (QE) and angle variance (σ^2) for MgO_6 and SiO_6 octahedra.

quartz ($\alpha \rightarrow \beta$) transitions causes volume change by 0.6% (at 573°C), and causes decompression of host rocks such as granite, etc. Similarly, highly anisotropic thermal expansion of calcite is responsible for the thermal decompression of marbles.

5.8.3. Radius ratio and coordination changes

The ratio of the ionic radii of cation (R_c) and anion (R_a) determines the coordination number of the cation. When this ratio (R_c/R_a) ranges between 0.414 and 0.732, octahedral coordination occurs. In the case of tetrahedral (4-fold) coordination, this ratio is less than 0.414 while, for cubic (8-fold) and dodecahedral (12-fold) coordination, this ratio falls below 0.732.

In the high-pressure (denser) polymorphs, the coordination number of Si and Mg increases (especially in perovskite structure). This is in consequence of the increase in radius ratio for most cations, which show less compressibility compared with the highly polarizable oxygen anions. Divalent cations (except low-spin ones) are more susceptible to a pressure-induced increase in coordination number than are the trivalent cations. Thus, at high pressure, divalent high-spin cations, e.g., Fe^{2+}, Mn^{2+}, Co^{2+} and Cr^{2+}, acquire a coordination number greater than six. These cations occur in the A-sites of perovskites in the lower mantle; whereas higher-valent states, such as Ti^{4+}, Ti^{3+}, V^{3+}, Cr^{3+} and Fe^{3+}, remain in octahedral sites throughout the mantle and stabilize the B-sites of perovskite and also the structure of magnesiowüstite.

In the Earth's deep interior as pressure increases the coordination number, the cation–oxygen distance increases. Thus, high-pressure phases show greater compressibility than their low-pressure polymorphs. The volume reduction with pressure causing discontinuous structural changes is countered by the increase in cation coordination. Transformations such as those of $MgSiO_3$ from pyroxene to garnet to perovskite result in large density increases (from increased atom-packing efficiency).

5.8.4. Five-fold coordination: silicon and titanium

Five-fold coordination of silicon by oxygen (^{v}Si) has been predicted by theoretical studies of the effects P and T on silicate melts and glasses (Jin et al., 1994; Badro et al., 1996) and is inferred experimentally by ^{29}Si NMR and vibrational spectroscopy in alkali silicate liquid and glasses (e.g., McMillan et al. 1994; Farber et al., 1996). ^{v}Si has been proposed as playing a role in the dissolution of silicates (e.g., Xiao and Lasaga, 1996).

Although ^{v}Si is suspected in high-pressure silicates, no crystalline phase of silica containing ^{v}Si have yet been observed. It may form part of the network of high-pressure amorphous phases and be hypothetized in high-temperature SiO_2-rich melts or glasses.

The first-principles electronic structure method and inter-atomic potential studies show that ^{v}Si species are gradually replaced by ^{iv}Si and ^{vi}Si with increasing pressure (e.g., Kubicki et al., 1993). Recent molecular-dynamic simulations on α-quartz under non-hydrostatic stress found evidence for a crystalline phase of SiO_2 composed entirely of SiO_5 groups (Badro et al., 1996). The detail of the SiO_5 polyhedron is shown in Fig. 5.7. Badro et al. (1997) performed theoretical calculations in silica as a function of non-hydrostatic stress. Molecular-dynamics calculations reveal a crystalline-to-crystalline transiton from α-quartz to a ^{v}Si- bearing phase at high P in the presence of deviatoric stress. The structure of the phase possesses $P3_221$ space-group symmetry. First-principles calculations within the local-density approximation, as well as molecular dynamics and energy minimization with inter-atomic potentials, show this phase to be mechanically and energetically stable with respect to quartz at high pressure.

Upon decompression, the ^{v}Si phase reverts to α-quartz through an intermediate four-coordinated phase and an unusual isosymmetrical phase transformation. The change in Si–O bond length and Si–O–Si angle with molar volume on decompression of the penta phase is shown in Fig. 5.8. The calculated powder X-ray diffraction pattern of SiO_2 penta for a relaxed structure ($P = 16$ GPa) is shown in Fig. 5.9. The results suggest the

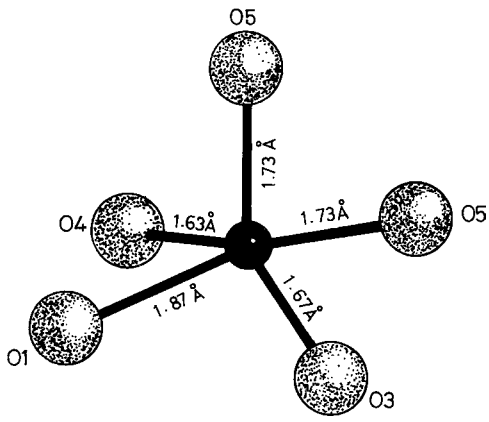

Figure 5.7. Detail of the SiO_5 polyhedron showing the position of the atoms and bond lengths calculated by LDA ($P = 16$ GPa) (from Badro et al., 1997, © 1997 American Physical Society).

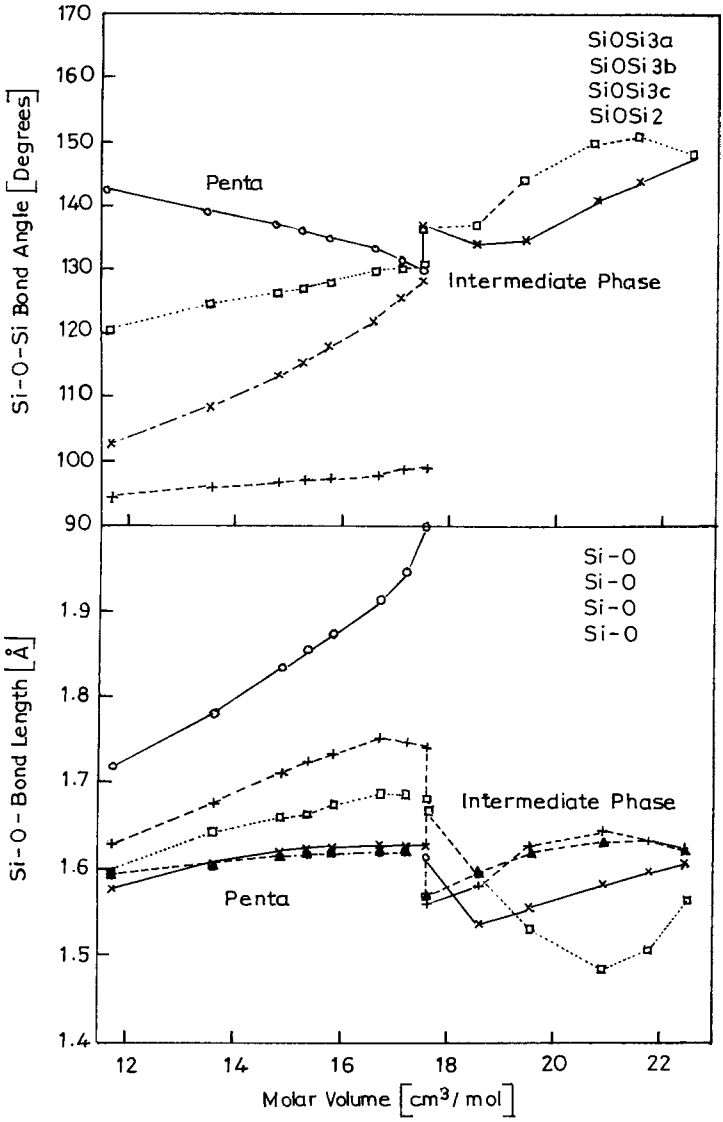

Figure 5.8. Structural variations in the penta phase as a function of volume during decompression Si–O–Si bond angles (top) and bond distances (bottom) (Badro et al., 1997, © 1997 American Physical Society).

importance of the application of non-hydrostatic stress conditions in the design and synthesis of novel materials (Badro et al., 1997).

Five-coordinated silicon is presumed to be present in an intermediate complex during dissociation and polymerization processes of silicates (e.g., Lasaga and Gibbs, 1990) and also during viscous flow and diffusion processes in silicate melts (Zue et al., 1991).

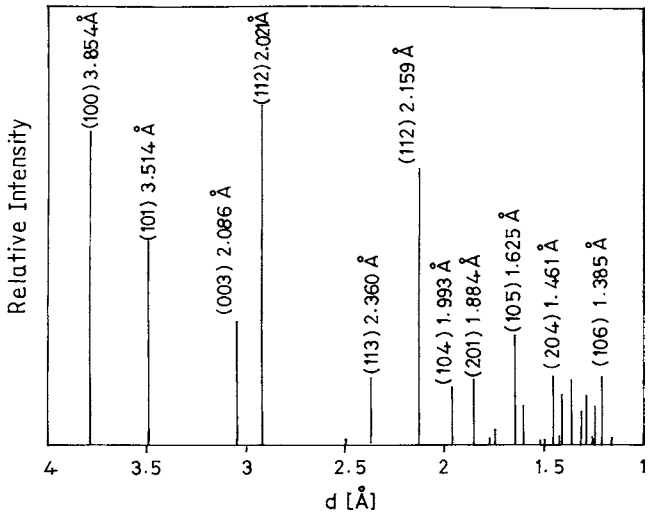

Figure 5.9. Calculated powder X-ray diffraction patter of the SiO_2 penta for the relaxed structure ($P = 16$ GPa) (from Badro et al., 1997, © 1997 American Physical Society).

Kanazaki et al. (1991) and Kudho and Kanazaki. (1998) synthesized α-$CaSi_2O_5$ phase at high P, T (12 GPa/1,500°C) and found the existence of a square-pyramid 5-fold coordination of silicon in the structure.(*see* Figs. 5.10 and 5.11).

Assuming 1.4 Å as the ionic radius of oxygen, the ionic radius of $^{[5]}$Si is obtained as 0.33, which is intermediate between 0.26 Å for $^{[4]}$Si and 0.40 Å for $^{[6]}$Si (Shannon- and Prewitt, 1969). Penta-coordinated silicon has been reported in organic compounds. In all these structures, the [SiA_5] groups are more or less distorted trigonal bipyramids.

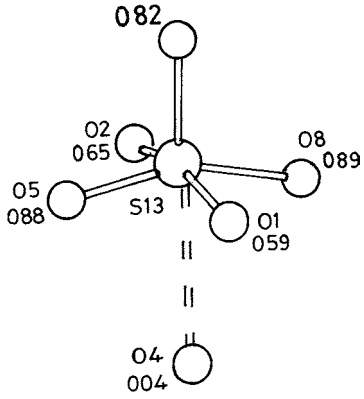

Figure 5.10. Square-pyramid coordination environment about Si_3. *Numbers* indicate bond valences. The sixth Si–O distance is indicated by *broken line* (Kudoh and Kanzaki, 1998, © 1998 Springer-Verlag).

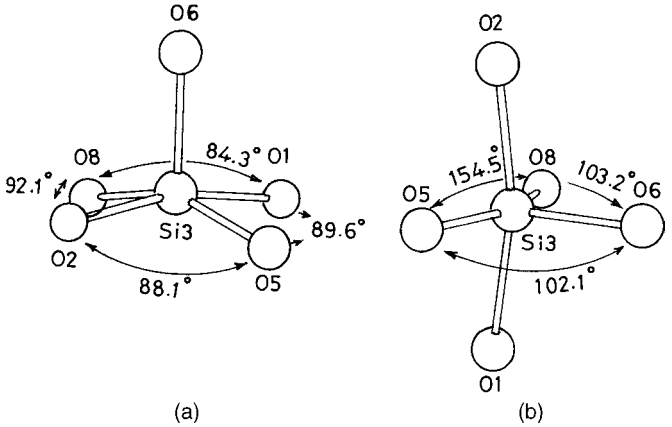

Figure 5.11. (a) [5]Si coordinated by five oxygens atoms with Si_3-O_6 being vertical. (b) As above with Si_3-O_6 being *horizontal* (Kudoh and Kanzaki, 1998, © 1998 Springer-Verlag).

The square pyramid 5-fold coordination of Ti by O has been reported for $Ba_2TiSi_2O_8$ (Moore and Louisnathan, 1967) and for Na_2TiSiO_5 (Nyman and O'Keeffe, 1978). In the case of the TiO_5 square pyramid, the four longer Ti–O bonds are tetragonally placed and the fifth oxygen atom makes a shorter Ti–O bond, forming a highly compressed square pyramid.

5.8.5. Thermal expansivity and deformation equivalence (α/β)

The mean linear coefficient of thermal expansion, $\bar{\alpha}$ ($\bar{\alpha} = \alpha_v/3$), where α_v is the coefficient of volumetric expansion of a coordination polyhedron formed by essentially ionic bonds, has simple reversible relations to Pauling bond strength (cf. equation (5-37)):

$$\bar{\alpha}_{1000} = \frac{1}{\alpha}\frac{\delta d}{\delta T} \approx 4.0(4)\left(\frac{n}{S^2 Z_c Z_a}\right) \times 10^{-6}\,^{\circ}\mathrm{C}^{-1} \tag{5-40}$$

where d is the cation–anion separation, n is the coordination number of the cation, Z_c and Z_a are cation and anion charges, respectively, and S^2 is the ionic-bond coefficient, which is equal to ~ 0.5 for oxygen compounds, as stated earlier. Thus, all types of polyhedra with a definite cation and anion have the same parameter α, which can be used for predicting the effect of T on the polyhedra and thus does not depend on structural bonds in the polyhedra. Furthermore, all coordination polyhedra with similar values of Pauling bond strength have a similar coefficient α (*see* Fig. 5.12). For example, in octrahedra with divalent Mg, Co, Fe, Cd, Mn, Ca, Ba and Sr, the thermal expansion ($\alpha_{1,000}$) equals $14 \pm 1 \times 10^{-6}\,^{\circ}\mathrm{C}^{-1}$.

Molar volume at 1 bar is expressed as function of T:

$$V(1,T) = V^0_{1,\mathrm{Tr}} \exp\left(\int_{Tr}^{T} \alpha(T)\mathrm{d}T\right) \tag{5-41}$$

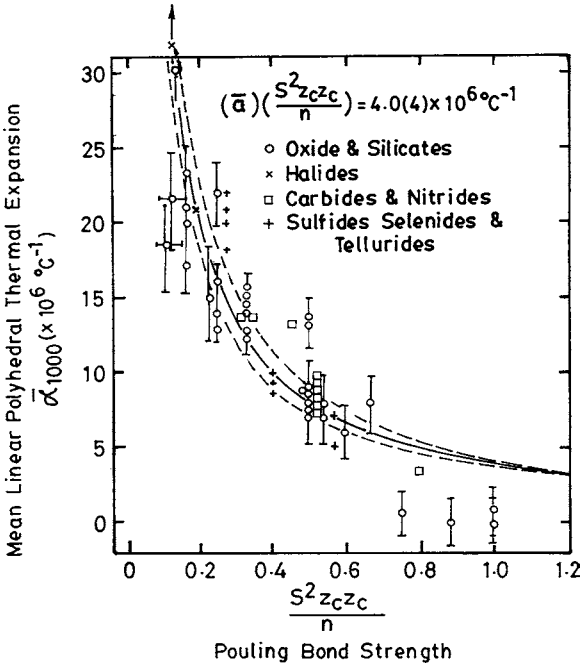

Figure 5.12. The relationship between the mean linear polyhedral thermal expansion vs the pauling bond strength.

where $V^0_{1,\mathrm{Tr}}$ is molar volume at 1 bar, Tr is the transition temperature and $\alpha(T)$ is the thermal expansion, depending on temperature as

$$\alpha(T) = \alpha_0 + \alpha_1 T + \alpha_2 T^2 + \alpha_3 T^3. \tag{5-42}$$

The thermal expansivity at ambient pressure, σ_{T0}, can be assumed as

$$\alpha_{\mathrm{T0}} = a + bT.$$

All crystalline substances can be represented in $P-T-X$ space by surfaces of a constant molar volume (isochroic surfaces). For many substances, the isochroic surfaces coincide with isostructural surfaces.

The deformation equivalence is measured as the ratio of thermal expansivity, α, with compressibility β. The minerals in a single zone have a similar deformation equivalence, α/β. This α/β value increases with pressure in depth. As a consequence of a decrease in the temperature gradient, the expansion slows down and the proportion of compression increases. The α/β relation obtained for a polyhedron (Hazen and Finger, 1982) is

$$\alpha/\beta \approx 90\, n/\mathrm{d}^3 \text{ bar/°C}.$$

Evidently, the higher coordination numbers (n) of the atoms in deep-seated phases determine their greater density and deformation equivalence, α/β. All Mg, Fe^{2+}, Al and Fe^{3+} octahedra have $\alpha/\beta \approx 65$ bar/°C. Many silicate minerals reveal $\alpha-\beta$ inverse relationships. Even rutile, having a more covalent bonding, demonstrates an inverse relationship.

In subducting slabs, the rocks in depth zones under higher temperature and pressure expand and compress simultaneously. The average α/β increases with depth of the zone (h), rock density (ρ), P-wave velocities within the zone (V_P) and the mean symmetry of the minerals in the zone.

Molar volume as a function of pressure and temperature can be calculated using the Murnaghan equation:

$$V(P,T) = V(1,T)\left(1 + \frac{K'_P P}{K_T}\right)^{-1/K'_P} \tag{5-43}$$

where K_T is isothermal bulk modulus expressed as

$$K_T = 1/(\beta_0 + \beta_1 T + \beta_2 T^2 + \beta_3 T^3)$$

and K'_P is the pressure derivative of the bulk modulus, which, in some cases, has a temperature dependence

$$K'_P = K'_{P\,Tr} + K'_{PT}(T - \mathrm{Tr})\ln(T/\mathrm{Tr})$$

$K'_{P\,Tr}$ is the pressure derivative of the bulk modulus at transition temperature, (Tr) and K'_{PT} is its temperature derivative.

The specific temperature dependence of the bulk modulus of oxides and silicates is available from Saxena et al. (1993). It is advisable to check that employment of the Murnaghan equation and the Birch–Murnaghan equation gives close results in the studied P, T range.

5.8.6. Volume compressibility: negative

Under hydrostatic pressure (P), most materials contract in all directions. Therefore, the volume compressibility $(-\mathrm{d}V/V\,\mathrm{d}P)$, area compressibility $(-\mathrm{d}A/A\,\mathrm{d}P)$ and linear compressibilities $(-\mathrm{d}L/L\,\mathrm{d}P)$ are all positive. Materials are thermodynamically forbidden to have negative volume compressibilities but some crystals having negative linear compressibilities have been known; e.g., lanthanum niobate, cesium dihydrogen phosphate (Prawer et al., 1985) and some others.

Materials having negative area compressibilities might be used as electrode clamps to provide a sensitivity increase by an order of magnitude for ferroelectric pressure sensors. However, materials with negative compressibilities are rare. The pressure-induced expansion of the negative-area-compressibility material forces a ferroelectric sheet to increase in area when pressure is applied. (*Note*: negative compressibility may be relevant in muscular hydrostats, such as those found in worms.)

5.8.6.1. Relative compressibilities

Relative compressibility can be measured quite precisely from relative volumes of crystals at several pressures:

$$\beta_1/\beta_2 \approx [(V_P/V_0)_1 - 1]/[(V_P/V_0) - 1], \tag{5-44}$$

where β_1 and β_2 are compressibilities of two different crystals,1 and 2, and V_0 and V_P are their unit-cell volumes measured at ambient pressure and high pressure.

Small compressibility differences in compositionally similar sites of wüstites (Hazen, 1981), felspars (Angel et al., 1988), pyroxenes (McCormick et al., 1989), wadsleyites (Hazen et al., 1990) and silicate spinels (Hazen, 1993) have been documented.

5.8.7. Thermodynamic parameters and EOS

One of the most important thermodynamic parameters for high $P-T$ calculations is the unit-cell volume of a mineral. Its variation with P and T is described by its EOS with three components: (1) compressibility at ambient temperature, (2) thermal expansivity at ambient pressure and (3) cross-derivative terms describing the effect of pressure on thermal expansivity, equivalent to the effect of temperature on compressibility. For accurate thermodynamic calculations, each component should be measured at relevant $P-T$ conditions. EOS measurements are useful for constraining lower $P-T$ metamorphic reactions.

The EOS presents the thermodynamic relations between V, T, P and other external fields. The EOS (when β is constant) can be written as a Taylor series or polynomial expansion of P in terms of V. Birch–Murnaghan EOS is capable of treating compression of up to factors of ~ 2 (i.e., $V/V_0 = 0.5$). For hydrogen and helium V/V_0 equals 0.15.

EOS data play a central role in efforts to describe the mineralogical structure and convective dynamics of the Earth's deep interior. Experiments defining the molar volume as a function of pressure clarify the nature and character of phase transitions that may occur in the crust and mantle and, furthermore, provide valuable constraints on models of bonding in minerals.

5.8.7.1. P–V–T data and EOS

An EOS reflects the underlying interaction potential among the ions and electrons that make up a crystal. The $P-V-T$ EOS plays a central role in study of the Earth's deep interior. Using the EOS, one can calculate the densities and bulk-wave velocities of candidate materials at lower-mantle P, T conditions. By fitting the densities and wave velocities to seismic observations, one can test models for the bulk chemistry of the lower mantle (e.g., Bina, 1995; Jackson, 1998). In addition, the EOS enables us to determine the depth dependence of important thermoelastic parameters, such as the thermal expansivity and temperature sensitivity of the bulk modulus. The latter is necessary for comparing seismic-bulk velocity profiles with laboratory data.

Recently, new methods using a diamond cell combined with laser or resistance heating have been used to obtain $P-V-T$ EOS data directly at lower-mantle $P-T$ conditions (e.g., Fiquet et al., 1998; Shim et al., 1998; Saxena et al., 1999).

Under pressure, the changes in volume V is expressed in terms of the bulk modulus, K:

$$V(\delta_p/\delta_v)_T = -K_T.$$

An expansion of the bulk modulus in terms of pressure is

$$K(P) = K_0 + K_0'P + \tfrac{1}{2}K_0'P^2 + \cdots$$

where K_0 is the value for $P = 0$, K_0' is the first-pressure derivative at $P = 0$ and so on.

Using only the first two terms and integrating the Murnaghan equation (for a crystal) empirically becomes

$$P = K_0/K_0'[(V_0/V)^{K_0'} - 1] = K_0/K_0'[(d_0/d)^{3K_0'} - 1] \tag{5-45}$$

where d is the lattice parameter.

The values of K_0 and K_0' are obtained from precise measurements of elastic constants; and X-ray data for the $d(P)$ fit of this equation (within the empirical error for $P < 0.2K_0$). A typical value of K is 75 GPa. To describe $d(P)$ at higher pressure, higher-order equations can be used but experimental data of K at high pressures are often not readily available.

5.8.7.2. Birch EOS

The Birch–Murnaghan EOS (Birch, 1947) has often been used to fit isothermal compressional data. When the cell volume data do not follow any isothermal experimental path, the Birch–Murnaghan EOS for diverse temperatures can be fitted to the $P-V-T$ data. It is important to indicate that any $V(P,T)$ data point should be reached by taking a realistic thermodynamic path. A standard way to fulfil the thermodynamic necessity is to heat the ambient volume V_0 to a temperature T and then compress the expanded volume $V(0,T)$ along the isothermal to reach the $V(P,T)$. The modified Birch–Murnaghan equation is thus written as

$$P = 3K_T f(1+2f)^{5/2}[1 - 3/2(4-K')f + \cdots] \tag{5-46}$$

where

$$K_T = K_{T0} + \mathring{K}(T-300), \qquad K' = \delta K/\delta P, \qquad \mathring{K} = \delta K/\delta T$$

$$f = 1/2[(V_T/V_{PT})^{2/3} - 1], \qquad V_T = V_0 \exp\left(\int \alpha_v(0,T)\mathrm{d}T\right)$$

where V_0 is the cell volume at ambient conditions, V_T at high T and V_{PT} at high $P-T$ conditions and thermal expansion at zero pressure is $\alpha_{v0} = \alpha_v(0,T) = a + bT - c/T^2$ (T in kelvin) and f is called the Eulerian strain (*see* equation (2-9)).

In thermal expansion, the C/T^2 term and the high-order derivatives of bulk modulus K'', $\mathring{K}$ and $\delta^2K/\delta P\delta T$ are generally ignored. The equation is a modified

isothermal Birch–Murnaghan EOS by replacement of K_0 with K_T and substituting V_0/V_P with V_T/V_{PT} so that temperature effects are incorporated.

Generally, four iterative steps, where each step has different constraints on starting parameters, can be taken to achieve the final fitting results:

Step 1: fix α_{v0} and fit K_{T0}, K', $\mathring{K}$

Step 2: fix K_{T0}, K' and fit α_{v0}, $\mathring{K}$

Step 3: fit α_{v0}, K_{T0}, K', $\mathring{K}$ simultaneously

Step 4: Combine all data and fit α_{v0}, K_{T0}, K', $\mathring{K}$ simultaneously.

The Birch equation assumes that the underlying potential can be represented as a series in $(1/r^{2n})$. The commonly used third-order Birch equation (with parameters V_0, K_{T0} and K'_{T0}) includes $n = 1$, 2 and 3.

However, there is no fundamental reason to expect $(1/r^{2n})$ to represent inter-atomic interactions well, so it is not surprising that the Birch equation is not perfect.

The Vinet and Holzapfel equations converge smoothly to a constant at large volumes, being consistent with physically based potentials.

5.8.7.3. Equations of state: density ratio

The Birch–Murnaghan EOS is widely used amongst geoscientists. The two important pressure–density relationships used are as follows.

The *first-order* Birch–Murnaghan EOS for many solids is approximately

$$P = 3/2K_0[(V_0/V_p)^{7/3} - (V_0/V_p)^{5/3}] \tag{5-47}$$

where K_0 is the bulk modulus at zero pressure (i.e., at 1 bar, $\cong 10^{-4}$ GPa) and V_0 and V_p are volumes at room and elevated pressure, respectively. Considering (V_0/V_p) equals (ρ/ρ_0), the following relations hold:

Birch–Murnaghan (*third order*):

$$P = (3/2)K_0[(\rho/\rho_0)^{7/3} - (\rho/\rho_0)^{5/3}]\left\{1 + 3/4(K'_0 - 4)[(\rho/\rho_0)^{2/3} - 1]\right\} \tag{5-48}$$

Birch–Murnaghan (*fourth order*):

$$P = 3/2K_0[(\rho/\rho_0)^{7/3} - (\rho/\rho_0)^{5/3}]\left\{1 + 3/4(K'_0 - 4)[(\rho/\rho_0)^{2/3} - 1] + 3/4[K_0K''_0 + (K'_0 - 4)(K_0 - 3) + 35/9][(\rho/\rho_0)^{2/3} - 1]^2\right\}$$

The EOS can be expressed as a function of density via $C = \rho/\rho_0$.

The *second-order* Birch–Murnaghan EOS appears as

$$P = \frac{3K_{T0}}{2}(C^{7/3} - C^{5/3}) \tag{5-49}$$

Likewise, the *third-order* Birch–Murnaghan EOS becomes

$$P = \frac{3K_{T0}}{2}(C^{7/3} - C^{5/3})\left[1 - \frac{3}{4}(K'_{T0} - 4)(C^{2/3} - 1)\right] \tag{5-50.1}$$

The third-order Birch–Murnaghan equation has been widely used to decribe the isothermal compression of mantle minerals

$$P_{st} = \frac{3}{2}K_{T0}\left[\left(\frac{V_0}{V}\right)^{7/3} - \left(\frac{V_0}{V}\right)^{5/3}\right]\left\{1 - \frac{3}{4}(4 - K'_{T0})\left[\left(\frac{V_0}{V}\right)^{2/3} - 1\right]\right\} \tag{5-50.2}$$

where K_{T0} is the isothermal bulk modulus, K'_{T0} is the pressure derivative of the bulk modulus and V_0 is the volume. The subscript 0 refers to ambient conditions (1 bar and 300 K).

The Vinet EOS comes as

$$P = 3K_{T0}C^{2/3}(1 - C^{-1/3})\exp\left(\frac{3}{2}(K'_{T0} - 1)(1 - C^{-1/3})\right) \tag{5-51}$$

These equations accurately describe the compressional behaviour of real materials.

However, better precision is attained by ab initio calculations, which provide not only a test data set but also enable us to calculate the internal energy of a system. These, therefore, provide independent means of calculating γ through the Mie–Grüneisen relation.

The volume at simultaneous pressure and temperature can be inferred from the Mie–Grüneisen EOS:

$$P_{300\ K} = (P_{th} - P_{th\ 300\ K})$$

where $P_{300\ K}$ is the static pressure at 300 K, obtained by using available experimental room temperature compression data to a third-order Birch–Murhaghan EOS:

$$P_{300\ K} = \frac{3}{2}K_0\left[\left(\frac{V_0}{V}\right)^{7/3} - \left(\frac{V_0}{V}\right)^{5/3}\right]\left[1 + \frac{3}{4}(K'_0 - 4)\left(\left(\frac{V_0}{V}\right)^{2/3} - 1\right)\right] \tag{5-52}$$

where P_{th} and $P_{th\ 300\ K}$ represent the thermal pressure at a given pressure and temperature and the thermal pressure at 300 K, respectively. P_{th} is related to the vibrational Helmholz free energy F_{vib}. as

$$P_{th} = -\left(\frac{\delta F_{vib}}{\delta v}\right)_T$$

The usual experimental technique employs multi-anvil apparatus and synchrotron radiation (e.g., Martinez et al., 1996). In this set-up, P and T can be controlled and measured, large sample volumes can be employed for high-quality data and nearly hydrostatic pressure distribution is achieved. The synchrotron radiation can be relatively easily handled.

The isothermal compression data can also be analyzed using the Murnaghan EOS:

$$\frac{V}{V_0} = \left(1 + \frac{K'_{T0}}{K_{T0}}P\right) - \frac{1}{K'_{T0}} \tag{5-53}$$

The two EOS have different assumptions concerning the second-order pressure derivative of the bulk modulus K''_{T0}. K''_{T0} is zero in the Murnaghan EOS, while it has a non-zero negative value in the Birch–Murnaghan EOS. It is often assumed that K''_{T0} has more effect on the refinement of K'_{T0}.

5.8.8. Bulk moduli: isothermal and isentropic

Silicates may be modelled as ionic compounds with bond strength determined to a first approximation by Coulombic forces. Bridgeman (1923), for example, demonstrated empirical inverse correlations between bulk modulus and molar volume and described his results in terms of an electrostatic model of inter-atomic forces. Bulk modulus–volume relationships have since become useful for predicting the behaviour of oxides, halides, silicates and many in the isomorphous and isoelectronic series (Anderson and Anderson, 1970).

The isothermal and isentropic bulk moduli are distinguished by employing the relation

$$K_S = -V\left(\frac{\delta V}{\delta P}\right)_S \tag{5-54}$$

where K_s is the isentropic bulk modulus at reference P (usually 1 bar), V is molar volume and $(dV/dP)_S$ is the change in molar volume with pressure at constant entropy. Conversion of K_S to the isothermal bulk modulus (K_T) can be calculated from the relationship:

$$K_T = \frac{K_S}{(1 + \alpha\gamma T)} \tag{5-55}$$

where α is the coefficient of thermal expansion and is defined as

$$\alpha = \frac{1}{v}\left(\frac{\delta V}{\delta T}\right)_P \tag{5-56}$$

with V the molar volume, T the temperature at constant pressure and γ is the thermal Grüneisen parameter, which is defined as

$$\gamma = \frac{\delta \ln \theta}{\delta \ln V} = \frac{\alpha K_s}{\rho C_P} \tag{5-57}$$

with θ the Debye temperature and C_P the specific heat at constant pressure.

As a function of pressure, the $P-V$ EOS provides a determination of density ρ and bulk modulus K_S (or K_T), or bulk-sound velocity $V_B (= K_S/\rho)$.

The stability and thermodynamic properties can be derived from the quasi-harmonic lattice dynamics employing parameter-free pair potentials derived from the MEG formulation.

By neglecting second- and third-order derivatives, the bulk modulus at room temperature can be expressed as

$$K_T = K_{T0} + (\delta K_T/\delta T)_P(T - 300\ \mathrm{K})$$

whereas the unit-cell volume is given by

$$V_{T0} = V_0 \exp\left(\int \alpha_{T0}\, dT\right).$$

Compare this with the molar volume shown by equation (5-43).

5.8.8.1. K of mineral mixture: Reuss bound and Voigt bound

Watt et al. (1976) have shown that, for crystalline materials, the bulk modulus (K^*) of a mixture is bounded by the sum of the bulk moduli (K_i) as a function of volume fraction (v_i) and the sum of compressibilities (K_i^{-1}) as a function of volume fraction:

$$K_R^* = \left(\sum_{i=1}^{n} v_i/K_i\right) \leq K^* \leq \sum_{i=1}^{n} v_i K_i = K_v^*$$

The *Reuss bound* (K_R^*) is calculated for the case of equal stress throughout an isotropic mixture, whereas the *Voigt bound* (K_v^*) is calculated for uniform strain in an isotropic aggregate. (*Note*: In the case of a melt, the real condition lies somewhere between the ideal conditions of uniform stress and uniform strain in the structure.)

5.8.8.2. Crystal-field spectra

The velocities of seismic waves are influenced by the bulk modulus and rigidity parameters. From the measurements of pressure-induced variation in CF spectra of transition-metal-bearing minerals, the polyhedral bulk moduli of silicate and oxide minerals can be determined.

From the spectrally determined bulk modulus at room pressure, K_0^s, one obtains the first-order Birch–Murnaghan EOS as

$$K_0^s = 2/3P[(\Delta_P/\Delta_0)^{7/5} - (\Delta_P/\Delta_0)]^{-1}$$

where Δ_0 and Δ_P are the crystal-field splitting parameters at room and elevated pressure, respectively. The polyhedral moduli determined from high-pressure X-ray data conform closely to those obtained from crystal-field spectra at high pressures. The higher coordination sites in a crystal system in general show higher compressibilities (Hazen and Finger, 1982) whereas a large CFSE of a cation at a site reduces the compressibility. For example, the $[CrO_6]$ octahedron shows poor compressibility because of very large CFSE of Cr^{3+} at octahedral sites.

In the upper mantle, olivine and pyroxenes are anisometric and the value of polyhedral bulk moduli shows polarization dependence. The cations in these show a tendency to order in very distorted coordination polyhedra leading to pleochroic spectra, which makes the pressure-dependence spectral evaluation difficult. In the lower mantle, fortuitously, the major phases are cubic or their polyhedral sites are also

cubic, e.g., spinel, garnet, perovskite and periclase. In the determination of the bulk moduli, the pressure dependence of the spectral shift, therefore, becomes more reliable (*see* Section 4.4.2).

5.8.9. Velocity–volume relationship

To interprete the lateral velocity anomalies in terms of lateral temperature anomalies, the following relationship in logarithmic form is useful:

$$\delta T = \frac{(\delta \ln \rho / \delta \ln V)}{\alpha} x\, \delta\, V \tag{5-58}$$

where δV is the velocity anomaly, α the thermal expansion coefficient and ρ the density, while the velocity variation is due to a temperature variation. The isobaric value of $(\delta \ln \rho / \delta \ln V)_P$ yields the isothermal value. (*Note*: $\ln(\rho/\rho_0) = -\ln(V/V_0)$.)

The linear relationship between velocity and volume requires that the value of $(\delta \ln \rho / \ln V)_T$ increases with pressure. The linearity with temperature requires that $(\delta \ln \rho / \delta \ln V)_P$ decreases with increasing temperature.

The velocity–volume functions of alkali halides NaCl and KCl are nearly the same at room pressure and temperature (near or above the Debye temperatures of these halides). Hence, the isobaric and isothermal derivatives of $(\delta \ln \rho / \delta \ln V)_P$ are also nearly the same. The value of the elastic (or anharmonic) contribution to $(\delta \ln \rho / \delta \ln V)_P$ appears to increase from the 1-atm values as pressure increases.

The relationship between the isothermal and isobaric values of $(\delta \ln \rho / \delta \ln V)$ can be obtained from

$$\left(\frac{\delta \ln v}{\delta T}\right)_V = \alpha \left[\left(\frac{\delta \ln v}{\delta \ln \rho}\right)_T - \left(\frac{\delta \ln v}{\delta \ln \rho}\right)_P\right] \tag{5-58.1}$$

From the above equation, one can derive the hypothesis that $(\delta \ln \rho / \delta \ln V)_P$ increases with depth (Yuen et al., 1993). The linear velocity–volume relationship requires that $(\delta \ln \rho / \delta \ln V)_T$ increases with pressure or decreasing volume. The isobaric $(\delta \ln \rho / \delta \ln V)_P$ should increase with depth as intrinsic anharmonicity decreases with depth.

Chopelas et al. (1996) observed that the velocities of sound in minerals (pyrope, YAG, Al_2O_3, $MgAl_2O_4$ and MgO) are linear with volume as long as no phase change or change in compressional mechanism occurs.

5.8.10. Velocity–density relationship: rules

Usually, four velocity–density systematics are used in the geophysical interpretation of seismic velocities in the Earth's interior: (a) the $V_P - \rho$ relationship (Birch, 1961), (b) the $\phi - (\rho/\bar{M})$ relationship (Anderson, 1967), (c) the $V_B - \rho$ relationship (Wang, 1968) and (d) the bulk modulus–volume relationship (Anderson and Anderson, 1970). These are discussed in the following.

(a) *Birch Law* (1961). The relationship between V_P and ρ for various silicates and oxides takes the form of a linear equation $V_P = a(M) + b\rho$ where $a(\bar{M})$ and b are material parameters. Similar relationships between V_s and ρ are also fairly established (Liebermann, 1970).

(b) *The $\phi-(\rho/\bar{M})$ relation.* Anderson's (1967) seismic EOS, based on data for a set of rocks and minerals with $\bar{M}$ values in the range 18–34, is

$$\rho_0/\bar{M} = 0.048\phi^{0.323\pm0.12} \ (\rho_0 \text{ is density at zero pressure}).$$

(c) $V_{B-}-\rho$ *relation*. A linear relationship between bulk velocity V_B $(= (\phi)^{1/2})$ and ρ is established (Wang, 1968). V_B is nearly proportional to V_P and should depend on $\bar{M}$ as well as on ρ, just as V_P does.

(d) *Bulk modulus–volume relationship*. The scaling relationship between bulk modulus K_0 and specific molar volume V_0 at ambient conditions is in the form of $K_0V_0^x =$ constant. For constant crystal structure, $x \approx 1$; when $\bar{M}$ is constant, the value of x is taken as ≈ 4 (Shankland and Chung, 1974).

Anderson and Nafe (1965) presented an analysis of $K_0V_0^x$ relationships, in which the data of quartz, forsterite, basalt, etc. were included. They also derived the relation:

$$V_{0i} \approx \rho^{(x-1)/2}$$

where V_{0i} is the ambient velocity for mode i $(i = 1, 2, 3)$. The velocity is seen as a nearly linear function of density.

5.8.11. Stretch densification

A solid increases in density when stretched along an axis of negative linear compressibility. Materials showing negative compressibilities (when hydrostatically compressed) in one or more dimensions have been discussed by many authors (Baughman et al., 1998). These are shown to have negative Poisson's ratios. (*Note*: Poisson ratio is the ratio of a lateral contraction to a longitudinal elongation produced by a tensile stress.) However, a few crystals with a negative Poisson's ratio show a negative linear compressibility. Plastically deformed foams and honeycombs are known to provide either negative Poisson's ratios or Poisson's ratios whose sums exceed unity about a stretch direction. Some of these crystals decrease in volume and expand in two dimensions when stretched in a particular direction and increase in surface area when hydrostatically compressed. These show the property "stretch-densified". The known stretch-densified phases, such as cesium dihydrogen phosphate and lanthanum niobate, are monoclinic phases but no stretch-densified triclinic phases have been identified.

Stretch densification may be modelled from a wine-rack-like deformation mode (Baughman and Galvao, 1993). Molecular mechanics calculations suggest that ferroelasticity (and associated shape-memory behaviour) should occur in combination with negative linear compressibilities. Negative linear compressibilities may result from various structures comprising helical chains: (i) single helices, (ii) oppositely wound

helices (like the finger cuff) and (iii) the network of left- and right-handed helices. A tensile stress in the helical axis direction decreases the volume (of the finger cuff) and the cylinder-direction angle between the helices becomes $< 109.46°$.

5.8.12. Compressibility and Si–O–Si bending

Shallow Earth materials mainly compress by bond angle bending whereas highly symmetric closest-packed deep Earth materials compress mainly by bond shortening. For example, Si–O–Si angle bending correlates with the compressibility of the SiO_2 polymorphs (Hemley et al., 1994), which all seem to lie on the same $\Delta V - \Delta(\text{Si–O–Si})$ trend (Downs and Palmer, 1994).

The compressibility of an individual silica structure is simply related to the displacements of the $\langle \text{Si–O–Si} \rangle_0$ angles from their global equilibrium value ($\sim 144°$); the further from the equilibrium angle, the stiffer the structure.

In most framework silicates, the principal compression mechanism is T–O–T bond bending (i.e., framework distortion) coupled with the compression of alkali–oxygen and alkaline earth–oxygen bonds. Cation–oxygen-bond compression was shown to be strongly influenced by Coulombic effects, whereby the bond compression becomes inversely proportional to the cation charge. Thus, large monovalent and divalent cation sites, typical of felspars, felspathoids, zeolites and other framework aluminosilicates, display significant compression (Hazen and Finger, 1989). The M-cation affects the bending energy of the T–O–T angle through the charge of the M-cation and the M–O bond length. If the bridging oxygen is bonded to three or more atoms, the energy required for bending the T–O–T angle is significantly increased (Geisinger et al., 1985).

The compression mechanism of the alkali felspars is dominated by the compression of the alkali-containing channels. The compression pathway may result from the T–O–T angle-bending energies that are linked to the alkali cation bonding. The most compressible direction is the one which narrows the channels containing the alkali cations.

A large family of dense structures can be constructed starting with a close-packed (or nearly so) array of oxygen atoms. Distinct structures are obtained depending on the ordering of the Si atoms in the octahedral sties. This produces chains of SiO_6 octahedra with different degrees of kinking. The structure with no kinks is that of stishovite, which has the $CaCl_2$-type structure.

5.8.12.1. Ionic compressibilities

From the ionic radii in a crystal structure, ionic radius vs. bond strength systematics have been developed. If the bond strength is defined as Z/N, where Z is the valence of the cation and N is the coordination number, the ionic radii for Si, Al, Mg, Cr, Fe and Ca given by Shannon and Prewitt (1969) can be shown to be a linear function of the log of the bond strength, thereby satisfying equations of the form:

$$R = ab \log(Z/N),$$

a and b are the fitted constants and R is the Shannon and Prewitt radius. Knowledge of a few ionic-radius values for a particular atom in a polyhedra allows one to predict

accurately the ionic radius for any other combination of valence and coordination number, provided all the ions have the same spin state.

Empirical relations between the volumes of coordination polyhedra and the ionic compressibilities have been proposed by many workers and have been used with considerable success in predicting crystal structures at high pressures. However, Hazen and Finger (1979) found that the relations are less dependent on structure types. Moreover, the observed bond compressibilities, β, can be modelled by an equation of the form:

$$\beta = 0.217\, b^2,$$

where the constant b is derived from linear regression and is the slope of the ionic radius–log bond strength curve for that type of ion. Since this equation is independent of the structure type and includes information about the coordination number, it provides a general means for estimating the ionic compressibility of various coordination polyhedra. The values are calculated from the relationship of Hazen and Prewitt (1977) and the observed values. The agreement obtained is remarkably good (Kudoh et al., 1992).

5.9. Free and thermal energies: phase boundaries

Thermodynamic parameters are used to verify the consistency of phase-equilibrium data and also to extrapolate the phase boundaries beyond the limited $P-T$ space of the experiments (e.g., Chopelas et al., 1994a). Estimates of the phase boundaries using the thermodynamic parameters complement phase-boundary measurements at high P and T. Delineation of phase boundaries helps to model the mantle compositions and temperatures at the seismic discontinuities.

The thermodynamic parameters which are mostly employed for estimating phase boundaries are the following:

ΔH : change in enthalpy
ΔS : change in entropy
C_{P} : heat capacity
ΔV : change in volume across the phase transition.

Enthalpies are measured by calorimetry (e.g., Akaogi and Ito, 1993). Entropies and heat capacity are derived from spectroscopic measurements using statistical thermodynamics. Volumes are derived from compression measurements at room temperature and thermal-expansivity systematics (e.g., Chopelas and Boehler, 1992b), i.e., from elastic constants, EOS and thermal expansivity. Changes in ΔS for transitions by P and T changes can be evaluated by using vibrational models. This has been done for several materials (e.g., Chopelas et al., 1994; Chopelas, 1996). An interdependence between entropy and volume in a given phase at different $P-T$ conditions can be seen by considering the equation for the entropy of a gas:

$$\Delta S = nR \ln \frac{V_2}{V_1}$$

where n is the number of moles, R is the universal gas constant and 1, 2 represent the two states.

This simple relationship depicts that entropy and volume are not independent variables and this relation remains valid even in the case of a solid (mineral). The changes in ΔS are quite small (of the order of a few %) but are large enough to change the topography of a phase-diagram calculation over long extrapolations.

A phase diagram is the map of the stability domains of the co-existing phase in the $P-T$ plane and the slope of the co-existing boundary of phases is represented by the Clausius–Clapeyron equation:

$$\frac{\Delta P}{\mathrm{d}T} = \frac{\Delta S}{\Delta V}$$

where ΔV and ΔS are the changes in volume and entropy at the transition.

Close examination of the relationship between S and V for the forsterite to β-phase transition (Chopelas, 1991) showed that $\Delta S/\Delta V$ changed by an amount much smaller than the experimental error over a large temperature and pressure range.

At the point of a phase change in bulk matter, the internal energy change ΔU from solid to liquid must exactly balance the contribution of entropy to the total energy change, $T\Delta S$. Only at P and T where these two are equal can solid and liquid co-exist in equilibrium. This is the relation that yields the co-existence curve of the solid–liquid phase diagram. The equality of ΔU and $T\Delta S$ ensures that the solid and liquid forms are equally likely to be found.

5.9.1. Free energy

At high pressures, the atoms organize themselves more efficiently, tending to pack into a higher coordination number. Stable (thermodynamically) phases are those, which manifest minimum energy. The internal energy as a function of crystal volume is related to the free energy and pressure as

$$P = -(\delta A/\delta V)_{\mathrm{T}} = -\mathrm{d}E/\mathrm{d}T, \qquad \text{at } T = 0^{\circ}\mathrm{K},$$

where A is the Helmholtz free energy $(A = E - TS)$, E the internal energy and S the entropy.

Gibbs free energy relates the extrinsic variable (P and T) to intrinsic properties (S and V) of a material body. The Gibbs free energy of a pure phase and end members of solid solution at $P-T$ conditions equal

$$G(P,T) = H^0_{298} + \int_{298}^{T} C_{\mathrm{P}}\mathrm{d}T - T\left(S^0_{298} + \int_{298}^{T} \frac{C_{\mathrm{P}}}{T}\mathrm{d}T\right) + \int_{1}^{p} V\,\mathrm{d}P \tag{5-58.2}$$

where C_{P} is the heat capacity expressed as

$$C_{\mathrm{P}} = a + bT + cT^2 + dT^2 + eT^3 + f\,T^{-0.5} + gT^{-1}$$

The Gibbs free energy for solid solution G^{SS} can be expressed as

$$G^{\mathrm{SS}} = x_1 G_1 + x_2 G_2 + RT(x_1 \ln X_1 + x_2 \ln x_2) + G^{\mathrm{ex}}$$

where $G_{1,2}$ is the Gibbs free energy of solid-solution end members 1 and 2. x_1 is a molar ratio in a phase, $x_2 = 1 - x_1$ and G^{ex} is excess Gibbs free energy of the solid solution described by polynomial (*Redlich–Kister model*):

$$G^{ex} = x_1 x_2 [A_0 + A_1 (x_1 - x_2)]$$

where A_0 and A_1 are the pressure- and temperature-dependent parameters.

5.9.1.1. Free energy change and phase boundary

At the phase boundary, there is no change in the free energy ($\Delta G = 0$) and the locus of the phase boundary can be written as

$$P = \left(\frac{\Delta S}{\Delta V} \right) T - \frac{\Delta H}{\Delta V}. \tag{5-59}$$

Setting the Gibbs free energy change, ΔG, to zero, the following equation is employed for the determination of phase boundaries:

$$\Delta G^0_{P,T} = 0 = \Delta H^0_{P,T} - T \Delta S^0_{P,T} + \int_0^P \Delta V \, dP \tag{5-60}$$

where ΔH is the enthalpy of transition, T is temperature, ΔV is the volume change across the phase boundary and P *is* the pressure. The other symbols carry their usual meaning.

Further, if one assumes that the molar-volume change (ΔV) is not a strong function of pressure, then equation can be further simplified to

$$\Delta G = \Delta H - T \Delta S + P \Delta V.$$

The entropy ΔS in phase-boundary calculations can be estimated by selecting one point along a measured phase boundary, solving for entropy using the equation and then calculating the remaining phase boundary using this value. Absurd values are obtained if the chosen point does not fall on the phase boundary. However, vibrational spectroscopic data and statistical thermodynamics allow entropy to be determined independently.

The general condition for equilibrium is expressed as

$$RT \ln K + \Delta G_{T,P} = 0$$

where K is a ratio of products of the activities of products and reactants and the Gibbs free energy change, $\Delta G_{T,P}$, is approximated by the following expression (e.g., Gasparik, 1994):

$$\Delta G_{T,P} = \Delta H^0_T - T \Delta S^0_T - C T^{1/2} + (\Delta V^0_T - bP) P \tag{5-61}$$

In the above expression, C is a parameter capable of expressing the heat-capacity differences, particularly those arising from disorder, and b can express the difference in compressibilities. The parameters can be used only in those cases where the differences in the heat capacities or compressibilities significantly affect the phase relations and could not be omitted. The effects on the phase relations arising from differences in thermal expansions are found to be less significant and thus not necessary to include.

The free-energy change ΔG determines the chemical equilibria (relating reactants and products):

$$\Delta G = RT \ln(a_m a_n \cdots / a_x a_y \cdots).$$

For most mineral reactions, ΔG ranges ~ 50 kcal (200 kJ) each side of zero.

Under pressure, a change in volume of 1 cm^3 corresponds to a change in energy of 10 kcal (40 kJ). This small volume change can bring about a large shift in chemical equilibria. Phase equilibria are shifted by pressure when inter-atomic bonds are broken and reformed.

5.9.1.2. Volume change and ΔH

The thermodynamic relationship that exists between pressure (P), temperature (T), volume change (ΔV) and heat absorbed in melting (ΔH) is

$$dT/dP = T\Delta V/\Delta H.$$

High-density forms are, in general, favoured at high pressure. Since ΔH can be positive or negative, the effects of pressure and temperature may reinforce or oppose stabilization of the high-pressure phase. It is seen that the melting points of iron increase by about 100°C (212°F) under pressure of 5–10 GPa. At 1 bar (10^5 Pa), NaCl melts in an iron crucible but, at 10 GPa pressure, iron can be melted in an NaCl crucible. This is because the ΔH for the melting of iron is very small compared with the ΔH for melting of NaCl.

5.9.1.3. Activation volume and activation enthalpy

When the activation volume (V^*) is considered equal to the formation volume of a vacancy, and the vacancy is considered as a cavity in a solid under pressure, the semi-empirical model of O'Connell (1977) can be used, wherein

$$V^* = V_0^*(1 + PK_0'/K_0)^{-1/K_0'}$$

where V^* is the activation volume at pressure P, V_0^* is the activation volume at zero pressure and K_0' is the pressure derivative of K_0. K_0' is defined as 4/9 of the bulk modulus (K) of the matrix.

At low pressure (e.g., 1 GPa), the normal stress at the inter-phase boundary will be low and could even be tensile owing to the volume change of transformation. At higher pressure (e.g., 15 GPa), there will be a high compressive stress normal to the boundary. Changes in the structure of the inter-phase boundary arising from differential stress can result in changes in the activation volume. Because there are no estimates of V^* (or its pressure dependence) for diffusion across inter-phase boundaries in minerals, Rubie and Ross (1994) used an empirical model (O'Connell, 1977) with V^* decreasing from 12 $cm^3\ mol^{-1}$ at 1 bar to about 4 $cm^3\ mol^{-1}$ at 15 GPa (Kirby et al., 1996).

The relationship between the Gibbs free energies for the perovskite and enstatite phase (Mg, Fe)SiO_3 at low and high pressure are schematically shown in Fig. 5.13 as a function of the configurational coordinate describing the phase transformation.

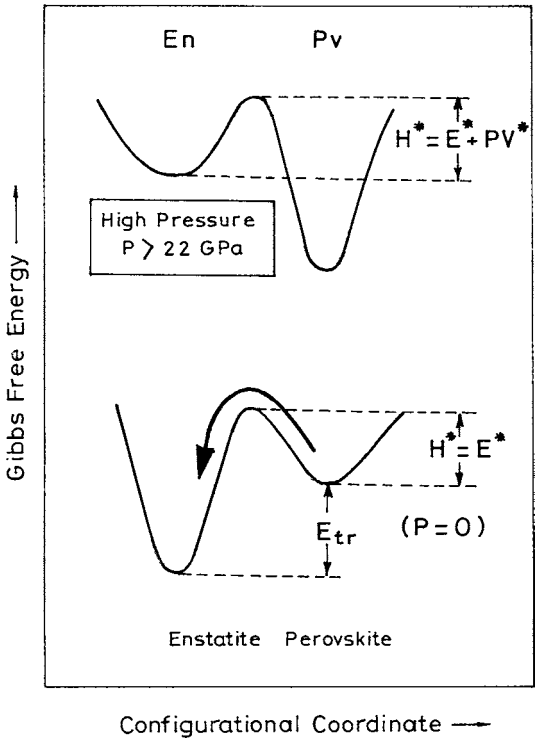

Figure 5.13. The relationship between the Gibbs free energies for the perovskite and enstatite phase of (Mg, Fe)SiO_3 at low and high pressure are schematically illustrated as a function of the configurational coordinate describing the phase transformation. It is assumed the value of E^*, the activation energy, is equivalent at low and high pressure. The energy of transformation at zero pressure, E_{tr} is shown for comparison (Knittle and Jeanloz, 1987a, © 1887 AAAS).

It is assumed that the value of E^*, the activation energy, is equivalent at low and high pressure. The energy of transformation at zero pressure, E_{tr}, is shown for comparison.

For silicate perovskite, the activation enthalpy ($H^* = E^* + PV^*$) is plotted in Fig. 5.14 as a function of pressure (assuming that the activation volume varies between 1 and 30 $cm^3\ mol^{-1}$). The top scale indicates the depth of the Earth that corresponds to the pressure given on the bottom scale. The extrapolated values of H^* for perovskite are compared with a range of values found for olivine. At 670 km depth, if V^* for perovskite is small ($1-10\ cm^3$ mol), then H^* is still small (≤ 300 kJ/mol) at comparable pressures. Fig. 5.14 illustrates the importance of determining V^* in order to determine H^* for minerals deep in the Earth (Knittle and Jeanloz, 1989)

5.9.1.4. Communal entropy: fluid

Kirkwood (1950) introduced the concept of communal entropy ($\Delta_{com}S_{TV}$), which represents the additional entropy a model fluid acquires when its molecules are free to move around the whole available volume, compared with a crystal or glassy state in which

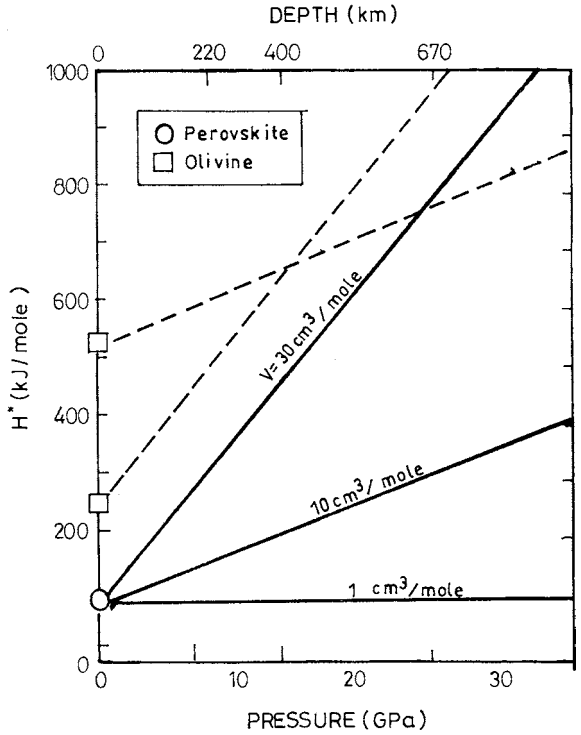

Figure 5.14. The activation enthalpy ($H^* = E^* + PV^*$) as a function of pressure for silicate perovskite. The activation volume is assumed to vary between 1 and 30 $cm^3\ mol^{-1}$. The top scale indicates the depth in the Earth corresponding to the pressure shown on the bottom scale. The extrapolated values of H^* for perovskite are compared with a range of values found for olivine. If V^* for perovskite is small (1–10 cm^3 mole), then at 670 km depth, H^* is still small ($\leq$300 kJ/mol) in comparison with a representative silicate such as olivine at comparable pressures (Knittle and Jeanloz, 1987, © 1987 American Geophysical Union).

the molecules are naturally constrained. An alternative communal entropy can similarly be defined as the entropy difference between the single-occupancy (SO)-cell model and the free fluid at the same temperature and pressure ($\Delta_{\text{com}}S_{\text{TP}}$). These two communal entropies are related as

$$\Delta_{\text{com}}S_{\text{TV}} = \Delta_{\text{com}}S_{\text{TP}} + R \ln PV/RT \tag{5-62}$$

At constant T and vanishing P, the Gibbs free-energy difference between the SO-cell model and the free fluid is exactly RT. The SO-cell model undergoes phase transition at pressure P^*, up to which the EOS is given by

$$P^*_{\text{SO}} = [1 + \pi\sqrt{2}(V_0/V)^{4/3} + (\pi\sqrt{2})^2((V_0/V)^3 + (V_0/V)^6)]/V^* \tag{5-63}$$

where P^*_{SO} is a measure of the reduced pressure in hard-sphere units of kT/σ^3 (where k is Boltzmann's constant), V^* is the reduced volume in units of $N\sigma^3$ and V_0 is the minimum volume at close packing.

For a thermodynamic hard sphere (fluid), the pressure, at a fixed temperature and volume, is directly related to the collision frequency as

$$P^* = (1 + n_C(z)\sqrt{\pi}/3\tau)/V^*,$$

where n_C is the number of collisions in time, τ. Only first neighbours collide in the stable crystal region.

5.9.1.5. Heat capacity, entropy and phase boundaries

To explain the T-dependence of the heat capacity of solids, Einstein (1907) proposed the quantization of vibrational energy (as a single characteristic frequency). He unified the nascent theory of radiation quanta (of Planck) with the thermodynamics of solids in his groundbreaking paper "Planck's theory of radiation and the theory of specific heat" (Einstein, 1907). Here, he demonstrated that if the atomic vibrations are quantized (in accordance with Planck's nascent theory) then the heat capacity of a solid will be temperature dependent rather than be a constant, as given by the Dulong–Petit law of classical thermodynamics. Taking clues from heat capacities, Einstein plotted the heat capacity of diamond as a function of temperature to show that atomic vibrations in solids are quantized. In Einstein's picture, the heat capacity increases monotonically from zero with increasing temperature (Fig. 5.15). The temperature (x-axis) is scaled to the Einstein temperature $qE = 1{,}320$ K. The heat capacity (y-axis) is given in cal mol^{-1} K^{-1}). Debye generalized the quantization rules to include all lattice vibrations (like standing waves). In the modified form, the heat capacity in simple systems increases as a power of the temperature. The powers correspond to the dimensions involved, viz. for 3D systems the power is 3 and for 2D and 1D systems the powers are 2 and 1, respectively.

The heat-capacity measurement provides information on the quantized nature of vibrational structure. The constant volume heat capacity, C_V, can be estimated from the

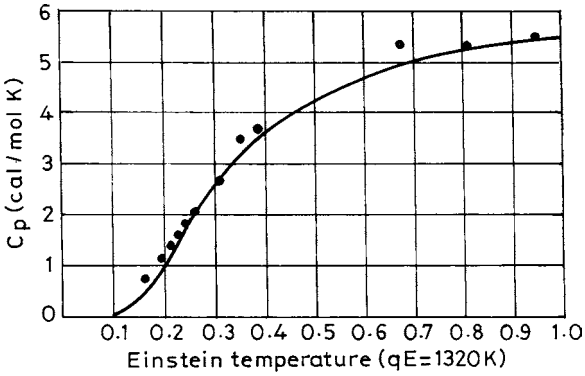

Figure 5.15. Heat capacity of diamond vs. Einstein temperature (Einstein, 1907).

relations

$$C_V = 3Nk \int_0^{\alpha} \frac{e^x}{(e^x - 1)^2} x^2 g(\nu) d\nu \tag{5-64}$$

where N is the number of atoms in the unit cell, k is the Boltzmann constant, ν is the frequency of vibration, x is $h\nu/kT$, h is Planck's constant and $g(\nu)$ is the DOS (vibrational model).

The thermodynamic properties and EOS parameters for phases stable at $P-T$ conditions of the mantle are presented by Saxena and Shen (1992), and Saxena et al. (1993). For these, the phase-equilibria data, calorimetric measurements and relationship between C_P, C_V, thermal expansion α, and compressibility β are taken into account. (*Note*: $C_P = C_V + \alpha^2 VT/\beta$.)

The constant volume heat capacity, C_V, can be converted to the constant pressure heat capacity, C_P, using

$$C_P = C_V + TV\alpha^2 K_T \tag{5-65}$$

where α is the thermal expansivity and K_T is the isothermal bulk modulus. To obtain entropy, the following is integrated over temperature

$$dS = \int_0^{T_1} \frac{C_P}{T} dT \tag{5-66}$$

where T is the temperature under study.

Variations of ΔH with temperature can be estimated using the heat capacity obtained from equation (5-65) in

$$\Delta H^0(T) = \Delta H^0(T_0) + \int_{T_0}^{T} \Delta C_P \, dT \tag{5-67}$$

Changes in volumes can be estimated by first using the bulk modulus and its pressure dependence in the third-order EOS (Birch, 1978). The volumes are then corrected for temperature with 1-atm thermal expansivity systematics (e.g., Chopelas and Boehler, 1992). This method circumvents the need to compress the materials at high temperatures where the bulk moduli are poorly known.

At the point of a phase change in bulk matter, the internal energy change, ΔU, from solid to liquid must exactly balance the contribution of entropy to the total energy change, $T\Delta S$. Only at P and T where these two are equal can solid and liquid co-exist in equilibrium. This is the relation that yields the co-existence curve of the solid–liquid phase diagram. The equality of ΔU and $T\Delta S$ ensures that the solid and liquid forms are equally likely to be found.

Heat capacity cannot be measured by performing calorimetry at pressure. This problem can be circumvented by measuring the vibrational spectra of minerals at mantle pressures and by utilizing these data to calculate heat capacity and entropy as a function of both temperature and pressure (e.g., Kieffler, 1980, 1982). The mode-Grüneisen

parameters (γ_i) obtained from the same experiments permit direct calculation of γ_{th} as a function of pressure.

Kieffer's (1979) lattice dynamics model accurately reproduces heat capacity C_V and entropy S at 1 atm for forsterite (Akaogi et al., 1984) and fayalite (Hofmeister, 1987). The pressure dependence of the other properties is computed when $C_V(P)$ are known or can be calculated.

Employing the heat capacity (C_P), thermal expansion (α) and density of solids and melts (ρ), an adiabatic P–T trajectory can be calculated from the relation:

$$(dT/dP)_S = \frac{\alpha T}{\rho C_P} \tag{5-68}$$

The geotherms corresponding to MORB adiabats have been determined as 1,300°C (Nisbet et al., 1993). This adiabat intersects the olivine–β-phase transition at 1,395°C and 13.7 GPa (410 km). In this transition, the reaction is exothermic, while the γ-spinel to perovskite + Mg-wüstite phase transition is an endothermic reaction and a temperature decrease should occur across 660 km. However, the phase boundaries representing equilibrium reactions should run in either direction (up for low pressure or down for high pressure) with the perturbing P and T; and the sign (positive or negative) of the changes in enthalpy and entropy should change accordingly. This also signifies that the olivine to β-phase transition is exothermic and the transformation of γ-spinel to perovskite + Mg-wüstite is endothermic.

5.9.2. Thermal-expansion coefficient

The effect of pressure on the thermal-expansion coefficient is determined (Birch, 1952) by the relation:

$$\alpha = \alpha_0 \left(\frac{V}{V_0} \right)^{\delta_T}$$

where δ_T ($\equiv q$) is the second Grüneisen parameter, which is assumed to be independent of temperature and pressure above Debye temperature (e.g., Anderson et al., 1991). α_0 and V_0 are the thermal-expansion coefficient and molar volume at some reference state. The thermal-expansion coefficient at higher temperatures and pressures is calculated using the above equation along an isothermal. The volume dependence of thermal expansion in the case of alkali halides has been expressed as (Yagi, 1978):

$$\alpha/\alpha_0 = (V/V_0)^{\delta_0}$$

where $\delta_0 = -(1/\alpha K)(dK/dT)_P$. From static P–V–T measurement, δ_0 is directly measured and a systematic difference of δ_0 is observed between alkali halides with NaCl structure ($\delta_0 = 2$–3) and those with CsCl structure ($\delta_0 = 6$ to ~ 7). The volume

relation is expressed as

$$V = V_0 \exp\left(\int_{T_0}^{T} \alpha(T)\mathrm{d}T\right) \tag{5-69}$$

This relation is corroborated by the experiments conducted by Fei et al. (1992) on $(Mg_{0.6}Fe_{0.4})O$ magnesiowüstite in the range of $T = 1{,}100-2{,}000$ K and P reaching up to 30 GPa.

Temperature increases the volume while pressure decreases it. The relations are defined by the thermal expansion coefficient, α, and the bulk modulus:

$$\alpha = \frac{1}{V}\cdot\frac{\delta V}{\delta T} \qquad \text{or} \qquad \frac{1}{K} = \frac{1}{V}\cdot\frac{\delta V}{\delta P}. \tag{5-70}$$

The variation of frequency with pressure provides a basis for estimating entropy vs. pressure, which directly yields thermal expansivity through the *Maxwell equation*:

$$\left(\frac{\delta V}{T}\right)_{\mathrm{P}} = -\left(\frac{\delta S}{\delta P}\right)_{\mathrm{T}} \tag{5-71}$$

and the thermal expansivity is then

$$\alpha = \frac{1}{V}\left(\frac{\delta V}{\delta T}\right)_{\mathrm{P}}$$

To calculate α from the variation of entropy vs. pressure, the molar volume of the phase must be known at the pressure and temperature of interest. At higher pressures, the bulk moduli (K_0) and their pressure derivative (K_0') for each of the phases are used to calculate the volumes at various pressures. Any uncertainty in volume determination does not significantly contribute to uncertainty of expansivity. An accurate computation of the entropy is more important than the volume.

The thermal expansivity is generally inversely proportional to the bulk modulus (K_0). This is because γ_{th} and V/C_{V} vary little among the minerals. It is reasonable that a very incompressible mineral such as stishovite will have the lowest α-values whereas the more compressible ones (e.g., orthoenstatite) will have one of the highest α-values at RT (*see* Table 5.5).

5.9.2.1. α values: spectroscopic vs. volumetric

Since the vibrational mode frequencies of crystals depend solely on the variation of volume, the volume thermal expansivity (α), isothermal bulk modulus (K_{T}) and the pressure and temperature dependences of frequency ν_i of a vibrational mode are related by

$$\alpha K_{\mathrm{T}} = -(\delta\bar{\nu}_i/\delta T)_{\mathrm{P}}/(\delta\bar{\nu}_i/\delta P)_{\mathrm{T}} \tag{5-72}$$

The value of $(\delta\bar{\nu}_i/\delta T)_{\mathrm{P}}$ can be reliably measured through experiments, followed by K_{T}, $(\delta\bar{\nu}_i/\delta P)_{\mathrm{P}}$ and α, using the above relationship if the values of the other three quantities are available.

At RT the normal modes or vibrations of a crystal lattice at or below $\sim 300\ \mathrm{cm}^{-1}$ are predominantly active in the crystal. This can be seen in the anti-Stokes spectrum where the modes above $300\ \mathrm{cm}^{-1}$ have almost no intensity. As temperature is increased, the intensity of the higher energy modes increase in the anti-Stokes spectrum since more bonds (modes) become active in the expansion.

At high temperatures, the exact value of α is underestimated. When the higher energy vibrations become active, the pressure shifts of these modes will increase. However, the high-energy modes of the high-pressure polymorphs are inter-coupled and thus are not separable into independent contributions from various polyhedral units (e.g., MgO_6 octahedra and SiO_4 tetrahedra).

Using the thermodynamic Maxwell relation (equation (5-71))

$$(\delta S/\delta P)_{\mathrm{T}} = -(\delta V/\delta T)_{\mathrm{P}}$$

the values of thermal expansities (α) can be determined. In this case, the entropies at high pressures are derived using a statistical method and spectroscopic data.

The spectroscopically determined thermal expansivities of minerals correspond very well with those derived from volumetric data. The results of some minerals are tabulated in Table 5.6 (Chopelas, 2000).

TABLE 5.6

Comparison of spectroscopically determined thermal expansivity α with those derived from volume measurements (*Source*: Chopelas, 2000)

Mineral	Spectroscopic ($10^{-5}\ \mathrm{K}^{-1}$)	Volumetric ($10^{-5}\ \mathrm{K}^{-1}$)
Forsterite	2.40[a]	2.72[b]
β-Mg_2SiO_4	1.89[a]	2.01[c]
γ-Mg_2SiO_4	1.84[a]	1.68[d]
MgO	2.79[a]	3.11[e]
Stishovite	1.33(8)′	14.2 [g]
$MgSiO_3$, Orthoen.	3.25(10)′	2.2–4.77 [h]
$MgSiO_3$, High Clen.	2.59(10)′	Not measured
$MgSiO_3$, Majorite	2.24(9)′	2.36
$MgSiO_3$, Ilmenite	1.7(1)′	–
$MgSiO_3$, Perovskite	1.8(1)[a]	1.72[i]

[a]Chopelas (1996).
[b]Kajioshi (1986).
[c]Suzuki et al. (1980).
[d]Suzuki et al. (1979).
[e]Isaak et al. (1989).
[f]Chopelas (2000).
[g]Fei et al. (1990), Ito et al. (1974a) and Ito et al. (1974b).
[h]*See* Chopelas (2000).
[i]Funamori et al. (1993), Utsumi et al. (1995), Wang et al. (1994).

5.9.3. Grüneisen parameter (γ)

The Grüneisen parameter (γ) is used for assigning constraints on geophysically important parameters such as the P, T dependence of the thermal properties of the mantle and core, the adiabatic temperature gradient and the geophysical interpretation of Hugoniot data.

5.9.3.1. Mode Grüneisen (M-G) parameter

The first mode Grüneisen parameter is calculated as

$$\gamma_i = -\left(\frac{\delta \ln \nu_i}{\delta \ln V}\right) \tag{5-73}$$

where ν_i is the frequency of the ith vibrational mode and V is the corresponding unit-cell volume. This is equivalent either to $\gamma_i(V) = -(V/\nu_i)(\mathrm{d}\nu_i/\mathrm{d}V)$ or to $\gamma_i(P) = (K_\mathrm{T}/\nu_i)(\mathrm{d}\nu_i/\mathrm{d}P)$.

Calculation of the first- and second-mode Grüneisen parameters, γ_i and q_i, from frequency and pressure determinations is analogous to deriving bulk modulus K_T solely from volume and pressure measurements.

The second Grüneisen parameter is calculated from

$$q_i = \mathrm{d} \ln \nu_i / \mathrm{d} \ln V$$

Equivalently,

$$q_i = (V/\gamma_i)(\mathrm{d}\gamma_i/\mathrm{d}V) = 1 + \gamma_i - (V^2/\gamma_i \nu_i)(\mathrm{d}^2 \nu_i/\mathrm{d}V^2)$$

$$q_i = (K_\mathrm{T}/\gamma_i)(\mathrm{d}\gamma_i/\mathrm{d}P) = \gamma^i - K'(K_\mathrm{T}^2/\gamma_i \nu_i)(\mathrm{d}^2 \nu_i/\mathrm{d}P^2).$$

5.9.3.2. Thermal Grüneisen parameter (γ_{th})

The thermal Grüneisen parameter (γ_{th}) has been discussed in the following in relation to the spectroscopic M-G parameter. If γ_i for the mode represents all the vibrations of the crystal (Gillet et al., 1998), then one can write

$$\gamma_i \sim \gamma_{th} = \gamma_0 (V/V_0)^q$$

where γ_0 represents the extrapolated value of γ_{th} at zero pressure with the volume dependence of γ_{th} explicitly given by parameter q.

The Grüneisen thermodynamic parameter is calculated as

$$\gamma_{th} = \frac{\alpha K_{0\mathrm{T}} V_0}{C\mathrm{V}} \tag{5-74}$$

where α is the 1-atm thermal expansion coefficient, $K_{0\mathrm{T}}$ is the isothermal bulk modulus at 1 atm, V_0 is the molar volume at 1 atm and C_V is the molar-heat capacity at constant volume ($C_\mathrm{V} = C_\mathrm{P} - \alpha^2 K_{0\mathrm{T}} V_{0\mathrm{T}}$). The specific heat at constant pressure (C_P) is related to the thermal-expansion coefficient (α) and bulk modulus as $C_\mathrm{P} = C_\mathrm{v} + \alpha^2 K_{0\mathrm{T}}$.

This parameter is of significant interest to geoscientists because it determines the limitations on the thermoelastic properties of the lower mantle and core. It is directly related to the EOS.

The spectroscopically derived weighted average Grüneisen parameter is $\langle\gamma\rangle = \sum C_i\gamma_i/C_i$, where C_i is the Einstein heat capacity of mode i and γ_i is the Grüneisen parameter of mode i. A comparison of the weighted average of the spectroscopic Grüneisen parameters $\langle\gamma\rangle = \sum C_i\gamma_i/C_i)$ with the thermal Grüneisen parameter $\gamma_{th} = (\alpha K_T V/C_V)$ is presented in Table 5.7 (Chopelas, 2000). Discrepancies between $\langle\gamma\rangle$ and γ_{th} have been observed in all minerals studied and $\langle\gamma\rangle$ is always 10–15% lower than γ_{th}, suggesting that many materials cannot be well described as Debye solids. The dependence of γ_{th} on Fe content in olivine series is discussed in Section 6.5.2 (*see* Fig. 6.30).

In the vibrational spectrum of silicate minerals, all the high-energy modes are associated with the very incompressible SiO_4 tetrahedra and have very low mode γ_{th} values.

5.9.3.3. Density and Grüneisen parameter

The density (ρ) and the Grüneissen parameter (γ) are related as

$$(\gamma/\gamma_0) = (\rho/\rho_0)^{-q}$$

where q is an arbitrary constant (Anderson, 1968). The EOS along the solidus is obtained when ρ is determined from P. To obtain $\rho(P)$, the bulk modulus–pressure curve $K(P)$ is used. An empirical $K(P)$ is obtained from the shock-wave Hugoniot.

TABLE 5.7

Comparison of the weighted average of the spectroscopic Grüneisen parameters $\langle\gamma\rangle$ $(= \sum C_i\gamma_i/C_i)$ with the thermal Grüneisen parameter γ_{th} $(= \alpha K_T V/C_V)$ (*Source*: Chopelas, 2000)

Mineral	$\langle\gamma\rangle$	γ_{th}
Forsterite	1.19[a]	1.29
β-Mg_2SiO_4	1.29[b]	1.39
γ-Mg_2SiO_4	1.10[c]	1.25
MgO	1.47[d]	1.52
Stishovite	1.40[e]	1.34
$MgSiO_3$ Orthoenstatite	1.20[e]	1.28
$MgSiO_3$ High Clinoen	1.09[e]	1.22[f]
$MgSiO_3$ Majorite	1.32[e]	1.28[f]
$MgSiO_3$ Ilmenite	1.24[e]	1.22[f]
$MgSiO_3$ Perovskite	1.43[d]	1.42

Parameters for all minerals for calculation of γ_{th} are available in Chopelas (2000).
[a]Chopelas (1990).
[b]Chopelas (1991).
[c]Chopelas et al. (1994).
[d]Chopelas (1996).
[e]Chopelas (2000).
[f]Using α at room T determined by Chopelas (2000).

5.9.3.4. Debye model

Using Einstein and Debye approximations, the Grüneisen parameter in the Debye model, γ_D, bears the relation:

$$\gamma_D = -\mathrm{d}\ln \Theta_D / \mathrm{d}\ln V,$$

where Θ_D is an effective Debye temperature (equivalent to the Einstein temperature, Θ_E, by the relation $\Theta_D = 5/3\Theta_E$ for $T > \Theta_D$).

Spectroscopic data and theoretical predictions on silicate perovskite indicate that γ_{th} of Mg-silicate perovskite is 1.7–2.0 (Hemley, 1991), while Θ_D values range from 725 to 1,200 K (Stixrude and Bukowinski, 1990). However, the vibrational DOS is not well represented by a Debye model.

5.9.3.5. Anderson–Grüneisen parameter

The variation of α with pressure is characterized by the Anderson–Grüneisen parameter $\gamma_{T,S}$, which is defined as

$$\gamma_{TS} = -\frac{1}{\alpha K_T}\left(\frac{\mathrm{d}K_T}{\mathrm{d}T}\right)_P \tag{5-75}$$

which is nearly constant at Earth's internal temperature conditions. When $\gamma_{T,S}$ is independent of P and T, it equals $(\mathrm{d}\ln \alpha/\mathrm{d}\ln V)_P$.

Intregation of first and second Grüneisen parameters with respect to temperature at constant volume would lead to the *Mie–Grüneisen expression* for γ:

$$\gamma = \frac{P_{th}V}{E_{th}} \tag{5-76}$$

(P_{th} = thermal pressure and E_{th} = thermal energy).

In principle, P_{th} and E_{th} can be calculated from ab initio free-energy calculations (e.g., Vocaldo et al., 1999, 2000).

In the Mie–Grüneisen approach, the total pressure, $P_{tot}(V,T)$, can be expressed as a sum of the static pressure, P_{st}, i.e., isothermal compression at 300 K and the thermal pressure increases along an isochore, ΔP_{th}:

$$P_{tot}(V,T) = P_{st}(V) + \Delta P_{th}(V,T).$$

Empirical EOS for both (Mg,Fe)SiO_3 and (Mg,Fe)O, based on an anharmonic Einstein model, were developed by Jeanloz and Knittle (1989). These enable one to predict the densities of both the phases under lower-mantle pressures and temperatures. Above the Debye temperature, a decrease in γ_T is expected (Anderson et al., 1990) and hence the measurements need to be extended to higher temperatures (e.g., $>$900 K).

5.9.3.6. Vinet equation

The Vinet equation (Vinet et al., 1987) is derived from a scaled approximate form for the energy:

$$E(r) = -\Delta E(1 + a^*)\exp[-a^*]$$

where

$$a^* = \frac{r - r_0}{l},$$

and ΔE is the binding energy, and r is the length per electron. This gives

$$P(x) = 3K_{T0}(1-x)x^{-2}\exp[3/2(K'_{T0}-1)(1-x)]$$

where $x = (V/V_0)^{1/3}$. The energy can be expressed as

$$E = E_0 + \frac{4K_{T0}V_0}{(K'_{T0}-1)^2} - 2V_0KT_{T0}(K'_{T0}-1)^{-2}$$

$$[5 + 3K'_{T0}(x-1) - 3x]\exp[-3/2(K'_{T0}-1)(x-1)]$$

Vinet EOS works surprisingly well for a wide range of types of materials and for compressions of up to $\eta = 0.1$.

5.9.3.7. Holzapfel equation

The Holzapfel EOS (Holzapfel, 1996) is similarly given by

$$P(x) = 3K'_{T0}x^{-5}(1-x)\exp[(cx+c_0)(1-x)]$$

where c_0 and c are chosen to give K' and the limiting Fermi gas behaviour as $x \rightarrow 0$. If $c = 0$, one gets a three-parameter (V_0, K_{T0}, and K'_0) EOS that behaves better at extreme compression (Hama and Suito, 1996):

$$P(x) = 3K_{T0}x^{-5}(1-x)\exp[c_0(1-x)] = 3K_{T0}x^5(1-x)\exp\left[\frac{3}{2}(K_{T0}-3)(1-x)\right]$$

5.9.3.8. Logarithmic equation

The logarithmic equation EOS (Poirer and Tarantola, 1998) give at third order:

$$P = K_{T0}\left[\ln\frac{V_0}{V} + \left(\frac{K'_{T0}-2}{2}\right)\left(\ln\frac{V_0}{V}\right)^2\right]$$

For extremely compressible matter, e.g., hydrogen, the Vinet EOS is more accurate than the Birch equation. For most of the fits, the V_0 is fixed at a known value of $23.0\ \mathrm{cm^3\ mol^{-1}}$ (Silvera, 1980). The best fit given by the Vinet EOS corresponds well with the fits using Birch or Holzapfel but the logarithmic EOS fails completely (Cohen et al., 2000).

5.9.3.9. Microscopic and macroscopic

For assessing the microscopic origin of thermodynamic properties such as thermal expansivity and entropy, the M-G parameter γ_i (obtained from least square fits of the high-pressure mid-infrared and Raman data; Chopelas and Boehler, 1992) is important. The

value of γ_{0i} (value at zero pressure) is comparatively large, i.e., it has an anharmonicity at low pressure.

The M-G parameter relates the pressure and volume derivatives of the frequency of interest. In most cases, the frequency of the far-IR bands depends linearly on volume and the frequency of mid-IR bands can be related to either volume or pressure.

The γ varies as a function of pressure and volume (e.g., Poirier, 1991) as

$$\gamma = -\frac{V}{2}\left(\frac{\dfrac{\delta^2(PV^{2x/3})}{\delta V^2}}{\dfrac{\delta(PV^{2x/3})}{\delta V}}\right) + \frac{(x-2)}{3} \tag{5-77}$$

Thus, γ behaves differently with different values of parameter x and the Grüneisen parameter is a direct function of the chosen EOS, which defines P as a function of V.

In the absence of reliable high-P, high-T experimental data, thermoelastic parameters, such as the Grüneisen parameter, cannot be reliably obtained from approximate descriptions. Rather, they can be derived from rigorous, highly accurate, quantum-mechanical free-energy calculations.

5.9.4. Thermal expansion and crystal-field changes

Temperature has a 2-fold influence on a crystal structure. Increased thermal motions cause increased amplitude of atoms vibrating about their crystallographic positions and thermal increase in inter-atomic distances causes a decrease in the value of crystal-field splitting, Δ, at elevated temperature. From these considerations, the relationship between the crystal-field shifting and the thermal expansivity is known to be

$$\frac{\Delta_T}{\Delta_0} = \left(\frac{\Delta_0}{\Delta_T}\right)^{5/3} = [1 + \alpha(T - T_0)]^{-5/3} \tag{5-78}$$

Because of thermal vibration, the absorption bands broaden and, due to the expansion of the M–O distance, the band centres move to slightly longer wavelengths, i.e., are "red-shifted". Thus, high pressures and elevated temperatures show compensatory effects on band maxima of absorption bands in crystal-field spectra. But the cumulative effect of both these causes an intensification of the absorption bands through the effects of increased covalency and increased vibronic coupling.

5.9.5. Radiative-heat transport

Minerals absorbing radiation in the near-IR and visible regions control the radiative-heat transport mechanism in the mantle (Clark, 1957).

The energy transfer of photons through a grey body (i.e., one in which absorption by photons is finite, non-zero and independent of wavelength) is given by (Stacky, 1969)

$$K_{\mathrm{r}} = \frac{16n^2ST^3}{3\alpha} \tag{5-79}$$

where K_{r} is the effective radiative conductivity, n is the mean refractive index, T is temperature, α is the mean absorption coefficient and S is the Stefan's constant. S relates the power E (i.e. the rate of energy emission per unit area) of an ideal black body to absolute

$$\frac{\mathrm{d}E}{\mathrm{d}T} = ST^4 \tag{5-80}$$

temperature, T, as follows.

In octahedrally coordinated Fe^{2+}, the $2t_{2g} \rightarrow 4e_g$ ligand-field transition occurs at near-IR. Absorption of black-body radiation by this transition is believed to retard significantly the radiative heat flow in the upper mantle (Shankland et al., 1974). However, the large increase in the $2t_{2g} \rightarrow 4e_g$ band energy due to an HS $\rightarrow$ LS transition of Fe^{2+} in the lower mantle may make the lower-mantle iron (II) mineralogy much more transparent to black-body radiation and, hence, an increase in the thermal conductivity of the lower mantle.

5.9.6. Thermal pressure: Eularian strain

Thermal pressure can be described by using the Debye model (Jackson and Rigden, 1996), and by employing the following relationship:

$$\Delta P_{\mathrm{th}} = \frac{\gamma(V)}{V}\left[E_{\mathrm{th}}(V,T) - E_{\mathrm{th}}(V,T_0)\right] \tag{5-81}$$

$$E_{\mathrm{th}} = \frac{9nRT}{(\theta/T)^3}\int_0^{\theta/T}\frac{\xi^3\,\mathrm{d}\xi}{\mathrm{e}^{\xi}-1} \tag{5-82}$$

$$\gamma = \gamma_0\left(\frac{V}{V_0}\right)^{\eta} \tag{5-83}$$

$$\theta = \theta_0\exp\left(\frac{\gamma_0 - \gamma(V)}{q}\right) \tag{5-84}$$

In the above relations, E_{th} is the vibrational energy for a given volume and temperature, R is the gas constant, γ is the Grüneisen parameter (q is the volume dependence of the Grüneisen parameter $(q = \mathrm{d}\ln\gamma/\mathrm{d}\ln V)$), which is assumed to be constant, n is the number of atoms per formula unit and θ is the Debye temperature.

The Debye approach (equation (5-84)) provides a description of thermal pressure without the truncation problem that can arise when one uses a polynomial expansion

(Jackson and Rigden, 1996). This enables determination of thermoelastic parameters and their pressure and/or temperature dependence in an internally consistent fashion (Shim and Duffy, 2000).

The pressures and their uncertainties are derived from room-temperature–volume measurements across the sample. Elastic models of samples in the laser-heated diamond cell indicate that the thermal pressure for perovskite at temperature above 1,300 K may be 3–5 GPa.

In materials at high temperatures and low strain, there is a large volume dependence of the thermal pressure (Wolf and Jeanloz, 1985). Birch's (1978) normalized pressure, F, is given as (*see* equation (5-52)):

$$F = P[3f(1+2f)^{5/2}]^{-1}, \tag{5-85}$$

where f is the Eularian strain measured as $f = 1/2[(V_0/V)^{2/3} - 1]$.

5.9.6.1. Thermal pressure as a function of volume

The temperature derivative of the isothermal bulk modulus at constant volume is obtained from the thermodynamic identity:

$$\left(\frac{\delta K_T}{\delta T}\right)_V = \left(\frac{\delta K_T}{\delta T}\right)_P + \left(\frac{\delta K_T}{\delta P}\right)_T \alpha K_T \tag{5-86}$$

A non-zero value of $(\delta K_T/\delta T)_V$ would suggest a volume dependence on thermal pressure. The thermal pressure as a function of volume at a constant temperature is expressed by $(T = 300\ \text{K})$:

$$P_{th} = a + b \ln\left(\frac{V_0}{V}\right), \tag{5-87}$$

where

$$a = \int_{300}^{T} \alpha K_T \, dT$$

and

$$b = \left(\frac{\delta K_T}{\delta T}\right)(T - 300)$$

For an earlier discussion involving EOS, see the second half of Section 5.8.7.3.

5.10. Phase transitions

The kinetics of phase transitions may elucidate the dynamics of the process in the Earth. Phase transformation in minerals defines the fields of their stability as a function of P, T and their intensive variables. At any P, T, the stable phase is one in which the free energy is the lowest. However, transitions do not always occur at thermodynamic

equilibrium pressures since kinetic factors are also involved. For this reason, it is usual to observe that, in an experiment of increasing pressure, a higher pressure than the true equilibrium pressure, P_{eq}, is needed to induce transition. Again, when pressure is decreased, the reverse transition does not occur at P_{eq}, but at a pressure below the equilibrium pressure.

To study electronic and phase transitions, several techniques, e.g., Raman and Brillouin scattering, absorption and luminescence measurements, energy dispersive X-ray diffraction, and conductivity measurements, are employed. The phase transitions observed in minerals include displacive phase transitions, cation-ordering transitions (e.g., Al–Si and Na–K) and orientational order–disorder phase transitions. The different types of phase transitions observed in minerals are given in Table 5.8 (Dove, 1997), which offers tabulated examples of phase transitions in minerals that occur with a change in either temperature or pressure. This was extracted from an electronic search of the Science Citation Index for the years 1981–1996. In some cases, details such as symmetry change may still be unknown or uncertain (marked with a "?"). The transformational behaviour of some materials may be affected by the presence of sample impurities, sample treatment or kinetic factors, which can account for some observed uncertainties (source: Dove, 1997).

Reconstructive phase transitions have been observed in complex silicates such as olivine and pyroxene. The phase-transition behaviour of framework silicate minerals is of considerable interest. The concomitant development of mean-field theories of phase-transition behaviour, microscopic computer modelling and new experimental techniques probing a range of length scales and dynamical phenomena have facilitated a profound re-evaluation of the structural behaviour of complex silicates.

Many common rock-forming aluminosilicates exhibit diverse structural behaviour with changing temperature and pressure such as cation order–disorder processes (e.g., Fe–Mg, Al–Si) and elastic instabilities that lead to displacive phase transitions. The coupling between individual order parameters, often by means of a common lattice strain, can make the overall behaviour very complex. Many transitions involve distortions of the aluminosilicate framework. In the context of phase transition, it should, however, be noted that Al and Ca enter into solution in major ferromagnesian phases and modify the phase relationship. But this role could not yet be described in detail from experimental studies. In the case of non-reconstructive-type phase transition, the results of dynamic and static experiments agree satisfactorily.

5.10.1. Mixed and quasi-stable phases

However, in reconstructive phase transition involving time sufficient enough for atomic diffusion, the scenario becomes different as, for the onset of phase transition, an overriding pressure is required and a *wide mixed phase region* is observed before the high-pressure phase region. This may be illustrated with quartz.

Phase transition in quartz starts around 13 GPa, which is higher than the equilibrium transition pressure to stishovite phase at ~9 GPa, although with no indication of the appearance of the coesite phase. A wide mixed-phase region is observed to persist up

TABLE 5.8

Examples of phase transitions (after Dove, 1997)

Material	T_C or P_C	Change	Comments	Reference
Quartz, SiO_2	848 K	$P6_222 \rightarrow P3_121$	Two-stage displacive phase transition involving an intermediate incommensurate phase	Castex and Madon (1995); Dolino and Vallade (1994)
Cristobalite, SiO_2	530 K, 1.2 GPa	$Fd3m \rightarrow P4_12_12$, $P4_12_12 \rightarrow P2_1$	First-order displacive phase transitions involving zone-boundary instabilities	Dove et al. (1995); Palmer et al. (1994)
Tridymite, SiO_2	748 K, 623 K	$P6_3/mmc \rightarrow P6_322$, $P6_322 \rightarrow C222_1$	A number of displacive phase transitions occur on cooling. The two given here involve zone-centre instabilities	Cellai et al. (1995)
Leucite, $KAlSi_2O_6$	960 K	$Ia3d \rightarrow I4_1/acd$, $I4_1/aCd \rightarrow I41/a$	Two-stage displacive phase transition, the first being a ferroelastic phase transition. Other materials with the leucite structure but different chemical composition can undergo other displacive and order–disorder phase transition	Dove et al. (1995)
Albite, $NaAlSi_3O_6$	1,250 K	$C2/m \rightarrow C\bar{1}$	Ferroelastic phase transition. An Al–Si ordering transition follows at lower temperatures but, because this does not involve a further symmetry change, it does not lead to a distinct transition temperature. Substitution of K^+ for Na^+ suppresses the ferroelastic phase transition and is only weakly dependent on temperature	Xiao et al. (1995b)
Anorthite, $CaAl_2Si_6O_{16}$	560 K	$I\bar{1} \rightarrow P\bar{1}$	Displacive phase transition involving a zone-boundary instability. Substitution of Sr^{2+} for Ca^{2+} allows a ferroelastic phase transition although the ordering transition to an $I2/m$ phase	Daniel et al. (1995); Phillips and Kirkpatrick (1995)
Kalsilite, $KAlSiO_4$			A preliminary study indicates the presence of one or more phase transitions, but details remain sketchy	Capobianco and Carpenter (1989)
Kaliophilite, $KAlSiO_4$	1,000 K	$P6_322 \rightarrow P6_3(?)$	Apparently a zone-centre transition, but details are sketchy	Cellai et al. (1992)

TABLE 5.8 (continued)

Material	T_C or P_C	Change	Comments	Reference
Calcite, $CaCO_3$	1,260 K, 1.5 GPa	$R\bar{3}C \rightarrow R\bar{3}m$, $R\bar{3}c \rightarrow P2_1/c$	Orientational order–disorder phase transition involving the carbonate molecular ions. The ordering involves doubling of the size of the unit cell. An additional phase transition occurs at 2.2 GPa	Dove et al. (1997); Fiquet et al. (1994)
Soda niter, $NaNO_3$	560 K	$R\bar{3}c \rightarrow R\bar{3}m$	Orientational order–disorder phase transition involving the nitrate molecular ions. The ordering involves doubling of the size of the unit cell	Harris et al. (1990)
Akermanite, $Ca_2MgSi_2O_7$, and related melilites	343 K	$P\bar{4}2_1m \rightarrow$ Inc	Incommensurate displacive transition. A possible phase transition to another commensurate phase at low temperature has not yet been identified	Brown et al. (1994); Webb et al. (1992)
Cordierite, $Mg_2Al_4Si_5O_{18}$		$P6/mcc \rightarrow cccm$	Al–Si ordering transition	Redfern et al. (1989a); Thayaparam et al. (1996)
Perovskite	1,384 K, 1,520 K	$Cmcm \rightarrow Pbnm$, $Pm3m(?) \rightarrow CmCm$	Displacive phase transition involving tilt of TiO_6 octahedra, with evidence of phase transition to tetragonal and cubic phases at higher temperatures	Guyot et al. (1993); Redfern (1996)
Titanate, $CaTiSiO_5$	497 K	$C2/c \rightarrow P2_1/a$	Zone-boundary displacive phase transition	Bismayer et al. (1992); Zhang et al. (1995)
Staurolite		$Cmm \rightarrow C2/m$	Al-vacancy ordering transition	Hawthorne et al. (1993)
Colemanite, $CaB_3O_4(OH)_3.H_2O$	270 K	$P2_1/a \rightarrow P2_1$	Ferroelectric phase transition	Gallup and Coleman (1990)
Chlorapatite, $Ca_5(PO_4)_3Cl$	620 K	$P6_3/m \rightarrow P2_1/a$	Ferroelastic phase transition	Bauer and Klee (1993)
Cryolite, Na_3AlF_6	820 K	$Immm \rightarrow P2_1/n$		Spearing et al. (1994); Yang et al. (1993)
Langbeinite, $K_2Cd_2(SO_4)_3$		$P2_13 \rightarrow P2_12_12_1$	Transition temperature depends on composition, with several possible substitutions of the Cd^{2+} cation	Boeriogoates et al. (1990); Percival (1990)
Natrite, (Gregoryite), Na_2CO_3	760 K	$P6_3/mmc \rightarrow C2/m$	Ferroelastic phase transition involving the softening of the C_{44} elastic constant	Harris et al. (1993, 1995, 1996); Swainson et al. (1995)

Ilvaite, $CaFe_2Si_2O_2(OH)$	346 K	$Pnam \rightarrow P2_1/a$	Phase transition driven by ordering of electrons on the Fe sites	Ghazibayat et al. (1992); Ghose et al. (1989)
Sodalites			Sodalites of different composition can undergo displacive phase transitions, Al–Si ordering phase transitions, and phase transitions involving orientational ordering of molecular ions in the large cavity coupled to displacive distortions of the sodalite framework	Depmeier (1988, 1992)
Brucite, $Mg(OH)_2$	6–7 GPa		Possible phase transition involving ordering of the H atom	Catti et al. (1995); Duffy et al. (1989a)
Garnets			Several postulated cation-ordering phase transitions based on different observed ordered structures	Hatch and Griffen (1989)
Gillespite, $BaFeSi_4O_{10}$	1.8 GPa	$P4/ncc \rightarrow P2_12_12$	First-order phase transition, mostly displacive in character but also involving some changes in coordination	Redfern et al. (1993, 1997)
Ferrosilite, $FeSO_4$	1.4–1.8 GPa	$C2/c \rightarrow P2_1/c$	Displacive phase transition. Similar transitions are found in other pyroxenes	Hugh-Jones et al. (1994); Shimobayashi and Kitamura (1991)
Arcanite, K_2SO_4	860 K	$P6_3/mmc \rightarrow Pmcn$	Orientational ordering of SO_4^{2-} anions	Miyake et al. (1981)
Sanmartinite, $ZnWO_4$–scheelite, $CuWO_4$		$P2/c \rightarrow P\bar{1}$	Jahn–Teller phase transition as a function of of composition	Redfern et al., (1995); Schofield et al., (1994)
Chiolite, $Na_5Al_3F_{10}$	150 K	$P4/mnc \rightarrow P2_1/n$	Displacive phase transition	Spearing et al., (1994)
Schultenite, $PbHAsO_4$	313 K	$P2/c \rightarrow Pc$	Ordering of the hydrogen bond	Wilson (1994)

to ~50 GPa. The observed Hugoniot of the high-pressure phase is explained as due to stishovite (*see* Graham, 1973).

Again, a quasi-stable phase with a higher free energy may survive because of kinetic factors. The best-known example for such a case is offered by carbon, for which the stable phase with minimum free energy is graphite and the metastable phase is diamond. Therefore, "diamonds are not for ever", but its change is so slow that it can hardly be perceptible even over a million years!

Similarly, Si, on release of pressure from the metallic state, remains in a metastable state, which has a volume intermediate between that of the normal semiconducting silicon and the high-pressure metallic phase. The energy bands in silicon show the empty metallic conduction band and the filled valence band, formed by hybridization of 3s and 3p electrons.

5.10.2. Lattice disorder

Temperature may affect the transition by introducing disorder into the lattice, which introduces a strong scattering of the conduction electron by the local lattice defects. Upon melting when the disordering is large, the bands become so diffuse as to make the transition from one phase to another continuous rather than discontinuous.

Lattice disorder introduces strong scattering of the conduction electron by local lattice defects. For a given crystal structure and chemical composition, the relative positions of the various electronic bands are determined mainly by the inter-atomic distances. The temperature effect operates only via lattice disorder and excites photons (which are indirect ones), causing blurring of the bands. This blurring is sufficient to destroy the narrow gap existing between the valence and the conduction bands in semiconductors.

5.10.3. Silicon: β-tin → hcp

Computer modelling showed that the simple hexagonal phase of Si would be a high-T superconductor, and this has later been confirmed by experiment (Erskine et al., 1987). Silicon under pressure at 12 GPa shows a transition to β-tin structure, followed by a simple hexagonal phase at 14 GPa. At still higher pressures, transitions to the hexagonal close packed (hcp) and face centred cubic (fcc) take place.

5.10.4. Cation distribution and order–disorder

The transitions are structural phase transitions or isostructural transitions where the valence state of the atom or the nature of the spin density wave state changes with pressure. A crossing of crystal-field levels with pressure may even occur that can be presented using an angular overlap model.

The minor cation substitutions that control the order–disorder variants in mantle minerals are presented in Table 5.9.

TABLE 5.9

Minor cation substitutions and order–disorder variants that might affect EOS of mantle minerals (compiled by Hazen and Yang, 1999)

Mineral and composition	Cation substitutions	Order–disorder
Olivine $(Mg,Fe)_2SiO_4$	Ca, Fe^{3+}	Mg–Fe
Wadsleyite $(Mg,Fe)_2SiO_4$	Fe^{3+}, H	Mg–Fe
Spinel $(Mg,Fe)_2SiO_4$	Fe^{3+}, Ti	Mg–Si
Pyrope $(Mg_3Al_2Si_3O_{12})$	Ca, Fe, MgSi–2Al	Mg–Si; Ca–Mg
Majorite $(Mg,Fe)SiO_3$	Ca, Al, Fe^{3+}	Mg–Al–Fe^{3+}–Si; Ca–Mg
Clinopyroxene $(Mg,Fe,Ca)SiO_3$	Na, K, Al, Fe^{3+}, Ti	Mg–Al–Fe^{3+}–Ti–Si; Ca–K–Na
Orthopyroxene $(Mg,Fe)SiO_3$	Ca, Al, Fe^{3+}	Mg–Al–Fe^{3+}–Ca
Perovskite $(Mg,Fe)SiO_3$	Ca, Al, Fe^{3+}	Mg–Al–Fe^{3+}–Si
Anhydrous B $(Mg,Fe)_{14}Si_5O_{24}$	Al, Fe^{3+}	Mg–Fe^{2+}–Al–Fe^{3+}–Si
Magnesiowustite (Mg,Fe)O	Fe^{3+}, vacancies	Fe^{2+}–Fe^{3+} vacancies

5.10.5. Incommensurate phases

Incommensurate phases occur in systems when competing periodicities of the two lattices, such as basic and atomic, show misfits when packed together.

An incommensurate quantity is a periodic distortion of an otherwise regular lattice (displacive incommensurability).

The incommensurate wave is made up of an amplitude wave (*amplitudon*) and a phase wave (*phason*). The spatially modulated electron density forms the *charge-density waves* (CDW). The periodic distortion accompanying the CDW (due to interaction between the conduction electron and the lattice) is responsible for the incommensurate phase.

Incommensurate phases are commonly encountered in metal oxides, sulfides and other materials where point defects (vacancies) order themselves, giving rise to superstructures. Many insulating solids exhibit incommensurate phases. The phase transitions generally occur in the order: normal → incommensurate → commensurate as the temperature is lowered.

A modulated structure is described as a periodic or partly periodic perturbation of a crystal structure with a repetition distance appreciably greater than the basic unit-cell dimensions. For the incommensurate phase, a unit cell cannot be defined. No unit cell can contain an exact period of both the wave and the underlying crystal structure. Accompanying the phase transitions, anomalies in electrical resistivities of the chalcogenides are observed.

5.10.6. Order of transition: first order and second order

First-order transition is associated with significant hysteresis. (*Note*: Hysteresis effects are used to characterize the "order" of a transition.)

The Clausius–Clapeyron equation describes the thermodynamics at a first-order transition:

$$\frac{dP}{dT}\ \frac{\Delta S}{\Delta V}\ \frac{\Delta H}{T\Delta V}$$

Second-order transition is associated with some disordering process. The ordering parameter becomes unity for a perfect order while at perfect disorder it is zero. In second order transition, ΔV and ΔS have zero values.

Landau's theory provides the basis for second-order transitions. In second-order or structural transitions, the symmetry of the crystal changes discontinuously. Second- and higher-order transitions are often referred to as *continuous transitions*. In a second-order transition, the soft-mode frequency is zero at T_c while, in a first-order transition, the change of phase occurs before the mode frequency reaches zero.

5.10.7. Order parameters

Examples: For ferromagnetic to paramagnetic transition the order parameter is *magnetization*.

For ferroelectrics such as $BaTiO_3$, the order parameter is *polarization*.

For phase transition of $SrTiO_3$, the order parameter is *the angle of rotation* of the oxygen octahedra. In this transition, one of the optic modes of $SrTiO_3$ exhibits softening behaviour (i.e., *soft modes*). A soft-mode behaviour under pressure has been examined by Samara (1984). It is known that not every phase transition is associated with a soft mode. Phase transitions in some ferroelectrics may result from lattice dynamical instability.

5.10.8. Superlattice ordering

Superlattice ordering of point defects has been found in metal halides, oxides, sulfides and other systems.

5.10.9. Structural changes

On heating, CsCl will transform to NaCl structure, while a distorted perovskite would transform to a cubic form. For the former, *reconstructive transition* (Buerger, 1951) is invoked.

In *displacive transition*, only small changes in the arrangement of coordination polyhedra occur.

Structural transitions can be *ferrodistortive* — with no change in the number of formula units in the unit cell (e.g., ferroelectric materials) and *anti-ferrodistortive* — with changes in the number of formula units in the unit cell (e.g., both ferroelectric and anti-ferroelectric materials).

5.10.10. Phase changes: principles and types

In high-pressure phase-transition studies, the structure of the heavier element compounds at ambient conditions usually correspond very well to the high-pressure polymorph of the lighter element compounds in the same group of the Periodic Table. Isostructural compounds are different only in the types of cations. It is possible that compounds having smaller cations require higher pressure to undertake the same type of phase transition at the same temperature. In such cases, repulsion in a polyhedron dominates over the transition.

A phase transition is called *first order* when the transition occurs with a discontinuous change in the structure and entropy, and, hence a latent heat, at the transition temperature. It is called *second order* where the structure of the low-temperature phase merges continuously with that of the higher temperature phase at the phase transition, with no discontinuous change in the entropy and hence no latent heat.

Displacive-phase transitions involve small motions of atoms to change the symmetry of the crystal structure (*see* Fig. 5.16). For example, in the case of quartz, cristobalite and leucite, the phase transitions involve small translations and rotations of the

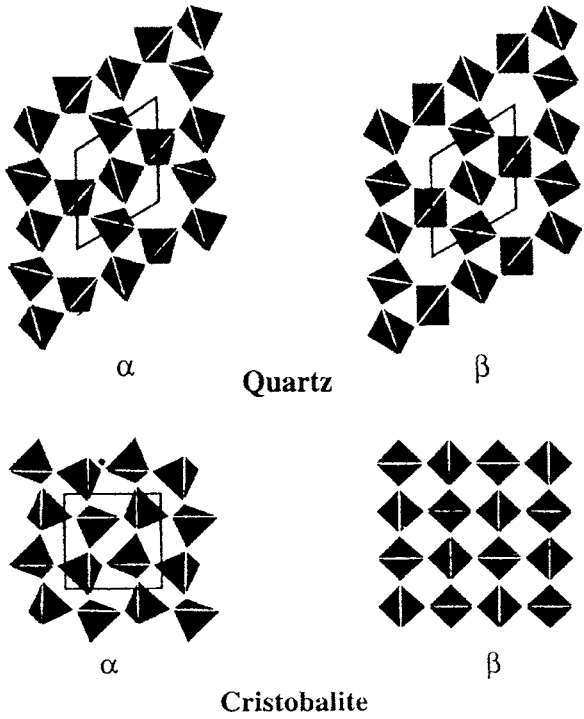

Figure 5.16. Displacive phase transitions in minerals. In each case α is the low-temperature phase and β is the high-temperature phase. In these the displacive phase transition occur as a result of rotations and translations of the nearly rigid tetrahedra (Dove, 1997, © 1997 Mineralogical Society of America).

$(Si,Al)O_4$ tetrahedra (Fig. 5.16; Dove, 1997). In the case of displacive transitions, an octahedra may rotate about the [001] axis (e.g., TiO_6 in $SrTiO_3$) while, in some, the octahedra tilt by different amounts about all three axes (e.g., TiO_6 and SiO_6 octahedra in $CaTiO_3$ and $MgSiO_3$, respectively).

5.10.10.1. Thermal transformations

The thermal transformations affecting a crystal are guided by the following three rules:

Rule 1
The effect of temperature is scalar and the deformation of a crystal can be described by a second-rank tensor.

Rule 2
Anharmonicity of thermal oscillations of atoms cause an increase in interatomic distance affecting the thermal expansion. More anharmonic oscillations with higher amplitudes (i.e., weaker bonds) manifest greater thermal expansion.

Rule 3
An increase in the thermal motion (vibrations, rotations and jumps) of atoms, etc., allows an increase in the crystal symmetry through raising the vibrational symmetry of the atoms, ultimately leading to more symmetrical high-temperature modification.

5.10.10.2. Soft modes

Each vibrational mode of a crystal structure is associated with a specific periodic distortion of the structure. When a high-temperature symmetric phase is cooled, the frequency of the "soft" mode decreases. When it becomes zero, the structure can hardly continue with the distortion and transforms to a lower symmetry phase. The word "soft" denotes crystal that yields to the displacements of atoms. Thus, in the high–low transition of quartz, softening takes place in the normal lattice mode, occurring at 208 cm^{-1} in the high-temperature form. This soft mode is Raman active. (*Note*: In a zone-centre transition, the lattice mode can be measured by Raman or IR spectroscopy, although symmetry-dependent selection rules would define which modes are active or inactive.)

The soft-mode frequency reaches zero at the Brillouin zone boundary, at points with the appearance of new reflections in the diffraction pattern of low-temperature form. Soft modes may be optic modes or acoustic modes.

Crystal structure changes through mode softening can be evaluated by the change in some order parameter (e.g., Q) as a function of temperature. In quartz, for example, the order parameter is related to the tilting angle, η, of SiO_4 tetrahedra while, in the perovskite structure, it is the angle of rotation, φ, of the octahedra.

5.10.10.3. Order parameter (η). Free energy and transition temperature

The free energy of the low-temperature phase can be written as a power series in the order parameter η as (Dove, 1997):

$$G(\eta) = G_0 + 1/2\,A\eta^2 + 1/4\,B\eta^4 + \cdots \tag{5-88}$$

where the parameters A and B are constants and G_0 is the free energy of the system for $\eta = 0$ (Dove, 1993). Usually, $G(\eta)$ is independent of the sign of η and, therefore, only contains terms with even powers of η.

Equation (5-88) represents an expansion of the free energy about a maximum value in the low-temperature phase and is, therefore, expected to be valid only for small values of η, i.e., only close to the phase transition.

For the free energy of equation (5-88) to represent a phase transition, it is necessary that the value of A changes sign at the transition temperature so that it is positive for temperatures above the transition temperature T_c and negative for those below. The simplest implementation of this condition is to assume that $A = a(T - T_c)$. It is also assumed that we only need to consider the smallest number of terms in the expansion so that we can rewrite equation (5-88) as

$$G(\eta) = G_0 + 1/2\, a(T - T_c)\eta^2 + 1/4b\eta^4 \tag{5-88.1}$$

where a and $b(= B)$ are positive constants. The equilibrium condition $\delta G/\delta\eta = 0$ applied to equation (5-88) leads to the predictions that $\eta = 0$ for $T > T_c$, that there is a continuous (second-order) phase transition at $T = T_c$ and that at, lower temperatures, η is non-zero and has the temperature dependence:

$$\eta = \left[\frac{a(T_c - T)}{b}\right]^{1/2} \tag{5-89}$$

When the constant b is negative, the form of the free energy gives a discontinuous (first-order) phase transition and the expansion of the free energy must be taken to a higher order (*see* Dove, 1993, Appendix D). The order parameter can be described by the above equation for temperatures down to 100–200 K, when the effects of the Third Law of Thermodynamics becomes important. This relation holds good at temperatures below T_c but, at very close to T_c, it takes the general form

$$\eta = a(T_c - T)^{\beta} \tag{5-90}$$

A term of the form PV could be added to the free energy, noting that the change in volume at a phase transition usually scales as $\Delta V \propto -1/\eta^2$. At increasing pressure, the value of η^2 at 0 K is likely to increase.

Since the electrons responsible for the JT effect are on the outside of the ions, they interact strongly with the lattice, giving rise to structural-phase transitions (at high temperature). The major products of electronic-phase transitions may be classed under:

(a) *Ferromagnets*. In these, long-range magnetic order below the Curie temperature induces a spontaneous magnetization, M_s, resulting in many magnetic domains, each with a M_s vector oriented in a direction different from that in adjacent domains.

(b) *Ferroelectrics*. These are characterized by different orientational states below T_c but the spontaneous polarization is induced by cooperative crystallographic distortion. In these, the domain boundaries can be controlled by an external field.

(c) *Ferroelastics*. In these, a cooperative crystal distortion induces a spontaneous strain below T_c. The domain boundaries of a ferroelastic can be controlled by applied stress.

5.10.10.4. Landau theory

Landau theory is effectively employed in describing the thermodynamics of phase transitions (e.g., Salje, 1992). Odd terms in the Landau free energy force the phase transition to be first order.

Ferromagnetic phase transition. Landau theory works well over a wide range of temperatures for displacive-phase transitions such as ferromagnetic-phase transitions. The mean-field theory of ferromagnetism predicts that the magnetization will vary as $|T_c - T|^{1/2}$ and the magnetic susceptibility will vary as $|T_c - T|^{-1}$, regardless of the specific details of the magnetic ordering. Landau theory predicts identical behaviour.

For magnetic-phase transition at temperatures close to transition temperature, the magnetization is found to vary as $|T_c - T|^{\beta}$ with $\beta \approx 0.38$, and the susceptibility as $|T_c - T|^{\gamma}$ with $\gamma \approx 1.3$.

Landau theory gives a good approximation to the free energy. The framework of Landau theory can allow the relationship between different phase transitions in the same material to be understood, such as when there is an Al–Si ordering-phase transition and a displacive-phase transition. By employing Landau theory, many questions may be answered by symmetry arguments. In Al–Si ordering-phase transition, the energy required to form Al–O–Al linkages is quite large ($\sim$40 kJ mol^{-1} or more; Dove et al., 1996) and the cations only disorder in equilibrium at temperatures well above the melting points. Strangely, there exists a wide range of ordering temperatures, even to low temperatures, and there is also some mechanism that allows disordering for a phase transition to occur.

Ferroelastic transition. For ferroelastic phase transitions, one may consider only the strain-order parameter coupling. This leads to re-normalized elastic constants, which reflect the inverse susceptibility. In the pressure range where the orientation strain ellipsoids remain invariant, the strain-order parameter coupling also remains invariant. Such high-pressure phase transition can, therefore, be treated in the same Landau manner as many high-temperature structural-phase transitions.

Ferroelectric-phase transition. In $PbTiO_3$ perovskite, Pb^{2+} and Ti^{4+}cations are off-centre along [001] to generate a ferroelectric-phase transition. (*Note*: In a ferroelectric-phase transition, small changes in the atomic positions generate a macroscopic dielectric polarization.) $BaTiO_3$ is well known for this ferroelectric-phase transition. In the high-temperature cubic phase, the Ti^{4+} atoms are potential-energy maxima.

The potential-energy minima for the Ti^{4+} cations are located away from the central site along the eight $\langle 111 \rangle$ directions. In the high-temperature phase, the Ti^{4+} cations hop among the eight different sites. When the Ti^{4+} cations lie preferentially in the sites in the positive *c*-direction, the ferroelectric-phase transition occurs. Still, four of these remain. Therefore, on further cooling, there are subsequent phase transitions leading to all Ti^{4+} cations occupying the same single site in the unit cell. Ferroelectric-phase transitions that involve the ordering of a proton between the two sites on a double-well hydrogen bond, such as in KH_2PO_4, are a further extreme example of this (e.g., Lines and Glass, 1977).

Such transitions may be considered as displacive, with small atomic displacements, or else as an order–disorder transformation. But in the displacive case, very little of the entropy is configurational, whereas in the order–disorder case the entropy is mostly configurational.

Displacive-phase transitions can be understood in terms of soft-mode theory, which developed from a better understanding of lattice dynamics using inelastic neutron-scattering techniques (Ghose, 1985, 1988).

The theory stands on the observation that, on cooling toward the transition temperature, the frequency of the lattice vibration falls to zero. A vanishing frequency implies a vanishing restoring force against the corresponding deformation. For this reason, it is called a soft mode. The atomic displacements associated with the soft mode are the same as the deformation of the structure in the low temperature.

Displacive transition: polymorphism. In displacive transition, the primary bonds in the structure are distorted. Symmetry change occurs, usually between high- and low-pressure/temperature forms (e.g., between high and low quartz at 573°C). In this transition, as the temperature decreases, the high-symmetry structure becomes unstable relative to some specific distortion. A displacive can be continuously monitored in terms of temperature (or pressure) and bond angle. This transition is usually fast and involves only small changes in energy. No change in translational symmetry occurs, i.e., the unit cell is essentially the same for both the polymorphs. This is known as *zone-centre transition.*

Reconstructive transition

Olivine(α) → spinel(γ). In olivine structure, oxygen atoms constitute a hexagonal close-packed array with Mg, Fe occupying half of the octahedral sites and Si occupying one-eighth of the tetrahedral sites. The close-packed oxygen layers are parallel to (100). In spinel structure, the oxygens are nearly close-packed cubic. Transition from olivine to spinel does not call for a coordination change of cations but the linkages between the cation polyhedra become more compact, which may account for the density increase by ~8%. The volume reduction implies a reduction in the effective radius of oxygen.

The mechanism for olivine–spinel transformation may be martensitic in nature and hence diffusionless. This involves the passage of partial dislocations on alternate close-packed oxygen layers to convert the hexagonal close-packing of olivine to cubic close packing in spinel. For this transformation, cation displacements (i.e., synchroshear) are needed.

In the martensitic mechanism, close-packed layers in olivine and spinel are parallel, i.e., the topotactic relation of $(100)_{ol}$ parallel to $(111)_{sp}$ holds.

β-Olivine → spinel(γ). The structural relation between β-(wadsleyite) phase and γ-(spinel) phase is such that one can be transformed to the other by the passage of partial dislocations with Burgers vector equal to this glide operation. A glide-plane displacement converts the existing glide to a mirror and vice versa. The stacking fault, which thus results, shows a local structure of the other phase. Therefore, a stacking fault in

a β-phase has the spinel structure. This is how stress-generated dislocations provide nucleation sites for phase transformations to proceed.

$\beta-\gamma$ transition depth in a subducting slab: Plunging velocity. The nucleation and growth mechanism in a subducting slab can be activated beyond the cut-off temperature of $\sim 700°C$. When the velocity of the downgoing slab is high, the overpressure will be high and olivine becomes metastable. When the temperature goes beyond the cut-off temperature, the rate of transition to spinel will be rapid enough to increase enormously the change in free energy (i.e., ΔG), causing implosive transition. This energy release as seismic waves causes the deep-focus earthquakes in downgoing slabs. The depth for transition to occur decreases with decrease in plunging velocity. A greater subduction rate means a greater depth at which the $\beta-\gamma$ transition will take place.

Driving forces for phase transition. There are two mechanisms for driving the phase transition to occur. First, a force should exist to distort the structure locally and, secondly, some interaction should exist to give a coupling between local ordering processes. The operation of the forces can be illustrated with the cases of $BaTiO_3$ and aluminosilicates.

In $BaTiO_3$, the Ti^{4+} cation hops between sites of local potential energy minima that give rise to the local distortions of the structure at low temperatures. The Ti^{4+} cations in neighbouring unit cells interact and force each other to order in the same way.

Similarly, in many aluminosilicates, the large cavities formed by the framework of linked SiO_4 and AlO_4 tetrahedra are occupied by cations such as K^+ and Ca^{2+}. In these phase transitions, both displacement of the cations from the centres of the cavities and collapse of the framework are involved. It is possible that the cations rattling around in their cavities will like to order and also that some mechanism should develop for ordering the cations in the neighbourhood as well. Coupling of these would bring forth the transformation of the structure.

For displacive-phase transitions in silicates, there are two aspects for the driving forces.

First, there is coupling between local ordering or deformation and the neighbouring atoms that allows long-range ordering, described by parameter J in the standard paradigm. In silicates, it arises from the stiffness of the tetrahedra that leads to a local deformation propagating over large distances.

Second, there is a longer range force that drives the actual deformation, which is described by the doubled-well potential $V(\eta)$, discussed in Section 5.10.10.6. below.

5.10.10.5. Landau order parameter

For a structural distortion, change in free energy is associated with the changes in enthalpy and entropy. The latter two can be measured calorimetrically.

The variation in free energy can be related to the interaction energies between the atoms. Again, the macroscopic properties such as strain, optical birefringence and site occupancy change the thermodynamic properties.

The Landau order parameter, Q, is related to the change in some macroscopic property through the phase transition. Change of order parameter with temperature describes the thermodynamic process of the ensuing phase transition. For example, in the

transition from tetragonal to orthorhombic structure, the optical indicatrix changes from uniaxial to biaxial, while the change in birefringence (which is equivalent to the degree of transformation) is directly proportional to Q, the order parameter. A discontinuity in the change in Q is marked by the critical temperature, T_c, of the phase transition.

Strict symmetry rules define the form of order parameter in relation to the change in symmetry. The correct form of the order parameter and its relationship to certain physical properties for a given change in symmetry is available in standard tables. Usually, the measured properties scale as Q or Q^2.

5.10.10.6. Origin of doubled-well potential, $V(\eta)$

There are three contributors to the doubled-well potential, $V(\eta)$, in silicate phases (Dove et al., 1995).

First, the *long-range interactions*, mostly arising from interactions between the highly polarizable O atoms. These are attractive and tend to contract the structure to the densest state possible, but the collapse is thwarted by short-range pepulsive interactions.

Second, the *short-range interaction* between a cation (e.g., K^+ or Ca^{2+}) occupying a large cavity site and neighbouring O anions. However, a collapse of the cavity about the cation may take place and the effect may propagate over large distance.

Third, the *energy with the Si–O–Si (or Al–O–Al) bond angle*, which is ideally $\sim 45°$. Bond angles differing from this value will have a higher energy. For high-temperature cristobalite, this angle enlarges to 180° (Schmahl et al., 1992) and this is associated with a disorder with neighbouring tetrahedra, which tend to rotate to reduce this angle (Swainson and Dove, 1995). To have as many bonds as possible to lead to an ideal bond angle, the structure should undergo displacive-phase transition. When the Si–O–Si bond angle is near the ideal value ($\sim 45°$), the energy associated with this bond will oppose phase transition or else phase transition will involve the *rigid-unit mode* (RUM) distortion (of SiO_4 tetrahedra) with the smallest distortion of the Si–O–Si bond angle (Dove et al., 1995). RUM is discussed below.

5.10.10.7. Rigid-unit mode: "split atoms" and energy spectra

The existence of RUM in framework silicates is not trivial. Each tetrahedron has six degrees of freedom (F). Each corner has three constraint equations that link it to the corner of the connected tetrahedron, so the number of constraints per tetrahedron is also six. Thus, the connected tetrahedra in a framework silicate, constrained with $F = C$ (total number of constraints), should have no modes of deformation. Some computational methods have been developed to determine all RUM for a given framework structure, taking account all possible wave vectors (Hammonds et al., 1994).

Each tetrahedron is taken as a rigid body and atoms shared by two tetrahedra are counted as two separate atoms, called "split atoms". Any mode of deformation rotating or translating the rigid tetrahedron may cause the split atoms to separate. This concept can be incorporated into the formalism of molecular lattice dynamics (Dove, 1993, Chapter 6). The RUM are then the vibrational modes calculated to have zero frequency. The number of RUM in any structure is usually small (but greater than zero) compared with the total number of wave vectors (Hammonds et al., 1996). On constraining tetrahedra as perfectly

rigid holding no intertetrahedral forces, the RUM are the modes with zero frequency but, in reality, the inter-tetrahedral forces will be non-zero and these will lead to an energy spectrum for the RUM (e.g., in cristobalite, the RUM energies are of the order 0–1 THz; Dove et al., 1995).). In the high-T phase of SiO_2, the Si–O–Si bond angle is near to the ideal value and a few rigid-unit mode (RUM) distortions do not involve change in this angle.

5.10.11. Pressure-induced order–disorder

Effects of pressure on atomic order–disorder in crystalline phases have received much attention because of their importance in geophysics, solid state physics and material science (*see* Hazen and Navrotsky, 1996). Pressure-induced order–disorder phenomena play a key role in the energetics, crystal chemistry and physical properties of solids such as minerals, ferroelectic materials, alloys, fullerenes and high-temperature superconductors. Order–disorder transition may alter crystal symmetry, causing changes in electrical and thermal conductivity, vibrational spectra and elastic moduli. Systematic studies on atomic order–disorder, compressibility and crystal chemistry of mineral phases are essential to obtain more realistic EOS for mantle phases that exhibit ordering-dependent properties.

Cation order–disorder can significantly modify high-pressure behaviour. In addition to structural and compositional factors, cation order–disorder also plays an important role in determining the elastic properties of crystalline phases. Even the properties of ferroelectrics and cuprate superconductors may be tuned by pressure. Cation disorder can increase compressibility (Hazen and Yang, 1997).

Pressure-induced ordering is an unexpected phenomenon. Garnet group minerals, which are cubic in structure, occur above 400 km. At higher pressures, they become tetragonal through an ordering of the contents of the octahedral and dodecahedral sites (Angel et al., 1989). Similarly, a large degree of ordering is seen in wadsleyite, β-$(Mg,Fe)_2SiO_4$ (Finger et al., 1993). High-pressure cation ordering has been observed in olivine (Aikawa et al., 1985), wadsleyite (Finger et al., 1993), garnets (Hazen et al., 1994) and in anhydrous phase-B (Hazen et al., 1992). This aspect has been discussed in sections relating to some of these minerals.

Hazen and Navrotsky (1996) reviewed the effects of pressure on order–disorder reactions and demonstrated that many phases display a significant volume disordering:

$$\Delta V_{\text{dis}} = V_{\text{disordered}} - V_{\text{ordered.}}$$

Silicates with Mg–Fe ordering commonly have ΔV_{dis} up to 0.5%, while values exceeding 2% obtain for some mixed-valence oxides and sulfides. Some (e.g., Liebermann et al., 1977) used velocity–density systematics to infer that cation ordering affects spinel elasticity. Cation ordering can also influence the EOS; e.g., the bulk modulus of stoichiometric pseudo-brookite-type $MgTi_2O_5$ is seen to vary by 6%, depending on the ordered state of Mg and Ti in two different octrahedral sites.

AB_2O_4 spinels ($Fd3m$) have two octahedrally coordinated cations for each tetrahedrally coordinated cation. "Normal" spinels are fully ordered ($^{[4]}A^{[6]}B_2O_4$).

For the intermediate form, $(^{[4]}A_{0.33}B_{0.67})\ ^{[6]}(A_{0.67}B_{1.33})O$, maximum disorder occurs on both tetrahedral and octrahedral sites.

5.10.11.1. Fe–Mg ordering in silicates

Recent high-pressure studies of the phases appearing in the system MgO–FeO–SiO_2 including wadsleyite (Finger et al., 1993), anhydrous B (Hazen et al., 1992) and olivine (Aikawa et al., 1985) have indicated that pressure may induce significant Mg–Fe ordering. Pressure-induced ordering may play a significant role in cation distributions, phase equilibria and element fractionations in the mantle. In orthopyroxene, ordering may affect its elasticity (Bass and Weidner, 1984) and thermochemical properties (Chatillon-Colinet et al., 1983).

The Fe–Mg order–disorder equilibria in pyroxenes and amphiboles can be used as a powerful means to determine temperature–time paths of metamorphic and igneous rocks on the Earth and the Moon. This principle can help the use of thermodynamic calibrations of heterogeneous phase equilibria between co-existing minerals in xenoliths entrained in basaltic and kimberlitic magmas and help to clarify the oxidation state of the Earth's upper mantle.

An extension of such a study can include the crystallographic controls of Fe^{3+} and Fe^{2+} in lower-mantle phases and thus can allow modelling of the oxidation state of the lower mantle. This would help to answer questions pertaining to the Earth's early evolution.

The degree of ordering of Mg and Fe between two octahedral sites, M1 and M2 (in olivine/orthopyroxene), is expressed by the distribution coefficient:

$$K_D = (Fe_{M1}/Mg_{M1})/(Fe_{M2}/Mg_{M2}).$$

Orthopyroxenes, having two very different octahedral sites, when allowed to equilibrate at low temperature, order strongly. Fe orders into the more distorted M2-site, while Mg prefers the smaller M1-site. K_D values as large as 0.50 have been reported for samples annealed at temperatures below 500°C, whereas samples heated to 1,000°C and rapidly quenched typically have K_D values between 0.2 and 0.3. Above 1,000°C, most Mg-silicates manifest nearly complete disorder (Virgo and Hafner, 1969) (*see* Section "Intra-crystalline Mg–Fe ordering" of Chapter 6).

A completely ordered mineral has a $K_D = 1$, whereas the completely disordered one has $K_D = 0$. The K_D values of some minerals are cited below as examples:

Minerals	K_D	Reference
Olivine	1.8	Finger and Virgo, 1971
Wadsleyite	2.7	Finger et al., 1990
Grünerite	2.3	Finger, 1969

Fe–Mg distribution: three-component lower mantle. In the lower mantle, the atomic proportions of Fe and Mg in the co-existing phases of perovskite and magnesiowüstite may be discussed with reference to a simplified formula relationship as described below.

Writing $f = \mathrm{Fe}/(\mathrm{Fe} + \mathrm{Mg})$ in atomic ratio, with subscript 1 for perovskite and 2 for magnesiowütite, the relations are found to be (Stacey and Isaak, 2000):

$$\rho_1 = 4104\,(1 + 0.272 f_1 - 0.012 f_1^2)\ \mathrm{kg\ m^{-3}}$$

$$\rho_2 = 3209\,(1 + 0.701 f_2 - 0.061 f_2^2)\ \mathrm{kg\ m^{-3}}$$

and

$$\bar{\rho} = (1 - x)\rho_1 + x\rho_2$$

for a volume fraction x of magnesiowütite. The two molecular weights are $m_1 = 100.389 + 31.542 f_1$ and $m_2 = 40.304 + 31.542 f_2$, so that

$$\bar{f} = \frac{[(1 - x)\rho_1 f_1/m_1 + x\rho_1 f_2/m_2]}{[(1 - x)\rho_1/m_1 + x\rho_2/m_2]} \tag{5-91}$$

If the lower mantle is composed only of (Fe,Mg)SiO_3 perovskite and (Fe,Mg)O magnesiowütite, then the overall ratio is tightly constrained to 0.220 ± 0.005 (independently of other assumptions). Arguments based on cosmic abundance and the composition of meteorites, xenoliths and peridotites strongly suggest that $\bar{f}$ is ≤ 0.11 for the whole mantle (O'Neill and Palme, 1998). The apparent high value of $\bar{f}\,(= 0.22)$ for lower-mantle mineralogy probably suggests the signature of $CaSiO_3$ perovskite in the lower mantle. Therefore, one must contemplate a three-component model for a more definitive explanation of the results for the lower mantle.

5.10.11.2. Structural disordering and twinning

In crystals, four types of structural disorders involving atoms are encountered, as discussed below.

(1) *Substitutional disorder*. This is the most common type of disorder seen in the mineral kingdom, covering felspars, ferromagnesian silicates, spinels, carbonates, etc. This disorder is also seen in non-stoichiometric crystals in which defects occur as missing atoms (vacancies), e.g., wüstite $Fe_{1-x}O$ and oxide superconductor $YBa_2Cu_3O_{7-x}$ (Hazen, 1990) or as interstitial excess O, as in La_2NaO_{4+x} (e.g., Chaillout et al., 1989).

(2) *Positional disorder*. Static positional disorder, for example in albite ($NaAlSi_3O_8$), Na atoms, occupy four distinct mean positions in different unit cells, depending on the local arrangement of Al and Si (Winter et al., 1977). This contributes to the thermal vibrational disorder.

(3) *Rotational disorder*. Rotation of CO_3 groups along an axis is seen in rhombohedral carbonates (Ferrario et al., 1994); molecular crystals such as H_2 (Mao and Hemley 1994) and C_{60} (Fischer and Heiney, 1993) show rotational disorder under pressure.

(4) *Distortional disorder*. Quartz (α-SiO_2) can distort from a high-symmetry form in more than one equivalent way (Kihara, 1990); the perovskite-type structure also show distortional disorder.

Beyond a critical orientational disorder, a system evolves to an amorphous state. This is consistent with the critical disorder model of amorphization proposed in the context of ion implantation-induced amorphization (Riviere, 1977).

5.10.11.3. Free energy and order parameter (Q)

The free energy (G) of a phase with a possible iso-symmetric transition has been expressed by Christy (1994) in terms of an order parameter, Q, representing some structural distortion as

$$G = aQ + bQ^2 + cQ^3 + dQ^4 + \cdots \tag{5-92.1}$$

with an extensive variable such as temperature and or pressure. When some of the coefficients in the above relation are changed, a phase transition could be introduced between structures of the same symmetry but with distinct stable values of Q. Christy also showed that such iso-symmetric transitions are necessarily first order and that when the free energy varies with P and T, the transition line may terminate at a critical point in P–T space. Around the extrapolation of the critical point in P–T space, a crossover region should occur of very rapid change in order parameter. The crossover line is defined as the locus of a minimum in $\mathrm{d}^2G/\mathrm{d}Q^2$ (where G = free energy and Q = order parameter). However, when there are no thermodynamic discontinuities, there should be no phase transition. However, in experiments, distinguishing a true crossover from a weak first-order iso-symmetric phase transition often becomes difficult.

In the equation (5-92.1), Q is assumed to remain homogeneous (i.e., the structural distortion remains constant in space) but when there is a mixing of two structural states (in unit-cell scale), the free energy is lowered and the order parameter Q becomes inhomogeneous. In two sublattices, Q may be denoted as Q_1 and Q_2, which, in a simple expression for G, would be related as

$$G = (1/2)\{a(Q_1 + Q_2) + b(Q_1^2 + Q_2^2) + c(Q_1^3 + Q_2^3) + d(Q_1^4 + Q_2^4)\} + (\lambda/2)(Q_1 - Q_2)^2 \tag{5-92.2}$$

The last term involves coupling between the two sublattices Q_1 and Q_2; higher order coupling terms may be omitted. In a homogeneous case, $Q_1 = Q_2$ and equation (5-92.1) reduces to equation (5-92.2).

Equation (5-92.1) can be recast in terms of two variables, Σ and Δ, [$\Sigma = (Q_1 + Q_2)/2$ and $\Delta = (Q_1 - Q_2)/2$] as follows:

$$G = \left\{a\Sigma + b\Sigma^2 + c\Sigma^3 + d\Sigma^4\right\} + \{(b + 2\lambda)\Delta^2 + d\Delta^4\} + 3c\Delta^2\Sigma + 6d\Delta^2\Sigma^2 \tag{5-93}$$

Evidently, the first term is equivalent to equation (5-92.2), representing the free energy of the system if Q is homogeneous with the average value Σ. The second term is equivalent to the Landau expansion for the free energy of a zone-boundary transition with order parameter Δ, for which the symmetry rules allow only even powers in the order parameter. The last terms are the symmetry-allowed linear-quadratic and bi-quadratic coupling terms between the order parameters of the iso-symmetric and zone-boundary transitions.

By equation (5-93), the stable structure predicted is governed by the sign of the coefficient of Δ^2. Again, if $(b + 2\lambda) < 0$, then $\Delta = 0$ becomes a local maximum and the minima are symmetrically placed on either side of $\Delta = 0$. Therefore, if b becomes more negative at reduced temperature or pressure, the high-symmetry phase will undergo a second-order transition to the cell-doubled structure. Depending on λ, this equilibrium line may intersect either the crossover in the high-symmetry phase or a segment of a first-order iso-symmetric transition line.

Tricritical/first-order transition. Higher order terms in equation (5-93) may be involved when one of the transitions from the low-symmetry to the high-symmetry phase are either first-order or tricritical in the Landau sense. For example, in anorthite, the transition is tricritical at room pressure (Redfern and Salje, 1987) whereas the transition at high pressure is first order in character (Hackwell and Angel, 1993, 1995). The phase-diagram topology may be characterized for the zone-boundary transition by an equilibrium line to be near-isobaric at high pressure and near-isothermal at high temperature.

5.10.11.4. Order parameter (Q) and strain (ε) in phase transition

When one tries to employ an extension of the Landau presentation of phase transitions to conditions of high pressure, the problem arising relates to the excess volume. When volume change is relatively small, a high-temperature phase transition normally accompanies a volume strain (Carpenter, 1992) in proportion to the square of the order parameter Q (i.e., $V_\varepsilon \propto Q^2$).

In a phase transition such as cristobalite I $\rightarrow$ II, both the symmetry breaking strain, ε^{sb} (E representation, equation (5-30)) and the non-symmetry-breaking strain (A_1 representation, volume) are proportional to Q^2 in the lowest order. This relation reflects the dependence on the square of the macroscopic order parameter Q for the tetragonal to monoclinic phase transition. Because the strain components change in proportion to each other (with P and T), the overall spontaneous strain ellipsoid changes in size, although not in orientation.

From different strain components, a total scalar spontaneous strain can be validly calculated (because of the constant $\varepsilon - Q$ coupling) as (Salje, 1990):

$$\varepsilon_{tot} = \sqrt{\sum_{i=1}^{6} \varepsilon_i^2} \tag{5-94}$$

where ε_i are the components of the spontaneous strain tensor derived (*see* Section 5.4).

5.10.12. Isosymmetric transitions

In recent years, high-pressure, single-crystal diffraction experiments have attained high precision, which has enabled the detection of a number of apparent phase transitions (cross/across) at high pressures manifesting no detectable symmetry change. In this cross through the phase transition, the space-group symmetry remains unchanged since the atoms within the unit cell occupy the same Wyckoff sites before and after the transition.

Such transitions have been termed "iso-symmetric" (e.g., Christy, 1995). This phenomenon is obviously seen in amorphous systems and gas–liquid transitions. Such iso-symmetric transitions have also been detected in some complex framework structures (e.g., orthopyroxene, clinopyroxene, anorthite, etc.) showing large degrees of internal structural freedom (Angel, 1996).

It is known that the free-energy changes associated with simple compression of a single phase are far greater than those associated with cooling to low temperature. Therefore, modest pressures can result in greater modifications to crystal structures and properties than do temperatures and new transitions may occur (Angel, 1996).

Nevertheless, the displacive-phase transition characteristics in minerals at high pressures often correspond fairly to high-temperature transitions. For example, the ferroic transition at high temperature in ilvaite, $CaFe_3O_8(OH)$, shows an order-parameter behaviour which is similar to that obtained at high pressure (Finger and Hazen, 1987). In co-elastic crystals (Salje, 1990), high pressures lead to an increase in elastic stiffness tensor and a coupling between strain and the order parameter of the transition.

Potasium titanyl phosphate (KTP) undergoes strongly first-order (3% volume change) iso-symmetric phase transition at $\sim$5.7 GPa, as does sodium-doped KTP (Allen and Nelmes, 1996). Such transitions are driven by significant changes in electronic structure, as exemplified by the orthorhombic $\rightarrow$ orthorhombic transition in $(La,Ba)CuO_4$ (Paul et al., 1987) and in complex framework structures. A large number of internal degrees of structural freedom are suppressed under pressure and some dynamic motion of the larger cations leads to iso-symmetric transitions (e.g., in anorthite).

5.10.12.1. Energetics of iso-symmetric transition

The energetics of phase transition between the high-symmetry structures in terms of an order-parameter approach show that the stability of the cell-doubled low symmetry of a phase arises simply from the development of inhomogeneity in the order parameter. Although the structural differences between the high-symmetry and low-symmetry phases and between the two high-symmetry structures are quite minor, the thermodynamic consequences of these changes can be quite significant. This is most clearly seen in the intersection of the crossover line with the low-to-high-symmetry transition boundary in anorthite (Hackwell and Angel, 1995). The high-pressure $P\bar{1} \Leftrightarrow I\bar{1}$ transition (in anorthite) is marked by the disappearance of the superlattice reflections (first-order transition). On the phase diagram, the phase boundary is almost isobaric.

5.10.13. Growth rates

The growth rate during an interface-controlled reconstructive polymorphic phase transition, involving diffusion across the inter-phase boundary, can be described by (Carbon and Rosenfeld, 1981)

$$x^0 = K_0 T \exp[-(H^* + PV^*)/RT][1 - \exp(\Delta G_r/RT)] \tag{5-95}$$

where K_0 is a constant, T is absolute temperature, H^* is the activation enthalpy, V^* is the activation volume for growth, ΔG_r is the Gibb's free energy change for reaction

(must be negative) and R is the gas constant (Christian, 1975). The first exponential is a *kinetic factor* describing the thermally activated diffusion of atoms across the inter-phase boundary. The rate of this process increases rapidly with temperature but decreases with increasing pressure, assuming that ΔV is positive. The second factor in brackets depends on the *thermodynamic driving potential* in the system.

ΔG_r can be approximated wherein ΔP is the overstep of pressure beyond equilibrium and ΔV is the transformation-volume change at the conditions of reaction. Hence, this factor is zero at equilibrium (where $\Delta G_r = 0$) and, therefore, the growth rate is zero. This factor approaches unity as ΔP increases.

For example, with increasing pressure at constant temperature, the growth rate of spinel during transformation from olivine first increases (due to thermodynamic factors) and then decreases (due to kinetic factors).

5.11. Charge distribution in ionic solids: valence and core states

In an ideal ionic solid, the valence charge is completely localized around an anion. Deviations from complete localization, manifested by reduced ionicities or by definite valence band-widths, indicate a measure of covalency in the bands. The distribution of the theoretical valence charge is expected to provide a more direct qualitative picture of the valency deduced from the band structure.

This can be illustrated with the example of MgO, as discussed by Bukowinski (1980).

The valence and core charge densities within the Mg and O spheres, computed at $V_0/V = 1.0$ (Figs. 5.17 and 5.18) show no more than 5% of the valence charge is located in the Mg sphere; its shape is suggestive of overlap tails from the oxygen ions. An analysis into spherical harmonics shows that the valence charge is primarily of p-like character on

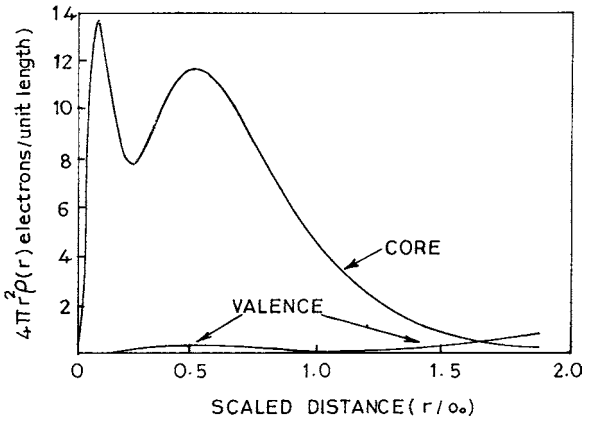

Figure 5.17. Core and valence charge density of MgO in the Mg sphere at $V_0/V = 1.0$; a_0 is the Bohr radius (Bukowinski, 1980, © 1980 American Geophysical Union).

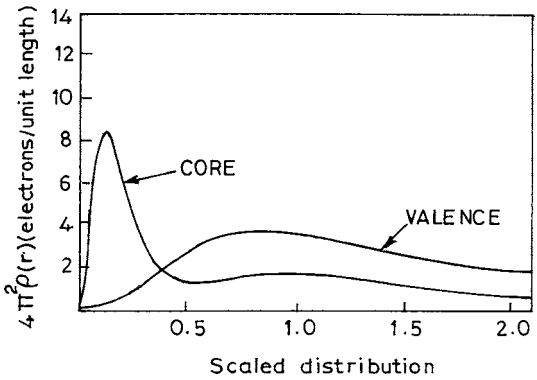

Figure 5.18. Core and valence charge density of MgO in the O sphere at $V_0/V = 1.0$ (Bukowinski, 1980, © 1980 American Geophysical Union).

both ions, with small amounts of other angular momenta induced by the crystal field. The small amount of valence charge in the Mg sphere may be understood as a consequence of the effective repulsion that arises from the orthogonalization of the valence states to the Mg $2p$ core states. Since the lowest empty states are at the bottom of the conduction band, the exchange repulsion of the valence charge is very efficient. Further evidence of this is found in the small effect that compression has on the amount of valence-charge overlap with the Mg^{2+} ion.

The core states of Mg and O have small but finite amplitudes at the sphere radii, indicating a certain amount of core–core overlap (Figs. 5.17 and 5.18). This is, of course, one of the sources of the repulsive potential between the Mg and O ions and is the reason why the O 2s and Mg 2p orbitals had to be treated as band states. In spite of this, the core density in the Mg sphere is practically indistinguishable from that of the free Mg^{2+} ion. Thus, in a first approximation, MgO could have valence electrons with the Mg^{2+} ions. The true picture is somewhat more complicated because of the presence of angular momentum components other than $l = 1$ and because more than one electronic charge is distributed outside the spheres. Thus, although the charge on the Mg ion is close to the nominal $+2$, the remaining charge is not entirely contained within the O sphere. Changing the radii has some effect on the charge distribution but this cannot completely eliminate the charge outside the spheres. With the model of equal touching spheres, the O and Mg core charge densities are approximately equal at the point of contact. Changing the sphere radii would transfer an unreasonable amount of core charge into the constant potential region. A model which best describes the calculated charge distribution would consist of Mg^{2+} ions that overlap with O cores that are of similar spatial extent. In addition, six valence electrons are distributed throughout the unit cell in such a way that only about 80% of the valence charge may be identified with the O site. This interpretation is in essential agreement with the experimental charge density (Adams, 1978).

However, a more accurate treatment of many-body effects is not likely to change the qualitative model presented above. Good agreement of the result of Bukowinski (1980)

with the charge density obtained with the empirical pseudopotential method and the measured charge density further supports this conclusion.

5.11.1. Ionic solid under compression: MgO

Compression should increase the valence charge density within the oxygen sphere, while the total charge within the sphere would decrease. However, the apparent incompressibility of the valence charge around the oxygen core may be a direct consequence of the high-potential energy that results from accumulating so much excess charge.

In the case of MgO, a high potential in the neighbourhood of the O core and the strong repulsion of the Mg ion (due to the large band gap) explains the low polarizability of MgO. The valence charge has virtually "no place to go". Added to this is the fact that the cores of O overlap with the Mg ion. These facts together account well for the large bulk modulus observed in MgO. In MgO, there is a small concentration of valence charge around $r = 0.5$ Bohr radii from the Mg site (Bukownsiki, 1980). The valence charge is also distributed throughout the whole unit cell and, in the neighbourhood of lattice sites, it resembles the corresponding atomic-valence states. In MO language, the valence states may be said to be composed of Mg 3s states and O 2p states (*see* Section 5.11).

Indeed, the computed electronic band structure and charge density coupled with experimental data suggest that the MgO valence electrons are distributed throughout the unit cell. This charge is possibly localized mostly with O ion, while an electronic charge is distributed between the two atomic spheres of Mg and O. However, a small part of this charge is localized near to the Mg site, where it mimics the Mg 3s state.

5.11.1.1. Band-gap change: implication in lower mantle

The band gap increases with pressure in the high-pressure regime of the Earth's mantle. Conduction band gaps play important roles in the thermal and electrical conductivity of the mantle. As compression increases, MgO attains a higher transparency to thermal radiation. At a temperature of a few thousand degrees, the thermal radiation shows the peak energy to be an order of magnitude lower than the MgO band gap. Thus, at the lower mantle, MgO should be a good conductor of radiative heat and a strong insulator to electricity.

Such a change in properties with band-gap change is of tremendous significance since the lower mantle is presumed to host a mixture of simple oxides, which would behave the way of MgO. However, in many such oxides, the systematics and models developed from zero-pressure data are likely to become unreliable when extrapolated to high pressure. In particular, cation substitution and compression can result in a substantial change in electron distribution around the neighbouring anion core. For example, the presence of Fe^{2+} cation impurity will form intrinsic d-levels and compression to lower-mantle densities will increase the overlap of the Fe^{2+} d-elections. Thus, as pressure increases, the Mg-silicates tend to become increasingly transparent to thermal radiation.

5.11.2. High-spin–low-spin transition

For transition-metal ions of d^4 to d^7 systems, high-spin and low-spin states are possible. The high-spin state is usually stable in oxides and silicates at normal pressures, except for the Co^{3+} ion. Since the ionic radius of the low-spin state is smaller than that of the high-spin state, an increased pressure will enhance the low-spin state by spin-pairing. The condition for HS $\rightarrow$ LS transition under pressure is that $\Delta G(P) = 0$. Usually, a contraction of the metal–ligand distance produces a large increase in the crystal-field splitting.

In a crystalline field, the degeneracy of Fe^{2+} 3d orbitals is lost and in an octahedral field they split into two sets of orbitals called t_{2g} and e_g. The difference between these two is the crystal-field splitting (10 Dq, commonly designated as Δ), which increases with decreasing Fe–O bond length, R. The ionic bonding model predicts the relation: $10\,\mathrm{Dq} \propto 1/R^5$.

The six d electrons (each with spin quantum number $S = 1/2$) of the Fe^{2+} cation can couple to give states with spin $S = 2$, 1 and 0. Because of exchange energy, both the t_{2g} and e_g orbitals are split into spin-up ($\uparrow$) and spin-down ($\downarrow$) sub-orbitals. The difference between these two sub-orbitals is expressed as U_{ex}. Usually, U_{ex} (for the t_{2g} orbitals) $= U_{ex}$ (for the e_g orbitals) but this is not always so. As can be seen in Fig. 5.19, the high-spin state $(S = 2)$ will be the most stable as long as $U_{ex} > 10\,\mathrm{Dq}$. A decrease in Fe–O bond length will increase 10 Dq and eventually U_{ex} will be smaller than 10 Dq. Thus, the low-spin $(S = 0)$ state will be most stable. From a different point of view, as the Fe–O bond length gets smaller, U_{ex} will decrease because of greater Fe–O covalency.

5.11.2.1. Energy change in spin transition

The difference of the total energy in the crystal between the high- and low-spin states is given by the change of the crystal-field stabilization and the spin-pairing energy in the transition-metal ion (*see* Fig. 5.19). The total energy (W) of the low-spin state is given by

$$-W_{LS}(V) = W_{HS}(V) + SN[\Pi(V) - \Delta(V)]$$

where S is the number of spin pairings (in octahedral coordination for d^4 and d^7 systems, it is 1 and for d^5 and d^6 systems, it is 2), N is the number of transition-metal ions in a crystal and Π is the spin-pairing energy.

The high-spin state $(^6A_{1g})$ at normal pressure has the crystal-field splitting, Δ smaller than the spin-pairing energy, Π. When Δ exceeds Π at high pressures, the low-spin state $(^2T_{2g})$ becomes more stable than that of high-spin Fe^{3+} ($r = 0.645$ Å). The volume change associated with the spin transition can be evaluated as 13% from the plot of the cell volume against the ionic radii systematics for the corundum structure sesquioxide (Fig. 3.10). This observed relationship is generally valid where both Δ and Π depend on the volume of the crystal.

In accordance with Griffith (1956), Π can be written with Racah parameters for d^4, d^5, d^6 and d^7 systems as $6B + 5C$, $(15/2)B + 5C$, $(5/2)B + 4C$, respectively. The spin-pairing energy is proportional to the Racah parameter B, since the ratio B/C is almost

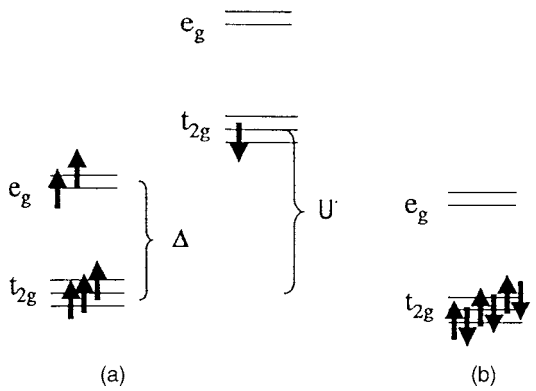

Figure 5.19. Schematic of occupancies of states (a) high-spin and (b) low-spin ferrous iron (*Courtesy*: R.E. Cohen).

constant (Tanabe and Sugano, 1954). The Racah parameter B describes the effects of repulsion between electrons of a given ion. An increase in the degree of covalency between a metal ion and its ligands by increased pressure would be accompanied by the spreading out of the electron charge cloud and, therefore, reduction of the repulsion and the value of B. For the volume dependence of Δ and Π, the simple power-law formulae hold as

$$\Delta = \Delta_0 (r/r_0)^{-m}$$

$$\Pi = \Pi_0 (r/r_0)^{n},$$

where m and n characterize the volume dependence of the crystal-field splitting and spin-pairing energies, respectively. In the case of Cr^{3+} in Al_2O_3, the value of n is estimated from the pressure dependence of B as about 1.0 (Goto et al., 1979). For Fe^{3+} in Fe_2O_3, the values of Δ_0 and Π_0 are obtained as 21.86 and 4.07×10^{-12} erg, respectively (Lehmann, 1970). In the case of Fe^{2+} in MgO, the value of m is estimated to be 3.0 from optical data at high pressure (Sankland, 1968).

The EOS of low-spin form is derived by using the derivation of $-W_{\mathrm{LS}}(V)$ with respect to V as

$$P_{\mathrm{LS}}(v) = \frac{-\mathrm{d}W_{\mathrm{LS}}(v)}{\mathrm{d}V} + SN\left[\frac{\mathrm{d}\Delta v}{\mathrm{d}V} - \frac{\mathrm{d}\Pi(v)}{\mathrm{d}V}\right] \tag{5-96}$$

According to Ohnishi's (1978) theory, the Birch–Murnaghan EOS adopted for high-spin state is

$$P_{\mathrm{HS}}(V) = (3/2)[(V/V_0)^{-7/3} - (V/V_0)^{-5/3}]K_0 x\{1 + (3/4)(K_0' - 4)[(V/V_0)^{-2/3} - 1]\}$$

Internal energy change. The free energy of HS → LS transition at constant T and P is

$$\Delta G = \Delta U - T\Delta S + P\Delta V$$

ΔU: The change in internal energy ΔU for HS → LS transition is simply the energy difference between ${}^5T_{2g}$ and ${}^1A_{1g}$ states of Fe^{2+} cations (${}^5T_{2g}$ is the spectroscopic state

resulting from the high-spin $(t_{2g})^4(e_g)^2$ configuration and $^1A_{1g}$ is the spectroscopic state arising from the $(t_{1g})^6$ configuration). From spectroscopic measurements or electronic structure calculations, the energy difference can be estimated.

The $^5T_{2g} \rightarrow {}^1A_{1g}$ electronic transition is spin-forbidden so no absorption band is expected in Fe(II) oxides and silicates. But the energy difference (ΔE) between the $^5T_{2g}$ and $^1A_{1g}$ states of Fe^{2+}, as calculated from ligand field theory, is

$$\Delta E : ({}^5T_{2g} - {}^1A_{1g}) = 5B + 8C - 20\,\text{Dq}.$$

where B and C are the Racah parameters describing the interelectronic exchange and repulsion energy. However, the B and C Racah parameters for Fe^{2+} in oxides and silicates are not well known. The free ion value of B is 1,058 cm^{-1} (Lever, 1968) but for solids it should be less by a factor β, the nephelauxetic ratio. That is

$$B(\text{solid}) = \beta B\ (\text{free ion}).$$

For divalent transition-metal ions, β for oxides and silicates is about 0.9. In a free ion $C = 3.7B$ and $B = 1{,}058\ cm^{-1}$. Taking all values together, $5B + 8C$ becomes 32,950 cm^{-1}.

The optical absorption spectral band of Fe^{2+} in regular octahedral coordination in oxides and silicates gives the value of 10 Dq. However, due to the dynamic JT effect, the line may split. For example, in (Mg, Fe)O, the $^5T_{2g} \rightarrow {}^5E_g$ transition is split into bands at 11,600 and 10,000 cm^{-1}. Therefore, 10 Dq is either 11,600 or 10,000 cm^{-1}. When the dynamic JT effect is small, a single band occurs at 11,000 cm^{-1}(Mao and Bell, 1972).

For Fe_2SiO_4 spinel, 10 Dq equals 11,000 cm^{-1} at R(Fe–O) = 2.16 Å. Therefore, the HS–LS transition energy, ΔU, is calculated as 10,950 cm^{-1} at R (Fe–O) = 2.16 Å. How the ΔU energy will change with R (Fe–O) is estimated by assuming $^{10}Dq'/{}^{10}Dq = (R/R')^5$. The resulting values for ΔU as a function of R (Fe–O) are given in Table 5.10 below.

TABLE 5.10

Internal energy estimated from HS → LS transition in octahedral Fe^{2+}

	R(Fe–O) (Å)			
	2.16	2.05	1.95	1.85
Estimates from ligand-field theory (cm^{-1})[a]				
10 Dq	11,000	14,300	18,300	23,900
ΔU	10,950	4,346	−3,654	−14,850
Estimates from SCF–X_α–SW MO calculation (cm^{-1})[a]				
10 Dq	11,130	14,826	18,040	23,520
ΔU	10,760	3,243	−5,241	−16,210

Note: 10,000 cm^{-1} = 119.6 kJ/mol, and 1 eV = 8,066 cm^{-1}. ΔU can also be estimated from first-principles electronic structure calculations.

[a]Calculated using $\beta = 0.9$, $B = 1{,}058\ cm^{-1}$, $C = 3.7B$.

The electronic structure of an $(FeO_6)^{10-}$ cluster as a function of Fe–O bond length can be calculated using the self-consistent field X_α-scattered wave (SCF-X_α-SW) method. The theory behind the SCF-X_α-SW method is given by Johnson (1973) and Slater (1974).

The molecular orbital diagram for an $(FeO_6)^{10-}$ cluster with an Fe–O bond length of 2.16 Å is shown in (Fig. 5.20). The calculations were carried out using a spin-unrestricted formalism that takes into account the different exchange potentials for spin-up (α) and spin-down (β) electrons. Using the "transition-state" formalism (Slater, 1974), the energy of the HS $\rightarrow$ LS transition was calculated for $(FeO_6)^{10-}$ clusters with decreasing Fe–O bond lengths. The $^5T_{2g} \rightarrow {}^1A_{1g}$ energy is given by $2[\varepsilon(t_{2g}^{\beta}) - \varepsilon(e_g^{\alpha})]$, where $\varepsilon(t_{2g}^{\beta})$ and $\varepsilon(e_g^{\alpha})$ are the t_{2g}^{β} and e_g^{α} one-electron orbital energies in the configuration $(t_{2g}^{\alpha})^3(t_{2g}^{\beta})(e_g^{\alpha})^1$.

The results are in good agreement with the rough estimates obtained by using ligand-field theory. Fitting the SCF–X_α–SW calculated energies to the ligand-field

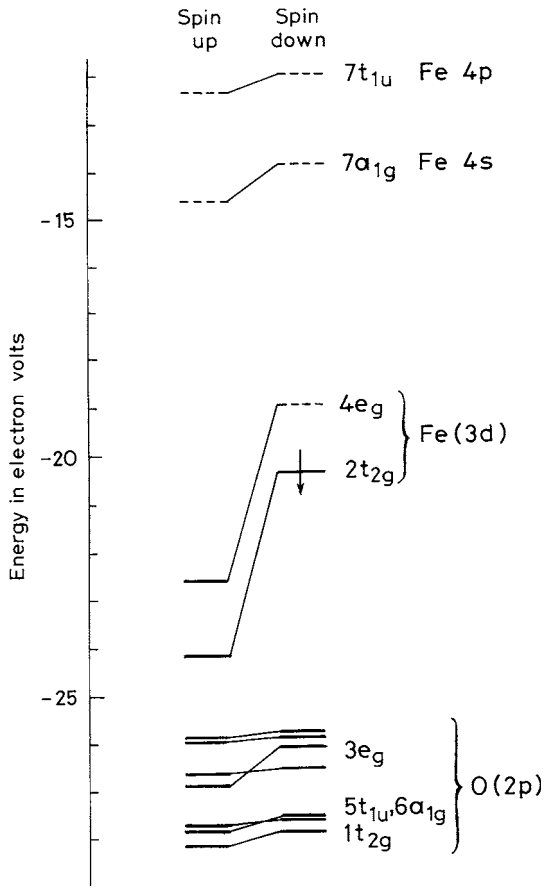

Figure 5.20. Self-consistent field X_∞–SW molecular orbital diagram for an $(FeO_6)^{10-}$ cluster at R(Fe–O) = 2.16 Å. Orbitals indicated by dashed lines are unoccupied.

relation gives

$$\Delta U = 5B + 8C - 20\,\mathrm{Dq}_0(R_0/R)^5$$

given $5B + 8C = 33{,}370\ \mathrm{cm}^{-1}$ and $10\,\mathrm{Dq}_0 = 11{,}480\ \mathrm{cm}^{-1}$ with $R_0 = 2.16$ Å. The SCF–X_α–SW calculated value for $5B + 8C$ decreases by about 10% when the Fe–O bond length is decreased from 2.16 to 1.85 Å. Also, the value for $10\,\mathrm{Dq}$ closely follows the ${}^{10}\mathrm{Dq}'/{}^{10}\mathrm{Dq} = (R/R')^5$ dependence.

5.11.2.2. Spin-pairing in the lower mantle

In the lower mantle, low-spin Fe^{2+} ions are likely to exist, as has been experimentally determined on a host of oxide phases by pressures overlapping those present in the lower mantle. Molecular orbital calculations (Tossel, 1976) also indicated that high-spin to low-spin transition could take place in Fe^{2+} in FeO in this mantle region (Sherman, 1988). MO calculations also showed that, at depths greater than 1,700 km, Fe^{2+} in magnesiowüstite would largely exist in low-spin state (Sherman, 1991). Low-spin Fe^{2+} ions may also exist in the perovskite structures in the lower mantle (Williams et al., 1989).

However, above the spin-pairing transition point, low-spin Fe^{2+} may have a smaller ionic radius than Mg^{2+}; this possibly would lead to a reversal of melting-point relationships. This change to low-spin configuration of Fe^{2+} would affect the magnetic properties of the lower mantle.

In the lower mantle, the transition of (Mg, Fe)O from B1(NaCl) to B2(CsCl) takes place along with the change in electronic structure of Fe^{2+} in silicate perovskite. In both the phases, Fe^{2+} occupy eight-coordinated sites. The change in internal energy, ΔU, for the HS $\rightarrow$ LS transition of 8-fold coordinated Fe^{2+}(the ${}^5E_g \rightarrow {}^3T_{1g}$), is estimated from ligand-field theory as

$$\Delta = -10\,\mathrm{Dq} + 6B + 5$$

calculating the difference between ${}^5E_g \rightarrow {}^3T_{1g}$ states. The calculated HS $\rightarrow$ LS transition energy for 8-fold coordinated Fe^{2+} as a function of the Fe–O bond length is given in Table 5.11.

The table indicates that any iron that is partitioned into the silicate perovskite phase will always be in the high-spin state, assuming that Fe^{2+} cations occupy only the 8 to 12-fold coordination sites. The calculations presented earlier suggest that the majority of Fe^{2+} cations in (Fe,Mg)O will not be in the low-spin state until a depth greater than 1,700 km is reached (*see* Fig. 5.21).

Magnesiowüstite (Mg, Fe)O and silicate perovskite (Mg, Fe)SiO_3 phases dominate in the lower mantle, where the ambient pressure is sufficient to effect a high-spin $(S = 2)$ to low-spin $(S = 0)$ transition.

Band broadening. Under pressure, the collapse of the high-spin magnetic state is caused by the band broadening due to shorter nearest-neighbour distances, not by an increase in the crystal-field splitting. The change in bond character from ionic to metallic would affect the mineral stability. As the charge moves out of the bond direction, the shapes of the

TABLE 5.11
HS → LS energy (in cm^{-1}) for 8-fold coordinated Fe^{2+}

	R(Fe–O) (Å)			
	2.30	2.16	1.95	1.85
10 Dq cm^{-1}	7.143	10.476	11.528	14.731
ΔU (cm^{-1})	16,186	12,853	11,801	8,598

All calculated by using $B = 1{,}058\ cm^{-1}$, $C = 3.7B$ and $\beta = 0.9$.

transition-metal ions and oxygen ions would change. This will affect the phase diagrams and elasticity.

Under high pressure transition-metal elements lose their properties and behave as different elements and the chemical behaviour drastically changes when the valence and other bonding electronic behaviour lose their significance in bonding.

5.11.3. Pressure dissolution and substitution

Dissolution of pyroxene in garnet has very little effect on thermal expansion but substitution of iron and magnesium in the pyrope–almandine join seems to have a large effect.

When δ_0 is calculated, using the $(dK/dT)_P$ values as reported by Soga (1967), its values become 5.3 for pyrope and 6.4 for almandine. For the pyroxene — garnet solid

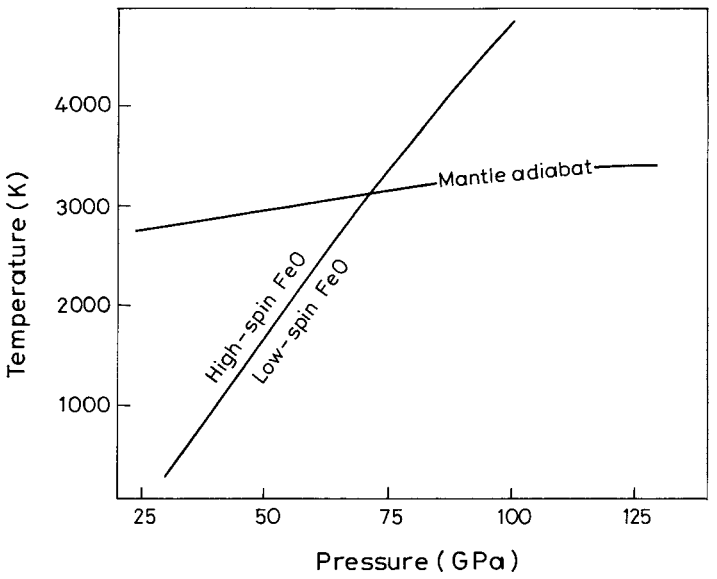

Figure 5.21. Calculated *PT*-curve for the high-spin to low-spin transition of FeO. Also shown is an approx. mantle geotherm (assumed adiabat). The HS → LS *PT*-curve crosses the mantle geotherm near 1700 km depths.

solution — it is observed (Yagi et al., 1987) that, with increasing pyroxene component, the bulk modulus seems to decrease and also that the thermal expansion of majorite is expected to be similar to that of garnet with the same Fe/Mg ratio.

5.12. Amorphization

Materials lacking translational or orientational long-range order are called amorphous phases. Although configurational disorder leading to excess entropy should render amorphous phases greater stability than ordered ones, this is not observed to be so. This is because, at temperature much below the melting temperature, the increase in entropy causes lowering of Gibbs free energy. This energy is, however, lower than the increase in the internal energy necessary for destroying long-range order by distortion.

Thus, at high temperature, the entropy term predominates up to the melting temperature and internal energy becomes less significant in determining the structural state of the material. Crystalline material with artificially created defects would transform to amorphous phase, thereby lowering its free energy. A common example is the amorphization or glass formation by radiation. In such a situation, the melting curve shows a downward trend with pressure. This pressure-induced amorphization (PIA) is termed "pseudo-melting".

Meteorite craters offer impact melted rock glass, called "diaplectic glasses". These contain dense pressure phases as stishovite or hollandite, formed at the high-pressure regimes in the Hugoniot curve.

High-pressure studies are critical for identifying new equilibria and metastable states that can be accessed as amorphous materials and compressed to smaller volumes. Recent studies of inorganic liquids and glasses under compression documented changes in nearest-neighbour geometry and vibrational spectra (Hemley et al., 1986; Williams and Jeanloz, 1988; Durben and Wolf, 1990). Just as crystalline compounds are modified by the high-pressure phase transitions, so the amorphous materials undergo structural transitions under pressure. In recent years, the intermediate-range order observed in amorphous materials has drawn considerable attention (Gaskell et al., 1991).

Studies on PIA have demonstrated that, at higher densities, potential energy dictates structures, not the entropy. At higher pressure, internal energy dominates, not entropy, and entropy does not favour the state. Unlike amorphization, through thermal quenching the kinetic processes are inhibited in a PIA.

5.12.1. Pressure-induced amorphization

A large number of materials which exhibit amorphization when subjected to static or dynamic high pressures have been investigated. The pressure-amorphized materials are now termed as "glass without fusion". In shock compression, the fusion and glassy structure may be a consequence of the high temperature and strain rates associated with it. However, an examination of the short- and medium-range order in

some of the pressure-amorphized materials suggests that these could be structurally different from the glasses obtained from quenching the melts. In this context, Raman spectroscopy has been extremely useful in providing insight into the evolution of disorders in the preceding crystalline phase. The residual short-range order in the amorphous state has also been deeply probed. It is found that the distribution of bond lengths and bond angles in the pressure-amorphized-state is narrower than those known in melt/quenched glasses.

The crystalline to amorphous transformation (c → a) opens up the question of clarifying (a) the relationship between these pressure-induced amorphous phases and the conventional glasses quenched from high-temperature melts and (b) the unusual mechanical processes that have been documented during metastable transitions in hydrous silicates. The latter may play an important role in generating deep-focus earthquakes in subduction zones (Meade and Jeanloz, 1991).

The pressure-amorphized state is metastable and is believed to be resulting from the kinetic hindrance of equilibrium-phase transitions. Slow kinetics associated with the molecular reorientation and translation across a phase transition leaves the system trapped in the metastable amorphous state. Directional bonds and non-hydrostaticity are some of the important factors that determine the amorphization pressure. The residual order in the pressure-amorphized materials is quantitatively different from quenched glasses. The existence of inhomogenous disorder in potash alum supports the applicability of a critical disorder model of amorphization. PIA was first observed in ice (Mishima et al., 1984). Sharma and Sikka (1996), however, suggest that this phenomenon may have been known earlier. Conversely, amorphization of crystalline phases stable at high pressure may occur on decompression. Liu and Ringwood (1975) showed that the cubic $CaSiO_3$ perovskite, which is stable at high pressure (~16 GPa), transforms to an amorphous phase during decompression.

Since the first report on ice (Mishima et al., 1984), a number of compounds have been found to exhibit amorphization at high pressure with widely different bonding natures, such as covalent SiO_2 (Hemley et al., 1988) and $AlPO_4$ (Kruger and Jeanloz; 1990), ionic $LiKSO_4$ (Arora and Sakuntala, 1992) and $Ca(OH)_2$ (Kruger et al., 1989), van der Waals SnI_4 (Sugai; 1985). PIA features have been observed in quartz-type forms of GeO_2 and $AlPO_4$, and also in framework silicates, pyroxenes, olivines and hydrous silicates.

Amorphization is brought about by different mechanism in different materials. For example, in quartz (SiO_2), the breaking of Si–O bonds due to bending of the Si–O–Si angles beyond their energetic limit has been proposed as the cause for PIA (Hazen et al., 1989). Dimerization of the tetrahedral molecules is believed to be the cause of PIA in SnI_4, whereas orientational disorder of sulphate ions is identified as reponsible for amorphization in a number of binary sulphates.

PIA has been reviewed by Richet and Gillet (1997) with reference to differential stress, crystalline transformations, compression mechanisms and shearing processes. They also discussed the thermodynamics of amorphization and mechanistic interpretations, with special reference to elastic and dynamic instabilities and shearing processes.

5.12.1.1. Metastability and reversible amorphization

A phase, while transforming from one crystalline state (c) to another crystalline state (c′) may get trapped in an intermediate metastable amorphous state (a) due to slow kinetics of c–c′ transition. Further pressurization may accelerate the a–c′ transition (*see* Fig. 5.22). As an example, high-density amorphous ice is seen to transform to crystalline ice VII when further pressurized to 4 GPa (Hemley et al., 1989).

Amorphization may be reversible or irreversible. Reversible transition with significant hysteresis is seen in cases of compounds having a dissimilar type of bonding among different groups of atoms such as $FeSiO_4$, $AlPO_4$, $Ca(OH)_2$, $LiKSO_4$, SnI_4, etc. Irreversible amorphization is seen in the cases of ice, quartz and $Ca_2Al_2Si_2O_8$ (Williams and Jeanloz, 1989). Examples of monatomic phases with directional bonds showing PIA are graphite (Goncharov et al., 1992) and sulphur (Luo and Rouff, 1993).

5.12.1.2. Non-hydrostatic pressure and amorphization

The presence of non-hydrostatic pressure also appears to have a role in driving the PIA. Freezing of the most commonly employed pressure-transmitting media such as methanol : ethanol (1 : 4) mixture at 11 GPa in a gasketted diamond-anvil cell leads to the development of a non-hydrostatic component of pressure in the cell. Hence, in some systems exhibiting PIA above 11 GPa, a non-hydrostatic pressure may be responsible. Under non-hydrostatic conditions, the Raman lines broaden much more rapidly and the amorphization pressure is lowered. The non-hydrostatic condition leads to shear stress and asymmetrical distortion of the molecular units. These accelerate the growth of disorder and thus effectively lower the pressure of amorphization. Lowering of amorphization pressure from 23 to 14 GPa is reported in graphite when no pressure-transmitting medium is used (Goncharov, 1992). A similar observation has been made with sulphur (Luo and Ruoff, 1993).

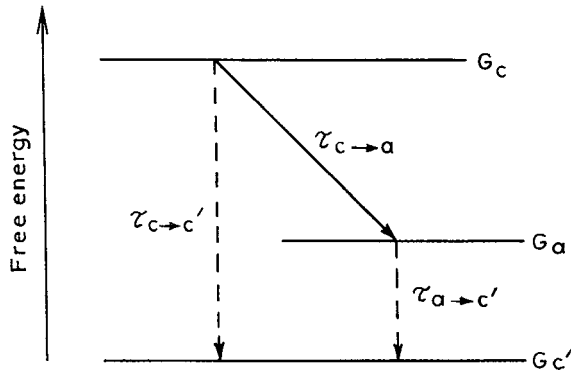

Figure 5.22. A schematic three level diagram for c → a, and a → c′ transformations.

5.12.2. Disordering and amorphization: Raman scattering

In the process of amorphization, the bond length and bond angle show a distribution other than being unique. As the amorphous phase lacks periodicity, the disappearance of lattice or the external vibrational modes in the Raman spectra is used to identify the PIA transition (Deb et al., 1993). The basic signature of amorphization by loss of long-range order in Raman spectrum lies in the vanishing of the external vibrational modes through the breakdown of the $q \approx 0$ selection rule. This results in manifesting the DOS through the second-order Raman scattering. This provides complementary information on the disorder in relatively more rigid units in the structure. However, it should be noted that vanishing or broadening of these modes may not necessarily correlate with the loss of long-range order.

The disorder is manifested in the broadening of the internal modes of the strongly bound polyatomic groups or molecular ions. An increase by a factor of ~ 5 in the width of Raman lines (Klug et al., 1986) or of infrared absorption (Kruger et al., 1989), associated with the internal modes, is observed across PIA.

Investigation of a number of binary sulphates shows that the high-pressure crystalline phases have disorder which is in the form of distinct orientations of sulphate ions. This results in the splitting of the non-degenerate symmetric stretching mode of the sulphate ions as seen in the Raman spectra (Arora and Sakuntala, 1992). Growth of these disorders eventually leads to amorphization. Raman spectra arising from the polyatomic units such as sulphate ions correspond to that of the bond lengths and bond angles. It should, in principle, be possible to obtain information about such short-range order from the analysis of the spectra.

5.12.2.1. Non-bonded atoms and steric hindrances

PIA can also be brought about by the structural frustration caused by kinetic impedance and steric hindrances (Sharma and Sikka, 1996). The steric constraints arise due to the reduction of non-bonded inter-atomic distances under pressure, when a significant modification of the molecular shapes is kinetically inaccessible. A general correlation is noted between the pressures of phase transformations and the limiting distances of non-bonded atoms. This happens when the repulsive energy cost for further squeezing those non-bonded atoms far exceeds the energy cost of the distortion of polyhedra. This leads to a phase transition to relieve the steric strain in the structure (Sikka et al., 1994).

For $AlPO_4$, the relevant non-bonded distances are for the non-bonded O···O atoms. For these, the largest steric limit is Pauling's van der Waals separation of 2.8 Å, and the smallest extreme limiting value is 2.6 Å. But a phase transition is not generally initiated at the van der Waals limiting distance. The O···O distances decrease with pressure and, between ~ 10 and 15 GPa, these reach a plateau value of ~ 3 Å (corresponding to the range where c/a ratio shows a plateau). At 29 GPa, there occurs a few O···O contacts which are ~ 2.58 Å, i.e., approaching the limit of 2.6 Å, at which distance the nucleation of the disordered phase occurs.

5.12.2.2. Memory glass: $AlPO_4$

The most common mineral known to manifest PIA is quartz, which, when subjected to a pressure of ~15–30 GPa at ambient temperature, undergoes slow amorphization. Kingma et al. (1993), however, have observed a new phase preceeding amorphization. An isostructural mineral, berlinite ($AlPO_4$), similarly shows PIA at ~20 GPa. This mineral, however, behaves as a memory glass' (e.g., Kruger and Jeanloz, 1990; Chaplot and Sikka, 1993; Polian et al., 1993).

A memory glass would recrystallize to the original crystallographic state upon release of pressure (i.e., quenching). Since the pioneering work of Kruger and Jeanloz (1990), this property has been noted in several materials iso-structural with quartz.

To investigate the mechanism of memory effect in berlinite, Tse and Klug (1992) and Chaplot and Sikka (1993) used inter-atomic potentials to perform molecular dynamics. They showed that the O–P–O bond-angle distribution remains close to the original in quartz structure and the PO_4 tetrahedra remain four-coordinated even when severely distorted. All these perform the observed memory behaviour. Some, however, noted it as polymorphic crystal–crystal phase transition (Gillet et al., 1995).

The crystallographic characters and changes under pressure of berlinite were earlier discussed under Section "Side-band fluorescence ultrasonic technique" of Chapter 4.

5.12.3. Solid–liquid (melt) stability boundary

The thermodynamic solid–liquid (melt) stability boundary is determined by the equality of free energies of the two phases. The mechanical stability of a crystal can be deciphered from the calculation of elastic constants at several pressures and temperatures. At a given temperature, the maximum pressure of stability is determined via the Born stability criteria. Mechanical instability occurs when a combination of elastic constants violates one of the Born stability conditions (*see* Born and Huang, 1956).

In a semi-empirical approach, the quasi-harmonic lattice dynamics may be combined with the Lindemann criterion for melting to compute a thermodynamic melting line. The mechanical instability line due to the violation of the Born stability condition $C_{11} - |C_{12}| > 0$ (*see* Born and Huang, 1956) and the theoretical thermodynamic curves are compared with experiment. The temperature where mechanical instability occurs is mostly higher than the thermodynamic melting point.

In a molecular dynamics study a mechanical instability due to the softening of the elastic modulus C_{66} $(= C_{11} - C_{12})$ of ice structure under high pressure has been proposed by Tse (1992).

5.12.3.1. Law of melting: Lindemann

The law of melting in its differential form is

$$\mathrm{d}\ \ln T_m / \mathrm{d}\ \ln \rho = 2(\gamma - 1/3) \tag{5-97a}$$

where T_m is the melting temperature, ρ is the density and γ is the Grüneissen parameter.

The relation relies on the postulation that, on melting, the long-range order of the solid state breaks down.

Lindemann theory offers the slope of the temperature of melting (T_m) with pressure as

$$\frac{\mathrm{d}T_\mathrm{m}}{\mathrm{d}P} = \frac{2T_\mathrm{m}}{K_\mathrm{T}}\left(\gamma - \frac{1}{3}\right) \tag{5-97b}$$

where γ is the Grüneisen parameter at a particular V and K_T is the isothermal bulk modulus at the T and V of the triple point. Again, $\gamma = \alpha_\mathrm{C} K_\mathrm{T} V / C_\mathrm{V}$, where α_V is the volume coefficient of thermal expansion and C_V is the specifics heat at constant volume.

Equation (5-97a), known as the Lindemann theory of melting, can be related to γ as

$$\gamma = \left(\frac{\delta \ln T_m}{\ln \rho}\right) \tag{5-98}$$

For melting relationships, equation (5-97a) or (5-98) seems to hold good in many cases.

$T_\mathrm{m}(P)$ can be determined by first calculating $P(V)$ and $T_\mathrm{m}(V)$. The thermal EOS appropriate to temperatures above $T_{\mathrm{m}0}$ (where $T_{\mathrm{m}0}$ is the temperature of melting at ambient pressure) is

$$P(V,T) = P(V,T_{\mathrm{m}0}) + P_\mathrm{th} \tag{5-99}$$

where the thermal pressure P_th is evaluated for $T > T_{\mathrm{m}0}$ along the melting curve.

The variation of γ with volume along the liquids is assumed to be

$$\left(\frac{\gamma(\rho)}{\gamma(\rho_0)}\right) = \left(\frac{V}{V_0}\right)^q \tag{5-100}$$

The values of γ_0 (at $P = 0$) of iron phases are presented by Anderson and Isaak (2000).

The melting temperature equation is obtained by substituting equation (5-98) in equation (5-97b) and integrating (Anderson, 1995, p. 286) so that

$$\frac{T_\mathrm{m}}{T_{\mathrm{m}0}} = \left(\frac{V}{V_0}\right)^{2/3} \exp\left\{\frac{2\gamma_0}{q}\left[1 - \left(\frac{V}{V}_0\right)^q\right]\right\} \tag{5-101}$$

where $T_{\mathrm{m}0}$ is the melting temperature at the beginning volume, V_0 at $P = 0$.

In some of the melting experiments, particularly those involving shock loading, the sample may not remain in the initial phase or in the single phase before melting. Often, decomposition or transition to another phase may precede the melting depending on the experimental conditions. This would also influence the observed melting temperature. Lower melting temperatures observed in an experiment may be largely accounted for by the level of defects. The true level of defects in a real sample in experiments could be much higher, depending on the sample history.

Mechanical melting is a consequence of the softening of elastic moduli.

Activation volume and melting temperature. The activation enthalpy H^* as a function of the melting temperature T_m (at 1 bar) can be expressed as

$$H^* = \alpha T_m$$

where α is a constant. This relationship seems approximately valid for thermally activated processes such as diffusion for similar structure but different composition (Frost and Ashby, 1982). Therefore, by incorporating the melting temperature T_m, the relation becomes

$$x^0 = K_0 T \exp[-(\alpha T_m + PV^*)/RT] \times [1 - \exp(\Delta G_r/RT)] \quad (5\text{-}102)$$

The activation volume V^* can also be related empirically to T_m (Poirier, 1985) for processes such as lattice diffusion and creep. However, the activation volume for a grain-boundary diffusion process (for example, the growth of spinel in olivine) will differ from the activation volume for lattice diffusion. Therefore, its relationship to T_m is not clear. There are at present no estimates for the activation volume of diffusion across inter-phase boundaries in minerals and there are no reliable models for the pressure dependence of this process. However, the activation volume V^* has been noted to decrease significantly with pressure increase (Kirby et al., 1996).